

# OSCILLATORY DEFORMATION OF AMORPHOUS MATERIALS: A NUMERICAL INVESTIGATION

THIS IS A TEMPORARY TITLE PAGE  
It will be replaced for the final print by a version  
provided by the service academique.

Thèse n. 6101 2014  
présenté le 17 Janvier 2014  
à la Faculté des Sciences de Base  
groupe Foffi  
programme doctoral en Physique  
École Polytechnique Fédérale de Lausanne  
pour l'obtention du grade de Docteur ès Sciences  
par

Davide Fiocco

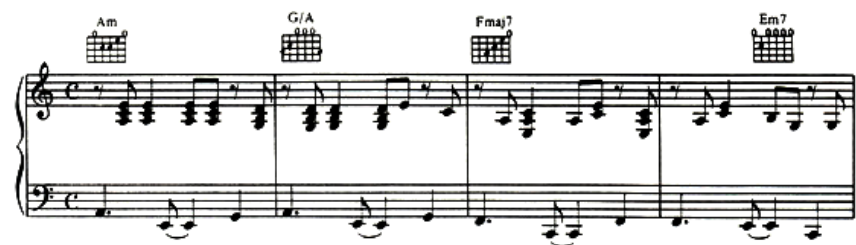
jury:

Prof Vincenzo Savona, président du jury  
Prof Giuseppe Foffi, directeur de thèse  
Prof William Curtin, rapporteur  
Prof Anne Tanguy, rapporteur  
Prof Hans Wyss, rapporteur

Lausanne, EPFL, 2013







— Morrissey & Johnny Marr



# Acknowledgements

I am grateful to my supervisor Prof. Giuseppe Foffi for the opportunity given to me to work in his group at the EPFL (and around the world!). Since the very beginning he has been very supportive and encouraging, always sharing his enthusiasm for science, giving a great freedom to explore ideas and creating an extremely friendly and familiar atmosphere in the whole group. I'm afraid I forced him to go beyond the call of his supervisory duties at short but intense times, and I cannot but thank him for the extra patience that he exercised with me.

A lot of inspiration and ideas contained in this thesis come from Prof. Srikanth Sastry. I deeply thank him for giving me the opportunity to work in his group at JNCASR and TIFR and for devoting his energy, time and sharpness of thought in a way that went beyond a scientific collaboration.

Srikanth and Giuseppe both had to struggle to fight the “Debbie-Downer-inside-me”, and I really hope that all in all it was worth it and fun.

I also thank Prof. Alfonso Baldereschi, for welcoming me to the ITP and introducing me to Giuseppe. I would also like to thank Noemi Porta, Tanya Castellino and Ursina Roder for all the work needed to make the ISJRP (and all the rest of the paperwork in [my] background) work. And Vittoria Rezzonico, Matteo Guglielmi and Florence Hagen for all the work related to the use of computational facilities at the EPFL. I thank Francesco Varrato, Nicolas Dorsaz and Alessandro Tuniz for reading the manuscript.

It will be hard to find elsewhere the same greatness that I have found in the ~~colleagues~~ friends that I have met in these four years. I really got more than what I gave, so I am indebted, and in a way that of course can't be expressed in a few sentences. The only thing I can say to excuse myself is that the standard set by them was too high.

Francesco has been a great teammate, and it's been fun and instructive to collaborate with him in the last months of my PhD. The word “patience” pops inside my mind when I think about his attitude towards me, but he's also been an example of intellectual curiosity and positive attitude during these four years. Nicolas (among the rest) gave me a lot good advices that I didn't always take, or not soon enough, because of the lack of credibility/applicability coming from the fact that he really is a bit of a hero in a lot of the things that he does (that's one of the things Giuseppe and I agree on). Maxim is a role model for clarity and scientific rigor to me, and I selfishly wish I had taken advantage of his presence more during his stay in the group.

---

It's been fun to live in the openspace in these 4+ years and share good moments with its inhabitants: an especially grateful thought goes to the unsurpassed Old Guard: Carlo, Claude, Daniel, Paolo and Tamás. And to Benjamin, for his constant encouragement and amazing puzzles I sometimes had to redshift from because of my lack of archmastery; Andrea, for her patience (with my food kleptomania, just to name one thing) and all the lifts I hitched, that turned fast into precious psychiatric help; Lorenzo, for pushing me to the swimming pool on Mondays, Salvo, for constructive criticisms about standing tall, these are difficult to accept at times! Tommaso and Frederic for (not-)being-friends-with-everybody, Duccio for making bus 22 a "naively singular" and fun ride and Rue de la Borde shorter and more interesting than it is, and Lucio, for making me switch from drowning people in lakes to mountaineering with great friends, just to name one reason. I was very lucky to have a great company during my stay in the Sastry lab at the JNCASR and TIFR. I thank Vishwas, Aparna, Shila and Moumita for the warm welcome, their help and the fun conversations and debates (!) that we had at the JNCASR. I would like to thank Sara and Olivier for hosting me in Paris during my visit to Orsay, and Alice, Susanna and Dani who made it feel like home in Zurich. Ottavia, Elisa and the summers with the Arcabologna made Switzerland good fun, so thanks! I don't know how Annaïse and Letizia could cope with a flatmate of my kind, and I thank Luisa for bringing *morbin* and a gust of *real world* everytime we met. SilvaTania taught me French, and I hope that trying to cook mayonnaise together was fun and worth it for her too. I thank, and that's the very last groovy time, Beppe who has been a constant friendly presence, with the tales of his Consonants, all the puns and the ESP jokes, and for making me think that mine was a great mind whenever we thought alike. I finally would like to thank my parents, Raffaella and Giuseppe, for their support and understanding, especially in the last months of completion of the thesis.

Lausanne, 13th December 2013

Davide

# Abstract

In this thesis we describe the results of simulations at the atomic level of a simple model of a metallic glass under cyclic shear deformation. We show that under oscillatory cyclic load, systems of Lennard-Jones particles exhibit a non-equilibrium transition as a function of the oscillation amplitude. At low amplitudes samples evolve at a microscopic level so to reach states which are unchanged by further oscillations, whereas above some threshold amplitude  $\gamma_c$  they evolve indefinitely. Similarly to what is observed in noncolloidal suspensions, samples are able, for small oscillation amplitudes, to retain a memory of the oscillation amplitude(s). Such amplitude(s) can be subsequently read by performing additional deformation experiments. We employ and develop simple models that are able to describe qualitatively such phenomenology, thus suggesting that a wider class of systems could be able to show the same transition and memory behavior. Separately, we study by means of computer simulation the behavior under deformation of a newly found class of soft matter systems, namely bigels, and compare it with that of single-component particle gels.

**Keywords:** Metallic glass, mechanical properties, computer simulation, shear deformation, non-equilibrium transition, athermal quasi-static deformation, NK model, memory, aging, rejuvenation, particle gel, bigel.



# Sommario

In questa tesi sono descritti i risultati di simulazioni a livello atomico di un modello semplice di *vetro metallico* sottoposto a deformazioni di taglio. Per effetto di deformazioni oscillatorie, sistemi formati da particelle interagenti tramite il potenziale di Lennard-Jones mostrano una transizione dinamica di non-equilibrio al variare dell'ampiezza della deformazione. Per piccole ampiezze, i campioni evolvono in modo tale da raggiungere stati invarianti per applicazione di deformazioni aggiuntive, mentre oltre una certa ampiezza di soglia  $\gamma_c$  i campioni evolvono indefinitamente. I campioni sottoposti a deformazioni di piccola ampiezza sono inoltre in grado di mantenere traccia di quest'ampiezza, analogamente a quanto osservato nel caso di sospensioni non-colloidali. Questa informazione può esser letta successivamente compiendo misure di deformazione aggiuntive. In questa tesi sono inoltre sviluppati e utilizzati modelli teorici che catturano qualitativamente tali comportamenti. Tale accordo qualitativo suggerisce che la transizione di cui sopra e gli effetti di memoria osservati nei modelli microscopici di vetri possano estendersi ad una classe più vasta di sistemi.

In un'appendice al lavoro, si analizza inoltre il comportamento meccanico di una classe di sistemi di materia soffice scoperta di recente: i bigel. Le proprietà di deformazione di questi sistemi sono inoltre confrontate con quelle dei gel a singola componente tramite simulazione al computer.

**Parole chiave:** Vetro metallico, proprietà meccaniche, deformazioni di taglio, transizione di non-equilibrio, modello NK, memoria, aging, rejuvenation, gel, bigel.



# Contents

<b>Preface</b>	<b>1</b>
<b>1 Introduction</b>	<b>5</b>
1.1 Bulk metallic glasses: results from experiments . . . . .	5
1.1.1 Bulk metallic glasses and the glass transition . . . . .	5
1.1.2 Mechanical properties of metallic glasses . . . . .	8
1.2 Theoretical models and computer simulations . . . . .	11
1.2.1 The Potential Energy Landscape . . . . .	11
1.2.2 Results from simulations of glasses relevant for this work . . . . .	16
1.2.3 Rejuvenation and overaging in the NK model . . . . .	20
1.2.4 Coarse-grained approach to the deformation of amorphous solids .	21
1.3 Oscillatory driven suspensions, memory effects . . . . .	21
1.3.1 Results on non-brownian suspensions relevant for this work . . . . .	21
1.4 Summary . . . . .	27
<b>2 Particle models and simulation of amorphous solids</b>	<b>29</b>
2.1 Lennard-Jones model for glassy systems . . . . .	29
2.2 Computer simulation of particle systems . . . . .	30
2.2.1 Molecular dynamics at constant $E$ or $T$ . . . . .	30
2.2.2 Simulation of deformation . . . . .	33
2.3 Simulation of athermal quasi-static deformation . . . . .	35
2.3.1 Effect of deformation on the energy landscape . . . . .	35
2.3.2 Consequences for athermal dynamics . . . . .	38
2.3.3 Oscillatory athermal deformation . . . . .	42
<b>3 Results from Lennard-Jones simulations</b>	<b>45</b>
3.1 Kob-Andersen Lennard-Jones mixtures (KA) . . . . .	45
3.2 Preparation of the samples - equilibrium simulations . . . . .	46
3.3 Results of AQS shear deformation simulations . . . . .	49
3.3.1 Energy of the structures: overaging and rejuvenation . . . . .	50
3.3.2 Stress tensor behavior . . . . .	53
3.3.3 Diffusion behavior . . . . .	54
3.3.4 Energy dissipation . . . . .	60

## Contents

---

3.3.5	Is $\gamma_c$ equal to the yield strain? . . . . .	64
3.4	Summary . . . . .	65
<b>4</b>	<b>Toy models of athermal deformation</b>	<b>69</b>
4.1	NK model . . . . .	69
4.1.1	Features of the NK model . . . . .	70
4.1.2	Energy landscape of the NK model . . . . .	71
4.2	Transition matrix (TM) model . . . . .	74
4.2.1	Classification of states by their transformation properties . . . . .	76
4.2.2	Construction of the $P$ matrix . . . . .	77
4.2.3	Intuition for the TM model . . . . .	78
4.3	Results from the NK model . . . . .	81
4.3.1	NK at equilibrium . . . . .	81
4.3.2	Evolution of the energy under deformation . . . . .	82
4.3.3	Diffusion behavior . . . . .	83
4.4	Results from the TM model . . . . .	86
4.4.1	“Diffusion” behavior: absorbing and recurring states . . . . .	86
4.5	Summary . . . . .	87
<b>5</b>	<b>Memory effects</b>	<b>91</b>
5.1	Memory effects in binary LJ mixtures, NK and TM models . . . . .	91
5.1.1	Training and reading protocols: single memory . . . . .	92
5.1.2	Multiple memories . . . . .	98
5.1.3	Summary and comparison with colloidal suspensions . . . . .	100
<b>6</b>	<b>Conclusions and Perspectives</b>	<b>103</b>
<b>A</b>	<b>Glossary of mechanical terms</b>	<b>109</b>
<b>B</b>	<b>The mortal random walk</b>	<b>113</b>
<b>C</b>	<b>Details of the NK model</b>	<b>115</b>
<b>D</b>	<b>Details of the TM model</b>	<b>119</b>
<b>E</b>	<b>Athermal deformation of gels and bigels</b>	<b>123</b>
<b>F</b>	<b>Data preservation</b>	<b>133</b>
	<b>Bibliography</b>	<b>142</b>

# Preface

One of the aims of research in materials science is to introduce materials whose mechanical properties guarantee increasingly better performances. A few examples can help to understand the need for high performance materials: in aerospace applications, materials of high *hardness*<sup>1</sup> and low density, combined with a low melting point [2] are needed in the making of shields able to protect spacecraft and satellites from debris traveling as fast as 15 km/s; microelectromechanical systems (or MEMS, devices whose size is in the order of  $\mu\text{m}$ ) sometimes operate in harsh environments, for example when used as pressure sensors in turbines. In this case resistance to corrosion is important, because corrosion can lead to device failure; high *strength* is also beneficial in MEMS subject to shocks, so that they don't break even when subject to intense forces [3]; in biomedical applications, biocompatible materials with a *yield strain* (so to match that of bones) and a high *yield strength* are desirable for implants [4]. In all these cases, the ability to process the materials, so to be able to inject them into a mold and cast them into the desired shape is a big advantage, as it reduces production costs.

In the second half of the twentieth century, a new class of materials was introduced and developed that exhibits the properties listed above, namely *metallic glasses*. The history of metallic glasses dates back to 1959, when Pol Duwez and collaborators [5] obtained flakes of an alloy of gold and silicon by means of splat quenching, a technique that allows cooling a hot melt (at above 1500 K) to room temperature at rates of  $\approx 10^7$  K/s. Their samples, analyzed with a Debye-Scherrer camera, revealed a disordered atomic structure. This was realized via the extremely fast quenching rate, which allowed to avoid crystallization in thin samples. Since then, other metallic alloys have been introduced which are able to avoid crystallization when quenched at relatively slow rates ( $\approx 10$  K/s), retaining an amorphous microscopic structure and making it possible to obtain *bulk* amorphous samples (rather than thin ones), which can be processed into the desired shape.

From a physicist's point of view it is interesting to understand how these amorphous ma-

---

<sup>1</sup>A glossary of the terms in italics in this paragraph referring to mechanical properties of materials is given in Appendix A. A useful overview is contained in [1].

terials form, characterize their macroscopic mechanical properties and link them to the microscopic structure of the material. The formation of the metallic glasses is an example of a *glass transition*, a phenomenon whose theoretical explanations haven't reached a unanimous consensus yet. As the behavior of undeformed glasses is not rationalized in a universally accepted way, one can well imagine that a thorough understanding of the behavior of metallic glasses under deformation is still out of reach. However, several models exist nowadays which are able to reproduce some of the features shown by metallic glasses in experiments that probe their mechanical properties. They can be classified by their granularity, which is the extent to which the system of interest is subdivided into smaller parts. For instance, a macroscopic chunk of material can be thought as composed of smaller homogeneous elements (as in the finite element method [6]) or broken down into its fundamental constituents and treated as a collection of interacting atoms (as in non-equilibrium molecular dynamics simulations [7]). Insights about the deformation behavior of metallic glasses have also come from the observation of other physical systems. An example in this sense is represented by colloidal glasses, where colloidal particles suspended in a fluid medium play the role of “mesoscopic atoms” whose motion (as opposed to that of real atoms) can be tracked [8] and give insights about the motion of atoms in a metallic glass. Starting from these observations one can build and improve theoretical models to help *design* new amorphous materials with the desired properties.

In this thesis we model systems as composed by particles interacting via isotropic potentials and we study their behavior under a particular kind of deformation, namely cyclic shear deformation. We do so by means of computer simulation in the athermal quasi-static regime, which is supposed to describe qualitatively the phenomenology of metallic glasses well below their glass transition temperature  $T_g$ . We also compare our results with experimental and simulation data on noncolloidal suspensions, and explore similarities and differences between the two classes of systems. Our findings aim at being predictions of the outcome of oscillatory experiments on real amorphous materials, and benchmarks to test coarser-grained models.

### Structure of the thesis

In chapter 1 we briefly review the remarkable properties of metallic glasses as shown by experiments. Afterwards, we outline some of the concepts that have been introduced to model their behavior. We then focus on the effects of oscillatory deformation, as studied by previous computer simulations. We finally describe the outcome of experiments and computer simulations of oscillatory deformation of dilute noncolloidal suspensions, which show how these systems can retain memory of their mechanical history. Note that chapter 1 is by *no means* an introduction to the vast fields of mechanical properties of materials and phenomenology and theory of glasses, but aims at providing a minimal set of conceptual tools, terminology and set the context and the motivation of the

thesis. In chapter 2 we describe the particle model and the algorithms used to study the deformation behavior of glassy samples of binary mixtures via computer simulation. In chapter 3 the results of our simulations are reported. In chapter 4 we describe abstract models that retain some of key ingredients of the original particle model, while dropping significant features of it. In chapter 4 we also show that these models capture qualitatively the behavior observed in chapter 3.

In chapter 5 the phenomenon of memory, already analyzed in the literature in the case of dilute noncolloidal suspensions, is discussed in the context of the particle models in chapter 2 and of the models in chapter 4.

The reader should be aware of the fact that chapters are meant to be read in a sequential way, as most of them often rely heavily on definitions and concepts illustrated in previous chapters.

The appendices contain the details omitted from the other chapters. Appendix E is a stand-alone chapter that contains the results of simulations of deformation on soft matter systems, namely *particle gels* and *bigels*, that use the same numerical techniques used on glasses in the core of the thesis.



# 1 Introduction

## 1.1 Bulk metallic glasses: results from experiments

### 1.1.1 Bulk metallic glasses and the glass transition

Several kinds of metallic glasses exist, differing by composition. Most of them are alloys of transition metals, such as Zr, Al, Ni and Cu. They are obtained by fast cooling (quenching) a hot melt composed by such elements fast enough so to avoid crystallization, so that atoms do not arrange themselves in ordered lattices. If the choice of the elements and their concentration is such that crystallization does not occur, the mixture is said to have “good glass forming capabilities”. If bulk solid samples can be obtained, the result is a *bulk metallic glass*. There is no set of precise rules to determine if a given melt will be a good glass former, but still some features have been shown to be beneficial to impede crystallization [9, 10]:

- constituting elements should have negative heat of mixing, so that unlike elements stick together forming energetically favored structures, rather than separating into pure phases;
- elements should have different sizes. Size is seen to play a major role in determining whether crystal structures are favored over disordered ones;
- mixtures should contain more than three elements. Intuitively, the rationale behind this requirement is to make crystal configurations more complex and harder to reach in configuration space. However (as in the Duwez experiment [5]), binary mixtures also show glass forming capabilities.

As for the choice of the composition, eutectics are, generally speaking, better glass formers. In multicomponent systems, however, eutectic points are hard to find because of the complexity of the phase diagrams. An additional difficulty is represented by the fact

that the best glass formers have a narrow compositional range.

If the criteria above are satisfied, the melt can avoid crystallization as temperature is lowered, and enter in a *supercooled state*. At a microscopic level, supercooled configurations are very similar to those assumed in the liquid state, and thus characterized by absence of long range order. In such a state, the shear viscosity  $\eta$  is seen to dramatically increase with decreasing temperature (see for example [11]), and experimental data on the shear viscosity can be fit by the Vogel-Fulcher-Tamman law:

$$\eta = \eta_0 e^{\frac{BT_0}{T-T_0}} \quad (1.1)$$

where  $\eta_0$  and  $B$  are constants. The consequence of Equation 1.1 is that at some temperature  $T_g$  (named the *glass transition temperature* [12]) well above  $T_0$  the viscosity becomes so high that samples behave like solids on experimental timescales, and as such can sustain shear stress, even though the microscopic structure is disordered and similar to that of liquids. In that case, one says that a *glass* has been formed. Incidentally the  $T_g$  of metallic glasses is typically above room temperature, so that they are solid in ambient conditions. Data on  $\eta$  for several bulk metallic glass formers and other systems are plotted in Figure 1.1 as a function of the inverse temperature, rescaled by the respective  $T_g$  (see also [12]). Metallic glasses in this plot show a non-exponential dependence from  $T_g/T$ , and thus belong to the class of *kinetically fragile* glass formers (as ortho-terphenyl), differing from the so-called *kinetically strong* ones (such as  $\text{SiO}_2$ ), which instead show an exponential dependence of  $\eta$  on the inverse temperature.

The temperature  $T_g$  marks not only the transition from a (supercooled) liquid to a solid-like state, but also the passage from an equilibrium state (metastable with respect to crystallization) to a regime where the sample appears to be *out of thermodynamical equilibrium*. The absence of equilibrium below  $T_g$  translates into a very slow drift of mechanical, calorimetric and electrical properties [15, 16] with time and their dependence on the detailed thermal history of the sample during the quench. In fact, the material behaves differently depending on its *age*, i.e. the time elapsed since the cooling of the sample below  $T_g$ . This phenomenon of *aging* is accompanied by an evolution of the structure at the microscopic level (also called *structural relaxation*), and can be measured in metallic glasses via X-ray photon correlation spectroscopy [17] or positron annihilation lifetime spectroscopy [18].

Another phenomenon that is observed in metallic glass melts below  $\approx 1.2 T_g$  is the breakdown of the Stokes-Einstein relation [19], which states that

$$\frac{D\eta}{T} = c \quad (1.2)$$

where  $D$  is the translational diffusion coefficient and  $c$  is a constant.

## 1.1. Bulk metallic glasses: results from experiments

---

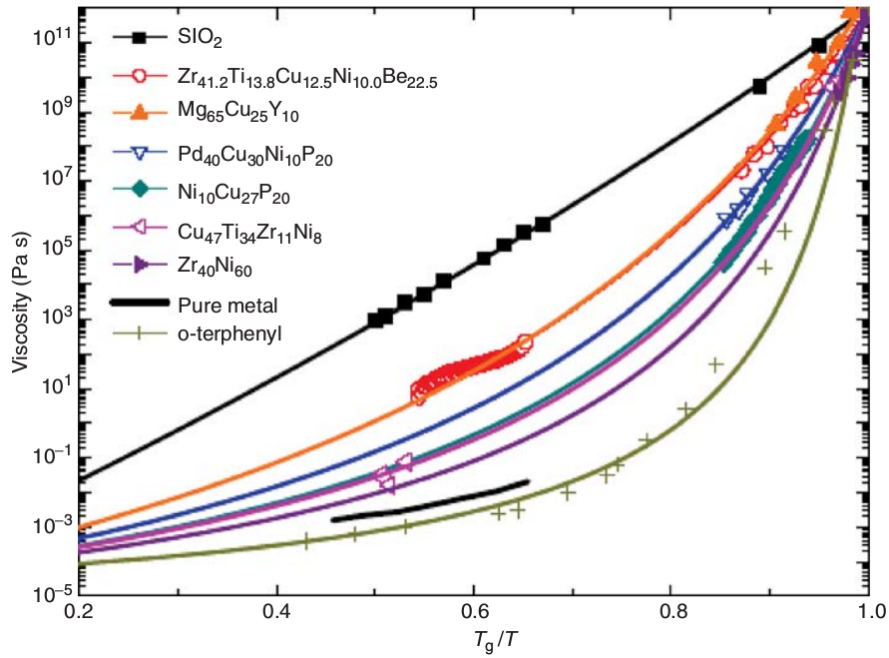


Figure 1.1: Plot of the viscosity as a function of the normalized inverse temperature  $T_g/T$  for different metallic glass formers in their supercooled state. Such a plot is often called “Angell plot” in the literature [13].  $T_g$  is defined as the temperature at which a given system has a viscosity of  $10^{12}$  Pa s. Fits using Equation 1.1 are superimposed. For reference, data relative to ortho-terphenyl and  $\text{SiO}_2$  are reported. Metallic glass formers show a behavior which is qualitatively similar to that of ortho-terphenyl, and thus are classified as *fragile* glass formers (see text). From [14].

### 1.1.2 Mechanical properties of metallic glasses

Below  $T_g$  bulk metallic glasses exhibit remarkable mechanical properties. In tensile deformation experiments (see Appendix A for a glossary of terms relative to the properties of materials subjected to tensile experiments), they behave elastically (so that stress deviates very little from a linear function of strain) up to high values of strain. In fact the yield strain is  $\approx 0.02$ , which is close to that of polymeric materials and an order of magnitude larger than the value  $\approx 0.002$  of typical crystalline metals. This fact, combined with Young moduli comparable to those of crystalline metals, allows them to exhibit very high *strengths* (see Figure 1.2). The high yield strain and the high values of the Young modulus make it possible to store elastically in bulk metallic glasses large quantities of energy per unit volume, endowing them with high values of *resilience* (see Figure 1.3). Furthermore, their *loss coefficient* is extraordinarily low. All the properties listed above are in general desirable for applications: strength allows to sustain large loads without undergoing irreversible deformation, enhancing durability; high strength incidentally translates into high *hardness*, which means resistance to wear; high resilience and low energy losses make bulk metallic excellent candidates for spring applications, where mechanical energy needs to be stored and recovered.

However, metallic glasses possess some characteristics that limit their widespread adoption in applications. Notably, if a sample made of metallic glass is deformed beyond its yield strain it typically exerts lower and lower forces. In fact, contrary to what is commonly observed in crystalline metals, metallic glasses undergo work *softening* upon loading. For strains slightly above the elastic limit deformation becomes localized in *shear bands* and leads to catastrophic failure (see Figure 1.4). For this reason, metallic glasses are said to be *brittle*, and are not as *ductile* as metals that are able to undergo large *plastic* deformations beyond their elastic limit. This is clearly a drawback in structural applications, where one would like a material to be able to sustain large strains before rupturing. Another drawback is the low fatigue limit [21] observed for some metallic glasses. When deformed cyclically, metallic glasses can exhibit fatigue cracks even well below their yield strain [22]. This also limits their reliability under cyclic loads.

### Rejuvenation and overaging

A debated issue in the context of deformed glasses is the possibility to revert the state of an aged (in the sense of subsection 1.1.1) glassy sample to a state where it shows properties that it had at an earlier stage of the aging process. This phenomenon goes under the name of *rejuvenation* and has been observed in calorimetric experiments on metallic glasses [24].

As mentioned above in the context of fatigue, oscillatory load can lead to changes in the material. In some cases [25] cyclic deformation makes the properties of samples similar to those that one would expect to find in *more aged* samples. In these cases,

## 1.1. Bulk metallic glasses: results from experiments

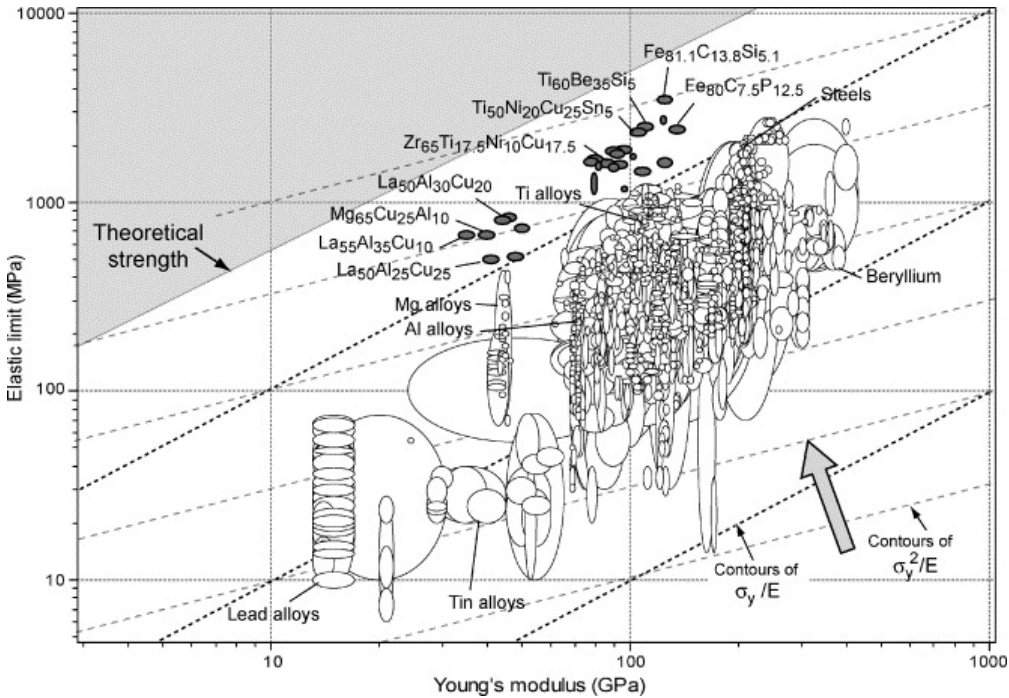


Figure 1.2: Strength (here named “elastic limit”) and Young modulus for various materials. This kind of plot, with two material properties on the axes and ellipses enclosing the values relative to different materials, is called in the literature “Ashby plot” [1]. Data relative to metallic glasses are enclosed by darker ellipses. Thanks to their exceptional strength, metallic glasses lie well above materials with a comparable Young modulus. From [20].

## Chapter 1. Introduction

---

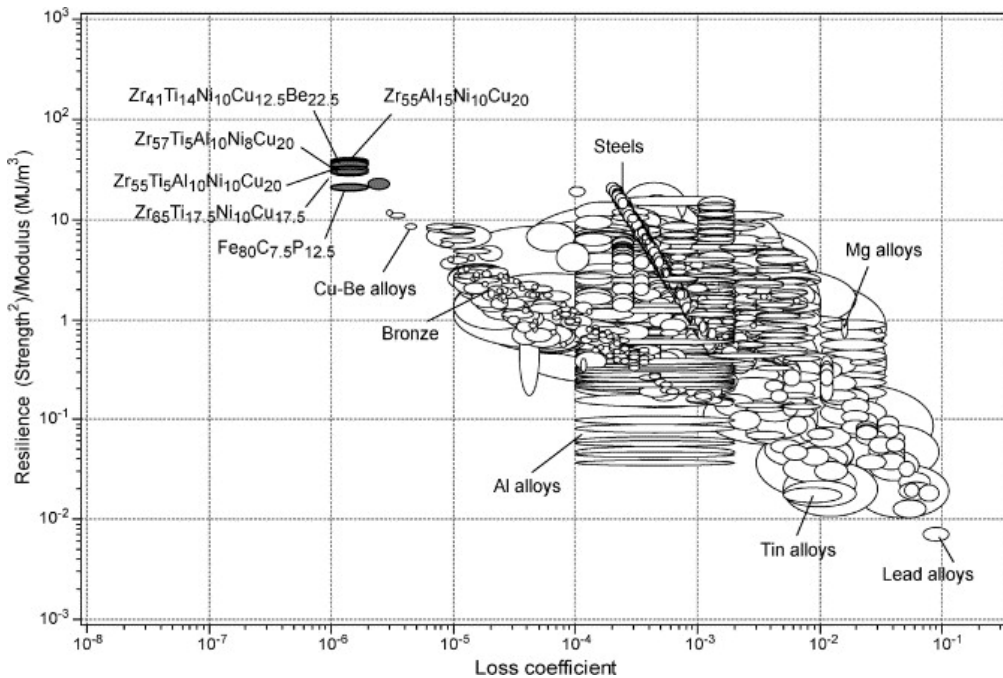


Figure 1.3: Ashby plot of the resilience and loss coefficient for various materials. Metallic glasses are outliers, as they can store very high amount of energy per unit volume (high resilience) and dissipate very low amounts of the stored energy when they undergo cyclic deformation (low loss coefficient). From [20].

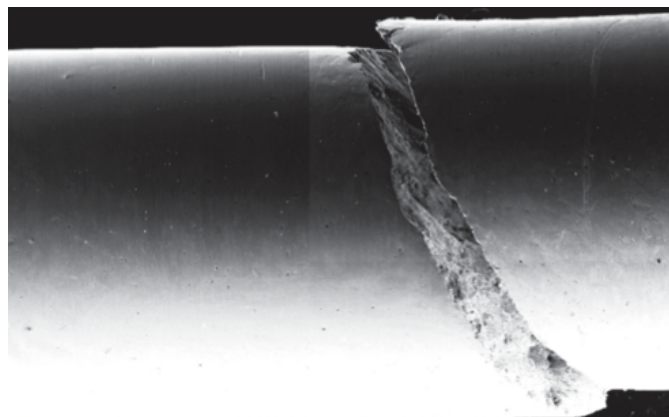


Figure 1.4: Typical brittle fracture of a metallic glass rod subjected to tensile strain. Metallic glasses don't typically show the necking behavior shown by ductile metals. Adapted from [23].

when mechanical deformation is seen to accelerate the process of aging, one speaks of *overaging*.

## 1.2 Theoretical models and computer simulations

The impressive increase in viscosity, the phenomenon of *aging* and the breakdown of the Stokes-Einstein relation are shared by other *glass forming* materials, and have been problems that have puzzled physicists for a very long time. An introduction to these and other aspects of the glass transition is given in [26] and in several other recent reviews on the subject ([27–29] just to name a few).

Here we present one of the most important frameworks used in the literature of the physics of glasses to rationalize their behavior, namely that of potential energy landscape (PEL) [30, 31], which will be extensively used throughout this thesis.

### 1.2.1 The Potential Energy Landscape

#### Geometrical properties of the energy landscape

Here we want to describe a supercooled liquid, or a glass, at a fine-grained level, that is by decomposing it into the set of interacting atoms<sup>1</sup> that form it. Each of the  $N$  atoms in a given system is thus thought to have (in 3 dimensions) 6 translational degrees of freedom, which evolve according to a set of Hamilton's equations of motion in a volume  $V$ . The potential part of the Hamiltonian takes into account the nuclear and electronic degrees of freedom in a coarse grained way, “condensing” them in the  $6N$  spatial coordinates and velocities of the nuclei. In particular, the potential energy function  $U$  can be expressed as a function of the coordinates of the nuclei:

$$U(\mathbf{r}_1, \dots, \mathbf{r}_N) \tag{1.3}$$

where  $\mathbf{r}_i$  is the position of the  $i$ -th atom. In this view, the system can be represented as a point moving on the  $3N + 1$ -dimensional surface  $(\mathbf{r}_1, \dots, \mathbf{r}_N, U(\mathbf{r}_1, \dots, \mathbf{r}_N))$ . Such surface is named in the literature “potential energy landscape” (PEL) and is characterized by “peaks” (in correspondence of configurations with a large potential energy with respect to neighboring configurations), “valleys” (energetically favored configurations) and “mountain passes” separating different valleys.

It is useful to note that any external perturbation  $\Delta U$  dependent on the coordinates of the particles of the system changes the form of the energy landscape:

$$U'(\mathbf{r}_1, \dots, \mathbf{r}_N) = U(\mathbf{r}_1, \dots, \mathbf{r}_N) + \Delta U(\mathbf{r}_1, \dots, \mathbf{r}_N) \tag{1.4}$$

---

<sup>1</sup>The same approach can be applied to molecular, or colloidal glasses as well. In that case however the simplest element won't be an atom, but an entire molecule (as in the case of a *molecular glass*) or a colloidal particle *in the case of a colloidal glass*, with its degrees of freedom.

## Chapter 1. Introduction

---

We will describe in detail in chapter 2 how an externally imposed mechanical deformation acts like such a perturbation, and this fact will be of fundamental importance in our analysis.

Important points of the potential energy landscape are its local minima. In a local potential energy minimum the system is mechanically stable: the force on each particle is zero and imposing a small displacement on one of them originates a force that tends to put it back in its original position, in a way that depends on the Hessian of the potential at the minimum. Incidentally, any configuration can be mapped onto one of such energy minima<sup>2</sup> once that a energy minimization procedure is adopted. Such minima are called *inherent structures* or *inherent configurations* [32]. Note that once that a minimization strategy is set, the configuration space is partitioned into different *basins*, each basin being formed by the points mapping onto the same inherent structure through the minimization procedure.

The energy landscape is a surface in a highly dimensional space, and as such it is hard to have an intuitive understanding of it and of its inherent structures. A better intuition of some of its features can be obtained by means of a simple argument and a graphical representation. The simple argument leads to the conclusion that *the number of inherent structures is exponential in the number of particles  $N$* . To understand this, consider a system composed of a large number of particles  $N$ , and divide it into  $L$  subsystems composed by  $n$  particles. If  $n$  is sufficiently large, and the potential between the particles is short ranged, one can safely assume that the influence of each subsystem on the other subsystems is weak, and treat them as independent. If the subsystems are independent, the supersystem is in an inherent structure if and only if each of its subsystems is in an inherent structure. If we call the number of inherent structures of each subsystem  $m$ , the number of inherent structures  $M$  is given by

$$M = m^L = m^{N/n} \tag{1.5}$$

The consequence of this fact is that the landscape becomes very complex as  $N$  increases, and a detailed enumeration of the local minima of the landscape becomes unfeasible for systems composed by more than a few dozen of particles [33].

The useful way to represent energy landscapes mentioned above consists in drawing *disconnectivity graphs* [34]. To construct a disconnectivity graph for a given potential energy landscape one initially picks a low threshold value of the energy. At that value of the threshold, some pockets of the configuration space will contain configurations whose energy is lower than the threshold. As the energy threshold is increased, some pockets coalesce, and others will appear (see Figure 1.5 for an example with an energy landscape

---

<sup>2</sup>Strictly speaking this is not *always* true: if the steepest descent algorithm is used, for instance, critical points as local maxima and saddle points (and points mapping to saddles through steepest descent) can't be unambiguously associated to a local minimum. Such points, however, are expected to belong to a measure zero set anyway.

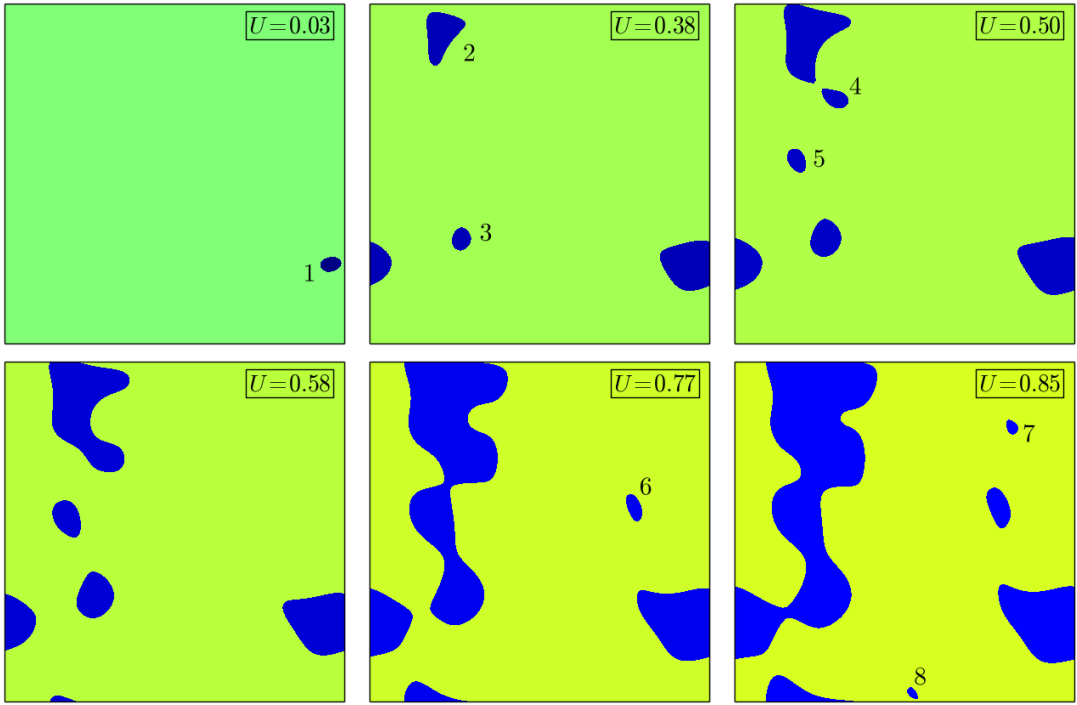


Figure 1.5: Schematic representation in 2D of an energy landscape. Regions of the energy landscape in Figure 1.6a that lie below and above the threshold value specified in the legend. Pockets with energy lower than the threshold value are drawn in blue. These are labeled so to be associated to the disconnectivity graph in Figure 1.6b.

in two dimensions<sup>3</sup>). A disconnectivity graph encodes the information about how many disconnected pockets exist at a given energy and at what energy coalescences between them occur. The disconnectivity graph relative to the landscape in Figure 1.5 is given in Figure 1.6b.

Using terminology of graph theory [35], a disconnectivity graph is a *tree* and each of its *leaves* is associated to an inherent structure, whereas the *internal vertices* are associated to barriers in the landscape. An example of a (part of a) disconnectivity graph for a system of Lennard-Jones particles (taken from [36]) is given in Figure 1.7.

### Dynamics in the energy landscape

The idea behind the landscape approach is that the way the system evolves in configuration space is affected by the topography of the landscape. At high temperature, the system has a total energy large enough to be able to visit different configurations with probabilities that are only slightly influenced by the value of the potential energy of such configurations. This is because the probability density is proportional to the Boltzmann factor  $e^{-\beta U(\mathbf{r}_1, \dots, \mathbf{r}_N)}$  (where  $\beta$  is  $1/k_B T$ ). If the temperature is high enough, one

---

<sup>3</sup>Refer to [34] for plenty of one-dimensional examples.

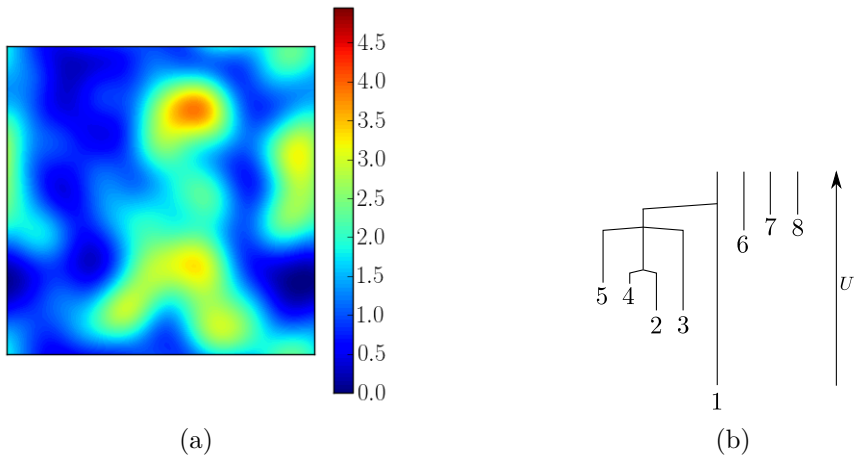


Figure 1.6: (a) Schematic representation in 2D of an energy landscape, which is supposed here to have only two degrees of freedom. The heat map describes the potential energy of the landscape used in Figure 1.5. (b) Disconnectivity graph of the deepest minima of Figure 1.6a.

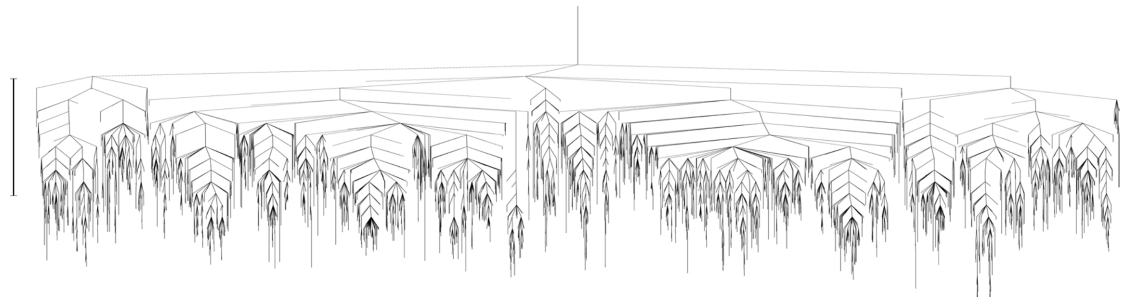


Figure 1.7: Disconnectivity graph for a Lennard-Jones binary mixture. Adapted from [36].

## 1.2. Theoretical models and computer simulations

---

can consider that for the majority of configurations  $U \ll kT$  so that their probability density is almost constant. In this regime the system is able to overcome the barriers that separate different basins, and the motion of the system is not affected much by the landscape. Note that as the system doesn't visit preferentially any part of the landscape, the average properties of the configurations that the system visits are simply related to the volume of configuration space associated to them<sup>4</sup>.

At lower temperature the system explores preferentially low potential energy regions of the landscape, and has difficulties in crossing the potential energy barriers in the landscape. In this case the landscape is able to confine the system for some time within some of its basins, thus slowing down its dynamics and reducing its ability to relax stress fluctuations. This fact is at the root of the viscosity behavior described by Equation 1.1. The details of the microscopic dynamics have been related to the features of the depth and topology of the landscape [37], and the landscape approach has proved successful in predicting quantitatively the behavior in Equation 1.1 [38] and rationalize the phenomenon of aging [39].

The dynamics of systems in the landscape can be studied using numerical simulation techniques like Molecular Dynamics (MD). In MD  $N$  particles (in our case representing atoms in a solid) are let evolve according to their interaction potential  $U$  in Equation 1.3 in a way that mimics their dynamics in real materials. In a simulation, particle positions are known at any point in time, an information that is experimentally inaccessible in the case of atoms in the bulk of real materials. This means that computer simulation allows to *track the motion of systems in their energy landscape* and gather microscopic insight about their macroscopic behavior [31].

In the case of metallic glasses, constituent atoms can be simulated as point particles interacting via a so-called embedded atom potential (or EAM potential) [40]. Potentials of this class can be written in the form

$$U = \sum_{i=1}^N \sum_{j < i} \phi(|\mathbf{r}_i - \mathbf{r}_j|) + \sum_{i=1}^N F(\rho_i(\mathbf{r}_i)) \quad \rho_i(\mathbf{r}_i) = \sum_{\substack{j=1 \\ j \neq i}}^N \psi(|\mathbf{r}_i - \mathbf{r}_j|) \quad (1.6)$$

where  $\phi$  is a pair potential interaction,  $\psi$  represents the electron density around a nucleus, and  $F$  is the so-called *embedding function*. The function  $\rho_i$ , according to its definition, can be thought as the sum of the electronic densities due to all the atoms but the one labeled with  $i$ . If  $F$  was linear in  $\rho$ , Equation 1.6 would reduce to a simple pairwise additive potential. In the embedded atom method, however,  $F$  is non-linear, so that Equation 1.6 is a many-body potential, which takes into account the fact that the presence of an atom alters the strength of the interaction between the other atoms. The detailed functional forms of  $F$ ,  $\rho$ ,  $\phi$  and  $\psi$  can be determined from first principles

---

<sup>4</sup>This is a simple consequence of the fact that the average value of an observable  $A$  that depends only on the positional degrees of freedom is  $\langle A \rangle = \int A(\mathbf{R}) e^{-\beta U(\mathbf{R})} d\mathbf{R}$ , and this expression, in the case of high  $T$ , simplifies in  $\langle A \rangle = \int A(\mathbf{R}) d\mathbf{R}$ .

using ab-initio methods [40].

An accurate, quantitative description of a material can be traded for simplicity by using a simple pairwise additive potential. This choice is often done in the literature whenever one is more interested in a qualitative, general description of a phenomenon rather than in the determination of the behavior of a specific material. A popular choice in this sense is represented by the Lennard-Jones (LJ) potential:

$$U = \sum_{i=1}^N \sum_{j < i} \phi(|\mathbf{r}_i - \mathbf{r}_j|) \quad \phi(r) = 4\epsilon \left[ \left( \frac{\sigma}{r} \right)^{12} - \left( \frac{\sigma}{r} \right)^6 \right] \quad (1.7)$$

which describes accurately the interaction between noble gases such as Ar, Kr, Xe, but has also been employed (in its multi-component generalization) to model mixtures of Ni and P [41].

### 1.2.2 Results from simulations of glasses relevant for this work

The analysis of the trajectories of particles interacting with potentials like those in Equation 1.6 and Equation 1.7 in dense systems has revealed features of their motion such as *dynamic heterogeneities* and an increasing *cooperativity* in particle motion as  $T$  is lowered in the supercooled and glassy states. These observations have been successively confirmed by experiment [42]. The possibility to measure accurately the structure has also allowed the search of *structural* signatures of glassy behavior, and growing *static* lengthscales (i.e. not related to dynamics, but to the mere arrangement of the particles at a given time) at the root of the viscosity behavior in Equation 1.1 [28].

Rather than exploring the features listed above, which are related to the way *undeformed* glasses behave, in this thesis we focus our attention on the behavior of glasses under deformation. Several techniques can be used to model the behavior of solids under deformation, and these in turn can be classified by their granularity, which is the resolution that they have in space and time. Such methods are extensively reviewed in [43] (with many more details than those mentioned here), where the possibility of combining them in a *multiscale* approach is also discussed. In this thesis, we try to understand what is the effect of *cyclic shear deformation* on glassy samples at a *microscopic* level, using techniques that are described in chapter 2 and analyzed more extensively in [43] and [44]. This is expected to give us insights about the phenomena seen in experiments where a sample is subject to a cyclic load, and to clarify the origin of mechanical *rejuvenation* and *overaging* mentioned in subsection 1.1.2. Before doing so, we introduce here some results obtained in the past by means of simulation of Lennard-Jones systems. Such results are propedeutical in the understanding of the following chapters and lie at the foundations of the present work.

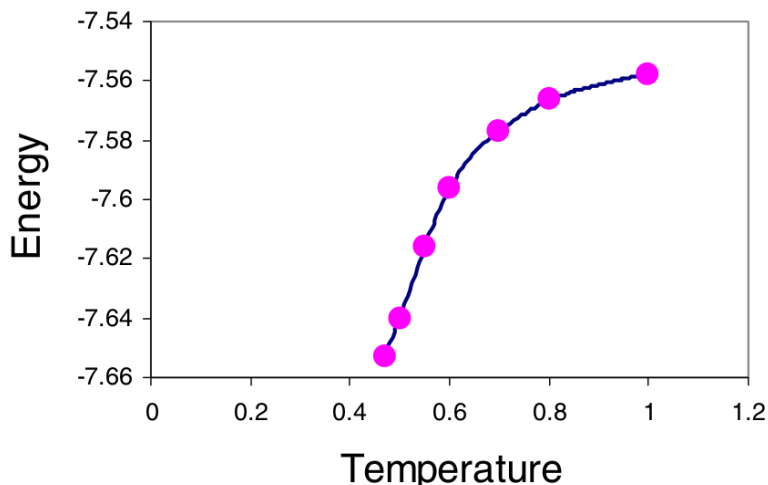


Figure 1.8: Average energy per particle for inherent configurations of a binary Lennard-Jones mixture obtained by quenching samples equilibrated at different  $T$  at infinite rate. At low temperatures the quench brings the system to minima with average lower energy. From [45].

#### Average $U$ of glasses obtained by cooling from finite $T$ to 0 at infinite rate

As we stated above, at low temperature a system is expected to assume configurations whose potential energy is low. In [45], configurations of a binary mixture of Lennard-Jones particles equilibrated at temperature  $T$  are quenched via an energy minimization procedure so to obtain the inherent structures to which they are associated. Physically, this operation corresponds to cooling the initial configuration to zero temperature at an extremely fast rate. The value of the temperature of the equilibrated samples from which inherent structures are obtained via energy minimization is called *effective temperature* of the corresponding inherent structures. If one plots the average potential energy  $U$  of such inherent structures as a function of their effective temperature, one gets a plot like that in Figure 1.8. At high  $T$  the system can be thought as residing in a given energy basin for a time that depends more on the extent of the basin in configuration space rather than its depth<sup>5</sup>. Increasing  $T$  further thus does not change the average energy after a quench (see Figure 1.8). At low temperatures the system will instead sample preferentially states with low energy, and thus spend time in deeper basins of the landscape. It's easy to believe that if the energy is minimized, the system will on average reach deeper inherent structures when starting from configurations equilibrated at lower  $T$ . In the language of disconnectivity graphs, this means that at low  $T$  the system spends more time in the basins associated to the leaves with the lowest energy in graphs like that in Figure 1.7.

<sup>5</sup>This is because the Boltzmann factor at high temperatures will be  $\approx 1$  wherever the potential has a small absolute value, and this includes all states with a negative potential energy.

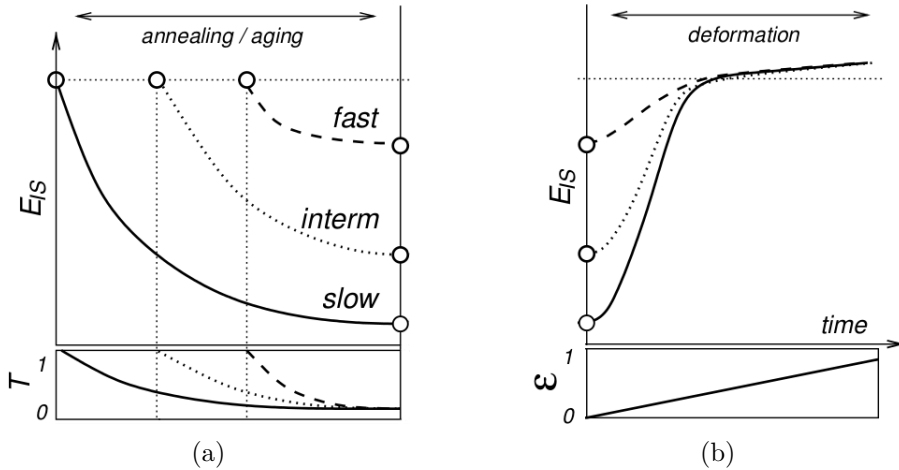


Figure 1.9: (a) Qualitative behavior of the energy per particle (here called  $E_{IS}$ ) as a function of time obtained by lowering the temperature at different rates (the  $T$ ) and mapping the system onto its associated inherent structure. The lower panel shows the form of  $T$  in time. The slowest quench yields the lowest final energies. (b) Energy per particle as a function of strain (here called  $\epsilon$ ) obtained starting from the samples quenched at different shear rates in (a) and increasing the value of shear strain. From [46].

### Average $U$ of glasses obtained by cooling from finite $T$ to 0 at finite rates

In [46], a binary mixture of Lennard-Jones particles equilibrated at temperature  $T$  is quenched to some lower temperature  $T_0 < T_g$  at a finite rate. As schematized in Figure 1.9a, faster cooling rates bring, at the end of the quench, to configurations of higher potential energy, whereas slower rates are more efficient in bringing the system in regions of the landscape with lower energy. Incidentally, samples quenched infinitely fast from equilibrium states at low  $T$  in [45] can be associated to the glassy states obtained by slow cooling in [46], and a similar relationship exists between the states quenched infinitely fast from high  $T$  and those which undergo fast cooling in [46]. In this way the results in [46] and [45] can be compared.

### Effect on $U$ of deformation of glasses obtained by cooling at finite rates

After having obtained glassy samples at  $T_0$  with different cooling rates, authors in [46] shear their samples at zero temperature, with a protocol that will be described in detail in chapter 2. The potential energy of their samples increases with increasing strain  $\gamma$ , so that samples visit states whose energies are equal to those that they had in earlier and earlier stages of the aging process. The authors thus observe that, at least by judging from the value of the potential energy, samples seem to undergo *rejuvenation* under deformation.

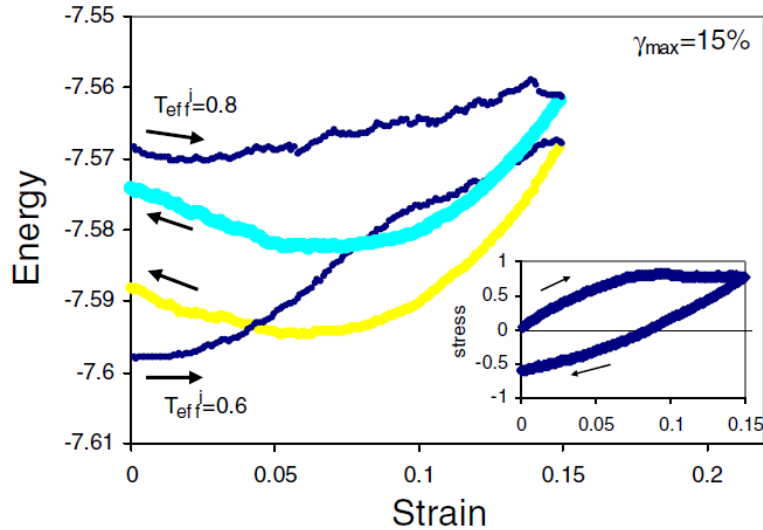


Figure 1.10: (Main panel) Energy per particle as a function of strain in an athermal quasi static deformation of a Lennard-Jones mixture, by varying the strain from 0 to  $\gamma_{max} = 0.15$  and back to 0 again, for two samples obtained by quenching equilibrated configurations at  $T = 0.8$  and  $T = 0.6$ . The sample at initial lower effective temperature rejuvenates (yellow data) after a semicycle of deformation, whereas the sample at initial higher effective temperature overages (cyan). In the inset, the value of the stress component in the plane of shear deformation is plotted as a function of the shear strain. The value of the stress as the strain is decreased back to zero (the *residual stress*) is negative. This means that deformed samples can be distinguished from undeformed ones. From [45].

#### Effect on $U$ of cyclic deformation of glasses obtained by cooling at infinite rates

In [45], authors perform deformation of samples as zero temperature similar to those in [46]. Differently from [46], the initial states are obtained by quenching at an *infinite rate* samples equilibrated at different temperatures  $T$ . In addition, rather than performing a simple shear deformation with monotonically increasing strain, authors in [45] perform a single semicycle of shear deformation, where the strain is incremented from 0 to  $\gamma_{max}$  and then decreased back to 0. In their case, again, the average potential energy of their samples is also seen to change with the deformation, and at the end of the semicycle the energy is observed to be higher or lower than the initial one (see Figure 1.10).

Coherently with what is reported in [46], they name the first behavior *rejuvenation* and the second *overaging*. The presence of rejuvenation or overaging after a semicycle is seen to depend on the strain amplitude  $\gamma_{max}$  (with higher  $\gamma_{max}$  correlating with rejuvenation, whereas lower  $\gamma_{max}$  usually resulting in overaging) and the effective temperature  $T$  of the initial samples (with lower effective  $T$  correlating with rejuvenation, and higher  $T$  leading to overaging). However, rejuvenated and overaged states are seen in [45]

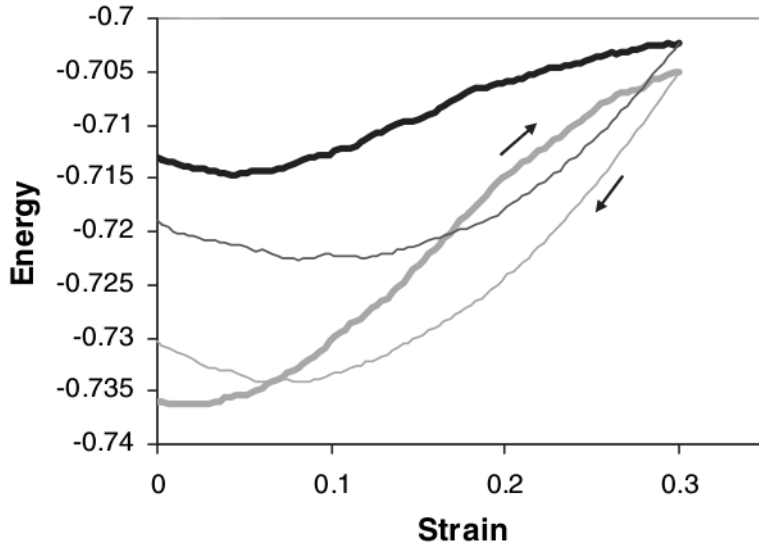


Figure 1.11: Energy per site as a function of strain in an athermal quasi static deformation of a NK system, by varying  $\gamma$  from 0 to  $\gamma_{max} = 0.3$  and back to 0 again, for samples at two different effective temperatures. The sample at initial lower effective temperature rejuvenates after a semicycle of deformation (gray data), whereas the sample at initial higher temperature overages (black). Note the similarity with what is observed in Figure 1.10. From [47].

*not* to be equivalent to undeformed samples with the same potential energy. This is verified by comparing the distribution of the eigenfrequencies for deformed samples and undeformed ones. The average values of the eigenfrequencies do not coincide for the two sets of samples, and the value of the stress component in the plane of deformation at zero strain is different from zero for deformed samples (see inset in Figure 1.10).

### 1.2.3 Rejuvenation and overaging in the NK model

Overaging and rejuvenation under the effect of deformation at zero temperature have been studied on systems characterized by a strain-dependent energy [47] which are not composed by interacting particles. In [47] authors consider a discrete model, namely the NK model, and study the effect that deformation has on it. The NK model will be described in detail in section 4.1. It does possess an energy landscape, but apart from this it has little to no resemblance to the particle models studied in [45, 46]. Nevertheless, it exhibits qualitatively the same energy behavior under oscillatory deformation observed in particle systems in [45] (see Figure 1.11). Given the striking agreement between Figure 1.11 and Figure 1.10 for data relative to the NK model and particle systems, it is interesting to determine whether the same agreement holds in the case of an arbitrarily long series of cyclic oscillations, rather than in that of a single cycle only. This issue is explored in chapter 4.

#### 1.2.4 Coarse-grained approach to the deformation of amorphous solids

Considerable effort has also been put into the understanding of the microscopic origins of the macroscopic mechanical properties listed in subsection 1.1.2, with special attention to the behavior beyond the elastic limit, which is critical for applications. In particular, recently theoretical work has been carried out so to build a framework comparable to that that is able to describe deformation in crystalline solids. In the case of crystalline solids, plastic deformation can be rationalized by the nucleation, motion and interaction of crystal defects such as dislocations [48, 49]. Established models of interactions between dislocations in crystals exist, which can be connected to finer-grained atomistic simulations [50], but this is not yet the case for amorphous solids. An attempt to fill this gap is represented by the shear transformation zone (STZ) theory [51], preceded by other models [52, 53].

The STZ theory assumes that the bulk of the material is populated by some number  $\Lambda$  of structural fluctuations that are capable to “transform” (change their state) as a shear stress  $\sigma$  is applied to the sample. In the STZ theory, the density of such fluctuations depends on an “effective disorder” parameter  $\chi$ , and  $\chi$  is also dependent on  $\sigma$  and the temperature  $T$ . In turn  $\sigma$  can be related to the strain  $\gamma$  via a linear proportionality related to the elastic modulus of the material  $\mu$ . The above relations constitute a set of coupled equations of the evolution of the applied strain  $\gamma$ ,  $\sigma$ ,  $\Lambda$ ,  $\chi$ , which can be solved as a function of the time  $t$  for a given applied strain profile  $\gamma(t)$ . In this way, one can thus determine [54] the relation existing between the strain and the stress for oscillatory deformation simulations like those performed in [45], and like those that are presented in the next chapters.

## 1.3 Oscillatory driven suspensions, memory effects

### 1.3.1 Results on non-brownian suspensions relevant for this work

One of the aims of this thesis is to compare the behavior exhibited by oscillatory sheared glasses in simulations like those listed in subsection 1.2.2 to that observed in oscillatory deformation experiments of a completely different system: a suspension of dilute non-brownian particles. The idea is to explore the similarities (if any) and differences between the two classes of systems.

An example of suspension of dilute non-brownian particles is given by the system studied in [55]. In [55], solid beads of polymethylmethacrylate of size  $\approx 200 \mu\text{m}$  are immersed in a viscous solution of water and surfactants. The beads and the surrounding medium have the same density (so that the weight of the particles is balanced exactly by buoyancy) and the same index of refraction (so to reduce as much as possible attraction due to Van der Waals forces). The particles are also big enough so that Brownian motion is absent. The resulting suspension is sheared repeatedly in an oscillatory way, up to some amplitude  $\gamma_{max}$ . Upon shearing and in the absence of collisions between them, particles

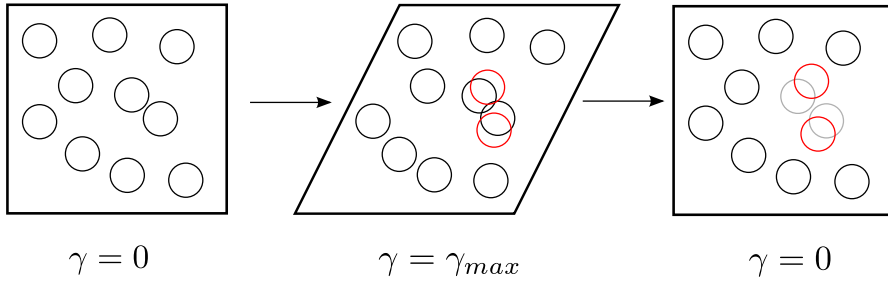


Figure 1.12: Schematic of the dynamics of the system in [55] in the course of a deformation semicycle. The system is affinely shear deformed up to some maximum value  $\gamma_{max}$ , according to Equation 1.9. Some of the particles come in contact in the course of such deformation. Those which do are labeled in red and named *active* (see text). Active particles are displaced randomly right after the collision. At the completion of a deformation semicycle, the result is that particles that haven't experienced any collision do get back to the position they started from, whereas the active ones are displaced from their original position (labeled in gray).

move in such a way that the coordinates  $\mathbf{r}_i$  of the center of particle  $i$  transform according to the affine map:

$$A\mathbf{r} = \mathbf{r}' \quad (1.8)$$

$$\begin{pmatrix} 1 & \gamma & 0 \\ 0 & 1 & 0 \\ 0 & 0 & 1 \end{pmatrix} \begin{pmatrix} x \\ y \\ z \end{pmatrix} = \begin{pmatrix} x + \gamma y \\ y \\ z \end{pmatrix} \quad (1.9)$$

where  $\gamma$  is a periodic function of time. In that case the motion is clearly reversible and the particles move in orbits which are retraced over and over again. However, if two particles become in contact in the course of the deformation, they interact irreversibly and do not retrace the trajectory followed before. This behavior can be modeled (see [55] and Figure 1.12) by assuming that particles move according to Equation 1.9 as long as no collisions occur and are displaced in a random way whenever they collide.

If samples are let evolve according to this dynamics and are observed stroboscopically at  $\gamma = 0$ , one can distinguish two different kinds of particles, by comparing the configurations of the system assumed before and after a deformation cycle:

- some of the particles won't change their position. These are the particles which haven't experienced any collision in the shear oscillation cycle.
- the rest of the particles will move, because they have collided in the course of the cycle, and we refer to them as *active*.

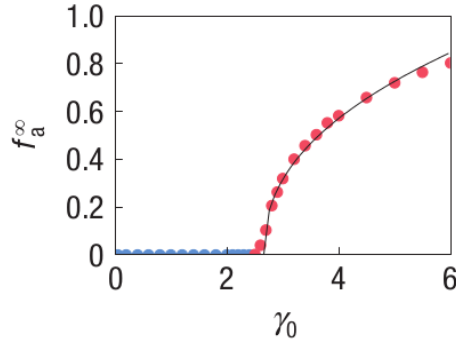


Figure 1.13: Fraction of active particles (see text) observed after a large number of oscillation cycles (larger than some characteristic  $\tau$ ) as a function of the oscillation amplitude (here indicated with  $\gamma_0$ ) in a model of a sheared suspension (see text). A transition at some value  $\gamma_c$  is observed. From [55].

#### Existence of a transition amplitude $\gamma_c$

An interesting transition in behavior is observed if a large number of shear oscillations is performed:

- for values of  $\gamma_{max}$  below some threshold value  $\gamma_c$ , after some average characteristic number of oscillations  $\tau_-(\gamma_{max})$ , the system reaches a state where *no particle is active*. This is because random collisions bring the system to states such that no particles collide in the course of a shear cycle. Such quiescent states are named *absorbing*.
- for values of  $\gamma_{max}$  above the threshold value  $\gamma_c$ , instead, a fraction  $f_a$  of the particles is always active, and the systems never seem to reach an absorbing state. Additionally,  $f_a$  seems to approach an asymptotic value in a characteristic number of oscillations  $\tau_+(\gamma_{max})$ , and thus the system reaches a *stationary* state (at least by judging from the value of  $f_a$ ). The  $f_a$  measured in a stationary state depends on  $\gamma_{max}$  (see Equation 1.10).

Experimental data on  $f_a$  in a 3D system and in simulations of a 2D system [55] do yield the form

$$f_a(\gamma_{max}) = \begin{cases} 0 & \text{if } \gamma_{max} < \gamma_c \\ (\gamma_{max} - \gamma_c)^\beta & \text{if } \gamma_{max} \geq \gamma_c \end{cases} \quad (1.10)$$

This behavior, observed in the 2D simulations in [55], is displayed in Figure 1.13.

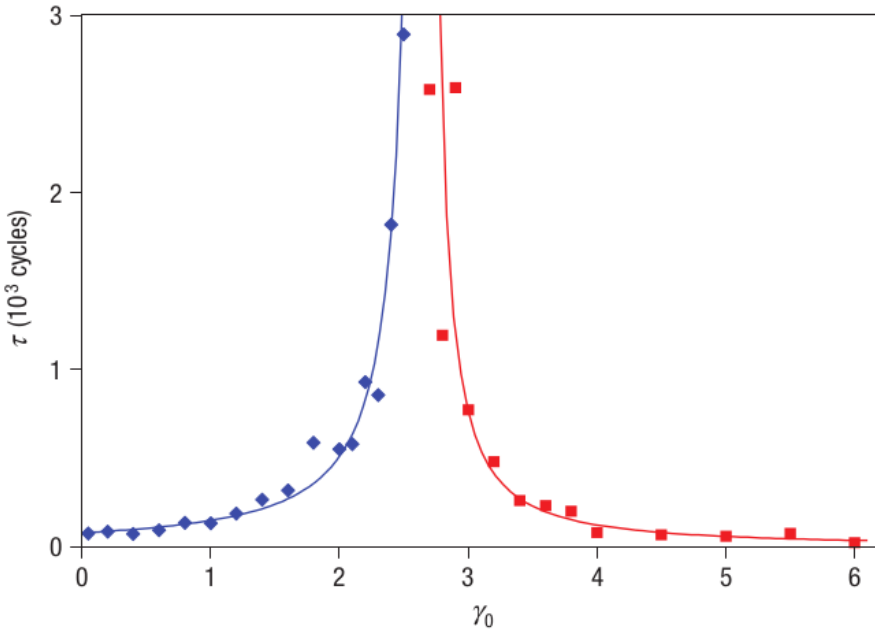


Figure 1.14: Characteristic number of shear oscillations  $\tau_-$  (blue) and  $\tau_+$  needed to the the number of active particles in the model colloidal suspension in [55] to approach a constant value as a function of the oscillation amplitude. At some value  $\gamma_c$   $\tau$  is seen to diverge. From [55].

In addition, the values of the characteristic numbers of oscillations  $\tau_{\pm}(\gamma_{max})$  seem to follow, in the same cases, the dependence

$$\tau_{\pm}(\gamma_{max}) = |\gamma_{max} - \gamma_c|^{-\nu_{\pm}} \quad (1.11)$$

signalling a divergence of the number of oscillations  $\tau_-$  needed to reach an absorbing state below  $\gamma_c$  and  $\tau_+$  needed to reach a stationary state above  $\gamma_c$ . This behavior, observed in the 2D simulation in [55], is displayed in Figure 1.14. The values of the exponents  $\beta$  and  $\tau_{\pm}$  can be obtained theoretically [56] in 2D and 3D, and have been suggested to be those that pertain to the universality class of conserved directed percolation [57].

### Memory effects

From what has been said above, if an experimenter shear deforms a suspension of the kind described in subsection 1.3.1 in a cyclic way up to some value  $\gamma_1 < \gamma_c$ , the system eventually reaches a final absorbing state which it can't leave. It turns out that if such a final state is handed to some other experimenter, she can determine the amplitude  $\gamma_1$  from simple measurements on the sample. To understand this, one can note that as the sample is in an absorbing state for oscillations of amplitude  $\gamma_1$ , any shear deformation cycle of amplitude  $\gamma_r < \gamma_1$  will leave the sample unaltered. This is because if no

### 1.3. Oscillatory driven suspensions, memory effects

---

collision occurs during a shear deformation cycle of amplitude  $\gamma_1$  (which is the necessary condition for the state to be absorbing for that amplitude) no collision can occur for any deformation of a smaller amplitude<sup>6</sup>. As soon as  $\gamma_r$  is raised above  $\gamma_c$ , however, collisions *can occur*, and the configuration of the system can be modified by a single cycle of shear deformation. All of the above can be exploited so to *read* the value of  $\gamma_1$ : one simply needs to apply cyclic shear deformation to the samples starting from an amplitude  $\gamma_r = 0$ , perform wider and wider oscillations and measure the fraction of active particles. Initially the sample will be unaltered (with zero active particles), but for some value  $\gamma^* \geq \gamma_c$  the system will be perturbed (with nonzero active particles). This is shown in Figure 1.15a in the curve which represents the fraction of active particles in samples which have undergone  $\approx 55000$  shear oscillations at  $\gamma_1 = 3$ . The value of  $\gamma^*$  is an *upper bound* for  $\gamma_1$ , and can be considered a good approximation of it.

From all of this one can conclude that if a first experimenter *trains* a sample by shearing it cyclically, a second one can *read* the value of the amplitude of the training oscillations in the way described above. The samples are thus able to store a *memory* of their mechanical history.

The fact that the approach to an absorbing state is exponential (described by  $\tau_-$ ) has an important consequence. Let's consider a collection of samples, on which an experimenter performs a number  $\tau < \tau_-$  of oscillations of amplitude  $\gamma_1$ . The training of the samples will be, so to say, “incomplete”: this means that some of the samples will reach an absorbing state for  $\gamma_1$ , and others will not. A “reading experiment” will be able to reveal the value of  $\gamma_1$ , by measuring a “kink” in the average number of active particles  $f_a$  as a function of  $\gamma_r$ , due to the signal from the samples that have reached an absorbing state for  $\gamma_1$ . An example of such a kink is evident in the curves in Figure 1.15a relative to incomplete trainings (those labeled with a number of oscillations  $\leq 1000$ ). If such “partially trained” collection of samples is now cyclically shear deformed up to  $\gamma_2 < \gamma_1$ , after some cycles some of the samples will become absorbing for  $\gamma_2$ . The collection of samples will thus be divided in three sets at that point: *a*) absorbing states for  $\gamma_2$ , but which are not absorbing for  $\gamma_1$ ; *b*) absorbing states for  $\gamma_1$  (absorbing *also* for  $\gamma_2$ ); *c*) states that are not absorbing neither for  $\gamma_2$  nor for  $\gamma_1$ . A “reading experiment” measuring  $f_a$  as a function of  $\gamma_r$  will thus show two kinks in correspondence of  $\gamma_1$  and  $\gamma_2$ . This procedure can be generalized to more training amplitudes  $\gamma_1 > \gamma_2 > \dots$ , and proves that these kinds of systems are able to store *multiple* memories.

In [58], multiple memories are encoded in samples by training them alternating a small number oscillations of different amplitudes, so that the strain  $\gamma$  of the sample varies in cycles  $0 \rightarrow \gamma_1 \rightarrow 0 \rightarrow -\gamma_1 \rightarrow 0 \rightarrow \gamma_2 \rightarrow 0 \rightarrow -\gamma_2 \rightarrow 0$ . The result of a reading operation on samples treated this way is shown in Figure 1.15b. Moreover, such multiple memories are shown to be *transient*, that is they're erased if the training is long enough. This is because oscillations of amplitude  $\gamma_1$  make the system evolve to absorbing states for this amplitude, and the amplitudes  $\gamma_i < \gamma_1$  are unable, by construction, to destabilize

---

<sup>6</sup>This fact is called “ordering of reversible states” in [58].

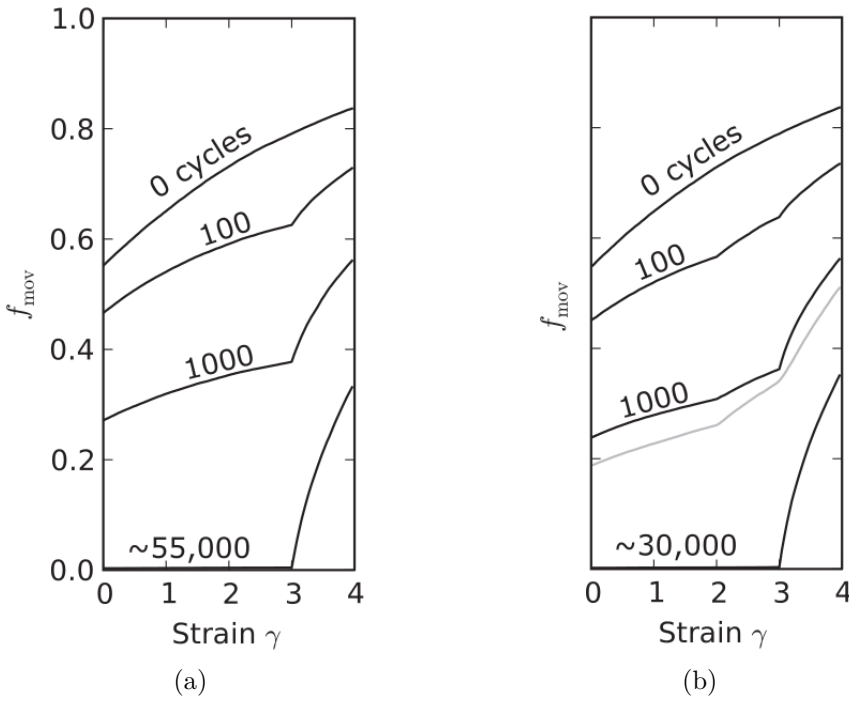


Figure 1.15: (a) Number of active particles as a function of the reading amplitude (here labeled with  $\gamma$ ) for a model of suspension subjected to a series of oscillations of amplitude  $\gamma_1 = 3$  and of different durations (specified next to the curves). The reading reveals the presence of memory of the initial training, and for a large number of oscillations no active particles are observed in the reading below  $\gamma_1$ . (b) In black: number of active particles read from samples trained by a series of oscillations alternating two different amplitudes  $\gamma_1 = 3, \gamma_2 = 2$ . The trace of a double memory of the training is evident but for the longest training. The multiple memory is transient. In gray: number of active particles subjected to a very long training alternating two oscillations amplitudes and adding noise in the dynamics. The multiple memory is still present, and is thus stabilized by the noise. From [58].

such absorbing states. The effect of a long series of alternated oscillations of multiple amplitudes  $\gamma_1 > \gamma_2 > \dots$  is thus to produce a set of absorbing states for the largest amplitude  $\gamma_1$  only, that retain no memory of the smaller amplitudes. This is evident in Figure 1.15b in the reading of samples trained with  $\approx 30000$  shear oscillations.

The erasure of the memory left by training at amplitudes smaller than  $\gamma_1$  can be avoided via the addition of a simple ingredient: noise. In [58], authors show that by adding a random perturbation to the trajectories, so that they “wiggle” around the path prescribed by Equation 1.9, multiple memories can be stabilized. The consequence of the addition of such noise is that cycles of smaller amplitudes are able to destabilize absorbing states for larger amplitudes, making multiple memories *persistent* under the application of an indefinitely large number of training cycles. The result of a reading experiment on a system subjected to a large number of alternating cycles with two amplitudes  $\gamma_1$  and  $\gamma_2$

in the presence of noise is shown in Figure 1.15b, in gray.

## 1.4 Summary

In the previous paragraphs we have briefly outlined the main features of metallic glasses, considering their mechanical properties and their formation. Metallic glasses are a subclass of materials in the larger family of glasses, and thus their properties can be studied (at least qualitatively) with theoretical and simulation techniques developed to describe glassy systems.

Simulations of oscillatory shear deformation performed in the past show that glassy systems rearrange so to change their potential energy under applied strain [45, 46]. In particular, *rejuvenation* and *overaging* are observed by analyzing a *single* cycle of shear deformation in Lennard-Jones models. It is however unclear what is the potential energy behavior of samples subject to a *large* number of deformation cycles, like in fatigue experiments in which a cyclic load is applied on a sample. This issue is explored in the chapters that follow.

It is interesting to ask also how particles composing a system deformed in the way described above *move* in the course of deformation. This kind of dynamics has been investigated in the case of shear deformed dilute noncolloidal suspensions [55], which show a *non-equilibrium transition* in the motion of the suspended particles as a function of the oscillatory deformation amplitude. In the following chapters (among the rest) we will explore similarities between the phenomenology observed in noncolloidal suspensions and particle models of glassy systems.



## 2 Particle models and simulation of amorphous solids

One way to understand macroscopic systems is to trace back their behavior to the particles that constitute them. Here we describe in detail the features of the Lennard-Jones model, which is the main workhorse used in this thesis to get insights about the mechanical behavior of glassy systems under oscillatory shear. The numerical techniques employed to study it are also presented, with an emphasis on those that aim at describing the behavior of systems under deformation. The most important concept explored in this chapter is the evolution of energy landscapes and inherent structures as strain is changed. This will be the key tool to interpret the results of simulations of LJ systems in chapter 3 and to develop new models in chapter 4.

### 2.1 Lennard-Jones model for glassy systems

In this thesis, we model glassy systems using an isotropic and pairwise additive potential, as in [45, 46]. More precisely, in what follows we will employ binary mixtures of classical particles interacting via a Lennard-Jones pair potential of the form

$$\phi_{\alpha\beta}(r) = 4\epsilon_{\alpha\beta} \left[ \left( \frac{\sigma_{\alpha\beta}}{r} \right)^{12} - \left( \frac{\sigma_{\alpha\beta}}{r} \right)^6 \right] \quad (2.1)$$

which has been extensively used in numerical and simulation work to probe and reproduce the behavior of glassy systems. While a model of this kind cannot reproduce quantitatively the properties of real amorphous materials, it still aims at capturing their behavior at a qualitative level.

By changing the parameters in Equation 2.1, one can embody in the model two out of the three features listed in subsection 1.1.1 that characterize a good metallic glass former. In fact, by varying the value of the matrix  $\sigma_{\alpha\beta}$ , one varies the range of the repulsive cores of the Lennard-Jones particles, thus changing their effective sizes. By varying the value of  $\epsilon_{\alpha\beta}$ , instead, one can tune the energy gain obtained when particles

of different species are close together. Such value is related to the enthalpy of mixing, which is another key factor that influences glass forming behavior. Indeed, it has been shown that a careful choice of  $\sigma_{\alpha\beta}$  and  $\epsilon_{\alpha\beta}$  allows binary Lennard-Jones systems at low temperature to avoid crystallization [59] for a sufficiently long time and exhibit behavior typical of glasses such as a dramatic slowdown of particle diffusion and the breakdown of the Stokes-Einstein relation between viscosity and diffusion in Equation 1.2 [60].

## 2.2 Computer simulation of particle systems

### 2.2.1 Molecular dynamics at constant $E$ or $T$

A system of  $N$  particles interacting via a pairwise additive potential like that in Equation 2.1 has a total potential energy

$$U(\mathbf{r}_1, \dots, \mathbf{r}_N) = \sum_{i=1}^N \sum_{j < i} \phi(|\mathbf{r}_i - \mathbf{r}_j|) \quad (2.2)$$

This value of  $U$  can be changed by some amount  $\Delta U$  in the presence of an external field (see Figure 2.1). Moreover, if such a field depends on the position of the particles, then the perturbation can be written as  $\Delta U(\mathbf{r}_1, \dots, \mathbf{r}_N)$ .

The forces acting on each  $i$ -th particle are known once that a configuration is specified:

$$\mathbf{f}_i = -\nabla_{\mathbf{r}_i} U(\mathbf{r}_1, \dots, \mathbf{r}_N) \quad (2.3)$$

where differentiation is performed with respect to the coordinates of the  $i$ -th particle that compose the vector  $\mathbf{r}_i$ . If the positions  $\{\mathbf{r}_i\}$  and velocities  $\{\dot{\mathbf{r}}_i\}$  are specified at a given moment in time  $t_0$ , the evolution of the system can be determined by integration of the Newton law:

$$\mathbf{f}_i = m_i \ddot{\mathbf{r}}_i \quad (2.4)$$

In practice, the integration of Equation 2.3 and Equation 2.4 (also called the *n-body problem* of classical mechanics) is too hard to be performed analytically even for the simplest interaction potentials if the number of particles is large. Fortunately, numerical techniques exist that are able to give approximate solutions of it (these are generally referred to as *molecular dynamics* (MD) methods [7, 61]). The idea behind these methods is to compute the trajectories of the particles by updating their coordinates according to their velocities as time is increased in small discrete intervals of duration  $dt$  (timesteps). One of the simplest and most effective integration schemes is the *velocity-Verlet* scheme [61], which has the desirable property of being time reversible (so that trajectories are retraced if the velocities are reversed at a given moment in time) and

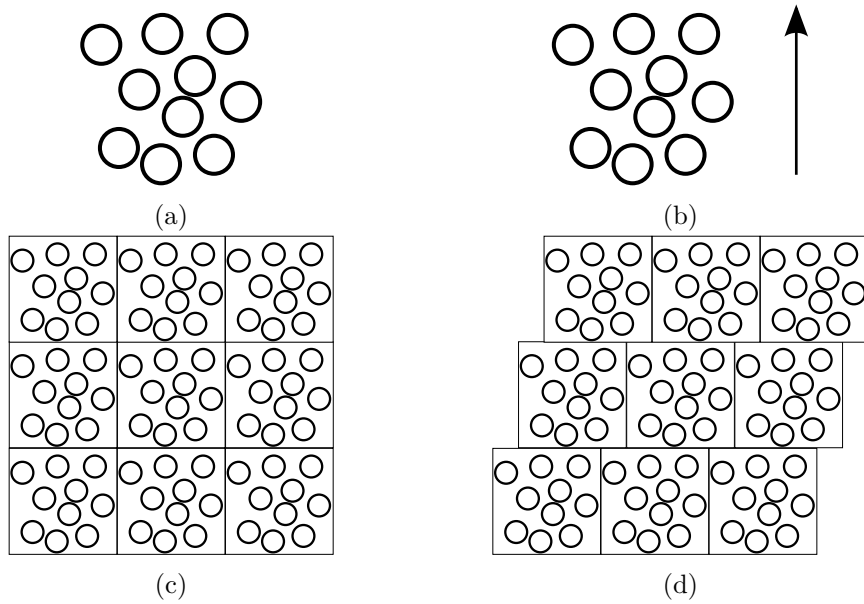


Figure 2.1: Schematic representation of systems of particles in different environments: (a) interacting particles with open boundary conditions; (b) interacting particles with open boundary boundary conditions and immersed in a field; (c) interacting particles with periodic boundary conditions. This is a special case of (b), but with the field generated by the particles *themselves*; (d) interacting particles with Lees-Edwards boundary conditions. This is another special case of (b), but with the field generated by the particles. Clearly, in this case the energy of the configuration will depend on the offset in the position of the simulation boxes.

of preserving volumes in phase space during the evolution, as required by Equation 2.3 and Equation 2.4 [61]. Such integration algorithms can be implemented using a programming language of choice, so that one is able to simulate the behavior of a system of interacting particles using a computer (or a group of computers). Nowadays several computer codes that perform the computation above are readily available. In order to do so efficiently, several “tricks” can be employed. First of all the real systems of interest are usually macroscopic in size, and are thus constituted by a very large number of particles  $> 10^{20}$ . Dealing explicitly with such a huge number of particles is not possible, as the sheer amount of memory needed to store the positions of such a large set of particles surpasses by far the capacity of ordinary computer systems. Luckily, there are ways to partially overcome this. A macroscopic system can be divided in parts (in three dimensions, each of these can be thought as the part of the system contained in a small cubic box, called *simulation box*). To simulate what happens in one of these boxes, one replaces the rest of the system that surrounds it with *identical copies* of it (as displayed schematically in Figure 2.1c and Figure 2.1d), called “images”. In this way particles at the boundaries of the box “feel” an environment that is similar to that they would experience in the bulk. This is accomplished at a very small cost, that is by computing the additional interactions between particles separated by the boundaries of

the box, and applying the so called “minimum image convention” [61]. This approach is not without drawbacks, as it tends to introduce spurious correlations. However, it can be used to obtain meaningful results by studying a relatively small number of particles (typically, in the range between  $10^2$  to  $10^6$ ). Note also that the periodic replicas of the particles can be viewed as sources of an external field acting on the particles contained in the simulation box. It’s then evident that the boundary conditions do contribute in shaping the features of the potential energy landscape of the system (this is clearly evident in Figure 2.1d, where the *exact* same configuration will have a different energy as the offset in the position of the boxes is varied).

Another source of problems comes from the fact that the calculation of the forces from Equation 2.3 for a pairwise additive potential like that in Equation 2.1 would in principle require the computation of  $N(N - 1)/2 \approx N^2$  forces. The computational complexity of the problem is thus polynomial in  $N$ , but one would like to have an exponent lower than 2. This is doable by neglecting the interactions between particles separated by a distance which exceeds some cut-off, and thus computing the force acting on a given particle as if it was generated only by the particles closest to it. If a list of neighboring particles can be generated, the complexity is reduced to that of the computation of just  $dN$  interactions, where  $d$  is the average number of neighbors surrounding each particle. The construction/rebuilding of the lists (cell lists or Verlet lists) [61] of neighboring particles often requires less than  $N^2$  operations or doesn’t need to be performed frequently, and thus the overall cost of the computation can be greatly reduced in the case of large systems [61].

In Equation 2.3, one assumes that the forces that act on the system are internal, so that it is isolated and its total energy  $E = K + U$  (where  $K$  is the kinetic energy) is conserved. However, experimental systems are very rarely isolated from their environment. In real experiments what is kept constant is usually the temperature  $T$  and the volume  $V$  or the pressure  $p$  via a contact with an external reservoir and it is crucial to be able to construct simulations capable to match experiments. The naive approach of simulating both the system of interest and a reservoir is too demanding in terms of computational resources to be feasible. For this reason, to deal with systems where the variables  $N, V, T$  or  $N, p, T$  are kept constant (and sample the canonical and isobaric ensembles respectively), other numerical schemes have been devised, respectively named thermostats and barostats [61]. Two popular choices of thermostats for simulations at constant  $N, V, T$  are represented by

- The Berendsen thermostat
- The Nosé-Hoover thermostat

Both thermostats are described in [62], and aim at making the trajectory of the system visit configuration with a probability compatible with the canonical ensemble [61].

In this work the Nosé-Hoover thermostat is employed to study systems at a specified temperature  $T$ .

### 2.2.2 Simulation of deformation

Another way (rather than imposing some temperature  $T$ ) to alter experimentally a sample is imposing a deformation on it. An example is a simple shear deformation of the kind described in Equation 1.9. Geometrically, such transformation maps a cube with edges parallel to the  $x, y, z$  axes onto a rectangular prism whose faces parallel to the  $xy$  plane are parallelograms, as depicted in Figure 2.2.

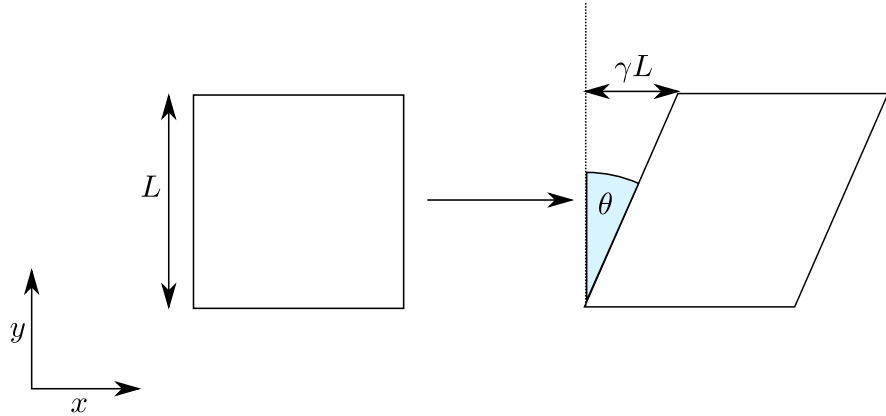


Figure 2.2: Shear deformation of a rectangular box under the effect of a shear deformation of the kind described in Equation 1.9, and disregarding the effect on the  $z$  direction. The effect of the shear is tilting the box by an angle  $\theta$  such that  $\tan \theta = \gamma$ , and the transformation conserves the volume.

As the determinant of the matrix in Equation 1.9 is equal to 1, the transformation is volume-conserving. A macroscopic deformation of this kind can be implemented in a computer simulation by applying the transformation in Equation 1.9 to the simulation box and its images, by means of the so-called Lees-Edwards boundary conditions (shown schematically in Figure 2.3 and described in [7]).

In the Lees-Edwards boundary conditions the image boxes (and the particles included in them) are displaced during the simulation.

Simulation of deformation can be performed in several ways. In what follows we outline two possible approaches, differing by the role played by temperature  $T$  and shear rate  $\dot{\gamma}$ .

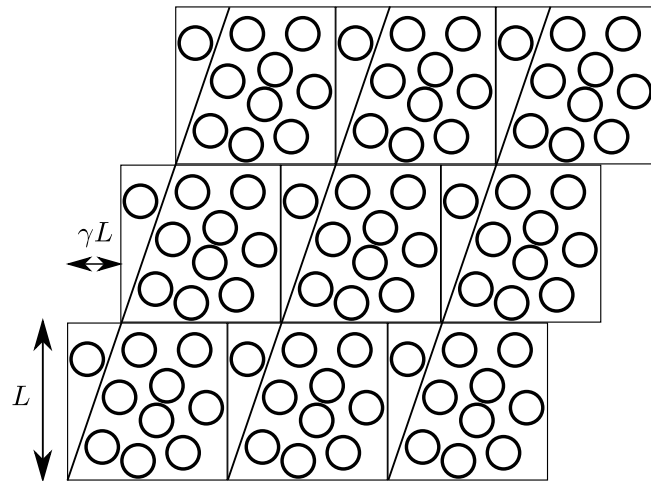


Figure 2.3: Schematic two-dimensional representation of the Lees-Edwards boundary conditions. The spatial arrangement of the particles can be interpreted in two ways: as particles in square boxes displaced by some offset  $\gamma L$  or as aligned boxes tilted by  $\theta = \arctan \gamma$ .

### Simulation of deformation at $T \neq 0$ and $\dot{\gamma} \neq 0$

In finite shear rate simulation, particles in the image boxes do drag those at the boundaries with some drift velocity  $\dot{\gamma}L$  (where  $\dot{\gamma}$  depends on the increment of  $d\gamma$  that is applied to the system at each  $dt$  molecular dynamics step) so that a velocity profile can be imposed to the system. Particles that cross the boundaries between images with non-zero relative velocity need to be re-inserted in the box at a position that depends on the value of strain  $\gamma$  and a velocity that depends on the difference in velocity between the box images [63]. Furthermore, by driving images by imposing a finite strain rate  $\dot{\gamma}$  work is done on the system, and is rapidly converted into kinetic energy. A coupling with a thermostat is thus necessary if the system is to be kept at a constant temperature  $T$  [63]. Several schemes of this kind have been devised to simulate systems at non-zero  $T$  and  $\dot{\gamma}$  and thus recover their transport coefficients, but their application lies outside the scope of this thesis.

Furthermore, one of the current limitations of these methods is that low shear rates are not easily accessible. This is because  $dt$ , if measured in real units and in the case of atomic solids, has to be very small (in the order of femtoseconds) in order to integrate properly the equation of motions of the atoms, and the maximum number of MD steps that can be performed in a reasonable timeframe (roughly in the order of weeks) is around  $\approx 10^9$  with the computing power available nowadays [64]. The consequence is that timescales reachable by MD lie in the microsecond range. Parallelization of ordinary MD algorithms can be successfully used to study *larger* systems, but not to access *longer* timescales. It's then clear that trying to simulate a shear deformation with low strain rate means choosing a  $d\gamma$  so tiny that the overall total strain  $\gamma$  reachable during the simulation is too small to be useful. Such limitation can be overcome by employing

### 2.3. Simulation of athermal quasi-static deformation

---

the athermal quasi-static deformation method described below.

#### Simulation of athermal quasi-static deformation (AQS) at $T = 0$ and $\dot{\gamma} \approx 0$

The athermal-quasi static (AQS) deformation procedure has been proposed in [65] and [66], following earlier methods used in [67] to overcome the shear rate limitations of ordinary MD, and it is the method of choice in this work. Within this approach particle velocities are completely disregarded. An undeformed system ( $\gamma = 0$ ) is initially in an inherent structure, obtained typically by means of an energy minimization procedure. Afterwards, a strain increment of  $d\gamma$  is imposed on the system through Lees-Edwards boundary conditions by displacing the upper and lower image boxes in Figure 2.3 and by applying the transformation in Equation 1.9. This has the effect of putting the system in a configuration that does not correspond to an energy minimum anymore. Finally, the system is drawn to a new inherent structure by another application of the energy minimization procedure. The operations above can then be repeated so to reach arbitrary values of strain in steps of  $d\gamma$ . This method turns out to be a reasonable model for systems satisfying two conditions:

1. Temperatures are low enough so that systems can be imagined as “rattling” around a single inherent structure. As this condition satisfied in the limit where  $T \rightarrow 0$ , this means that the system can be considered athermal.
2. Shear rates are low enough so that, once deformed, the system has time to relax to an inherent structure before further deformation is applied. Being this condition satisfied in the limit where  $\dot{\gamma} \rightarrow 0$ , one can consider the systems as deformed in a quasi-static way<sup>1</sup>.

Summarizing, the athermal quasi-static protocol represents the dynamics of glassy system at vanishingly low  $T$  and  $\dot{\gamma}$ .

## 2.3 Simulation of athermal quasi-static deformation

### 2.3.1 Effect of deformation on the energy landscape

The shape of the energy landscape of a system of  $N$  particles in a simulation box is dictated by Equation 2.2 and 2.1 and the boundary conditions. These in turn depend on the shape and volume of the box and on the spatial arrangement of the image boxes (see Figure 2.1). All these ingredients, in fact, contribute to shaping the exact form of the term  $\Delta U$  that must be added to the expression of  $U$  in Equation 2.2 (the energy that the particles would have if they were isolated in space) to get the total energy.

---

<sup>1</sup>the deformation is thus “adiabatic”, in the same spirit of the adiabatic approximation of quantum mechanics

What is the effect of deformation on the energy landscape of a set of particles contained in a simulation box connected to image boxes via Lees-Edwards boundary conditions? Image boxes can be regarded as sources of an external field for the particles located at coordinates  $(\mathbf{r}_1, \dots, \mathbf{r}_N)$  in the simulation box, as in Figure 2.1d. As the value of the offset in position  $\gamma L$  is changed, such external field is modified. This means that the value of the total potential energy is dependent on  $\gamma$ , and can be thus rewritten as  $U(\mathbf{r}_1, \dots, \mathbf{r}_N, \gamma)$ . The effect of deformation can be thought of, in general, as altering the topology of the energy landscape<sup>2</sup>. Some of the peaks and minimas of the landscape are thus changed by deformation, while some others are stable. The relevance of the changes of a given feature of the landscape is determined by the importance of the interactions of particles located at the boundaries of the simulation box with respect to those located in the bulk. This can be clarified with an example: consider a configuration such that two particles located deep inside the simulation box have their centers very close together. Due to the repulsive part of the pair potential in Equation 2.1 the contribution given by such a pair of particles to the potential energy in Equation 2.2 is very high, so to make this configuration close to a “peak” in the landscape. As the particles are not close to the boundaries, there is no way through which a change in the strain (by varying the  $\gamma$  in the Lees-Edwards boundary conditions) can change their relative distance, so that such configuration will always be close to a peak in the landscape, regardless the value of  $\gamma$ . Conversely, a peak due to close particles located in different image boxes can be eroded by deformation, because a change in the strain can separate them and thus reduce the value of their contribution to the total potential energy. Also, a configuration of relatively low energy for some value of the strain can become a peak in the landscape if, by varying  $\gamma$ , two particles at the boundaries come very close to each other.

### **Evolution of inherent structures under deformation**

What’s the fate of an inherent structure and its basin under deformation? For a given value of the strain  $\gamma$ , the energy landscape is fixed and presents a certain number of inherent structures  $\mathbf{R}_1^*, \dots, \mathbf{R}_M^*$  (where each  $\mathbf{R}_i^*$  stands for a  $3N$ -dimensional vector of the form  $(\mathbf{r}_1, \dots, \mathbf{r}_N)$ ). For a different value  $\gamma'$  the number of inherent structures  $\mathbf{R}_1^{*\prime}, \dots, \mathbf{R}_L^{*\prime}$  won’t be the same, because some structures get created or destroyed as the landscape changes as  $\gamma$  is varied. In what follows we will identify inherent structures of the landscapes associated to the values of the strain  $\gamma$  and  $\gamma'$  if, in the  $3N+1$ -dimensional space (configuration space + strain dimension  $\gamma$ ), there is a path connecting them such that each point in the path is an inherent structure for some value of the strain between  $\gamma$  and  $\gamma'$  (see Figure 2.4). We name “surviving” or “stable” inherent structures those in the sets  $\{\mathbf{R}_1^*, \dots, \mathbf{R}_M^*\}$  and  $\{\mathbf{R}_1^{*\prime}, \dots, \mathbf{R}_L^{*\prime}\}$  that are connected with such a path; we call “destroyed” those in the set  $\{\mathbf{R}_1^*, \dots, \mathbf{R}_M^*\}$  that are not connected with a path to any of those in  $\{\mathbf{R}_1^{*\prime}, \dots, \mathbf{R}_L^{*\prime}\}$ , and “created” those in the set  $\{\mathbf{R}_1^{*\prime}, \dots, \mathbf{R}_L^{*\prime}\}$  which are

---

<sup>2</sup>An intuitive picture of this is the effect of erosion/morphogenesis of the surface of the Earth.

### 2.3. Simulation of athermal quasi-static deformation

---

not connected to any of those in  $\{\mathbf{R}_1^*, \dots, \mathbf{R}_M^*\}$ . In Figure 2.4 each inherent structure follows a path in the  $3N + 1$  dimensional space.

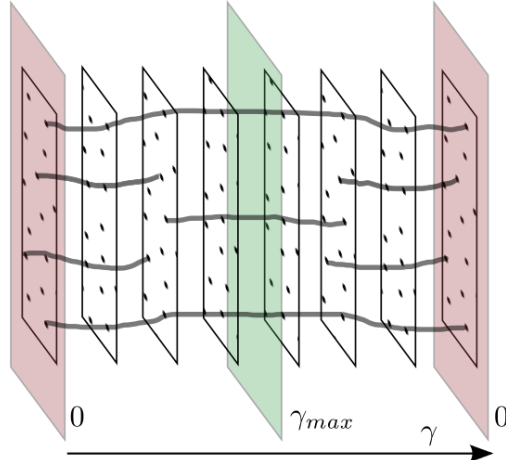


Figure 2.4: Schematic representation of the evolution of energy landscape in a “configuration space -  $\gamma$ ” diagram during a shear deformation semicycle. In this picture configuration spaces associated to a given value of  $\gamma$  are assumed to be two-dimensional, and each of them has a set of minima (indicated with black dots). As  $\gamma$  is increased and the landscape deforms the inherent structures will move in configuration space, tracing the trajectories represented in gray (to avoid clutter, only some of them are shown). Sometimes the inherent structures get destroyed, so that the lines are interrupted; conversely, as new local minima are formed, new trajectories are generated. Due to the reversal of the strain, the diagram is symmetric with respect to the plane of  $\gamma = \gamma_{max}$ .

What does determine the destruction of an inherent structure? Under strain the basin pertaining to a given inherent structure can shrink due to the changes in the landscape, with the inherent structure being closer and closer to the boundaries of the basin. The inherent structure (together with its basin) disappears upon colliding with a saddle point of the landscape [68]. Such collision has a corresponding hallmark in the Hessian matrix of the potential energy calculated at the inherent structure: right before the collision at least one of the eigenvalues of the Hessian matrix falls to zero [68]. The creation of an inherent structure is simply the inverse process of the destruction, and these two processes are represented schematically in Figure 2.5.

The destruction of an inherent structure can be also easily visualized in terms of the disconnectivity graphs introduced in chapter 1. During deformation, the disconnectivity tree of the landscape gradually changes, with leaves disappearing (as inherent structures and their basins are destroyed) and others forming, and connectivity between them changing. In particular, the process of destruction of a given inherent structure corresponds to the gradual shortening and final disappearance of the leaf associated to it in the graph.

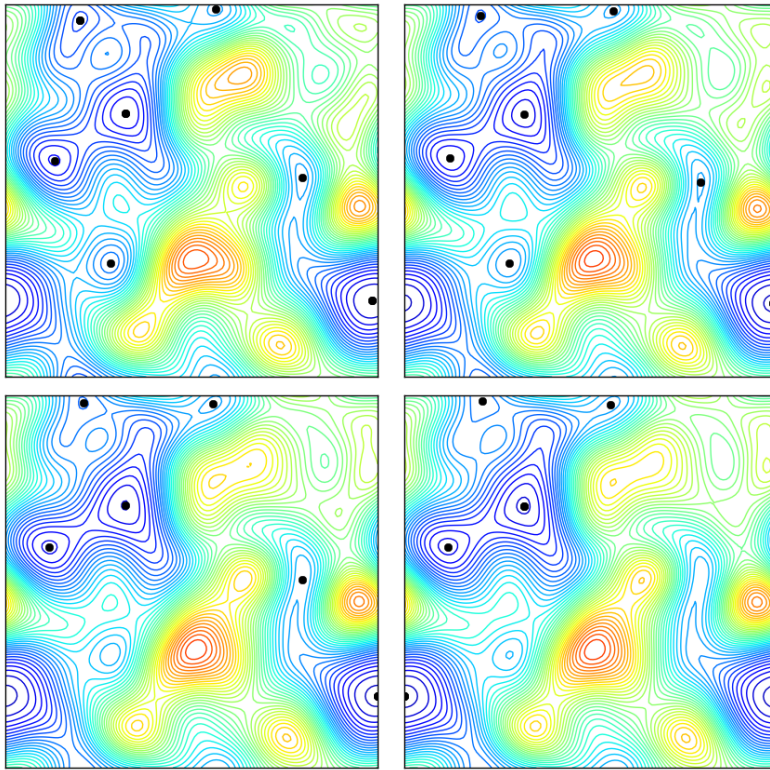


Figure 2.5: Schematic two-dimensional representation of the evolution of inherent structures changing the value of  $\gamma$ . This figure can be seen as a series of projections (or cuts at fixed values of  $\gamma$ ) of the diagram in Figure 2.4. As  $\gamma$  is varied, the energy landscape (represented by equipotential lines) changes and the inherent structures (black dots) move, or get destroyed or created accordingly.

### 2.3.2 Consequences for athermal dynamics

The way in which the energy landscape evolves during a deformation is intimately related to the evolution of a given starting state under the AQS protocol. For clarity this relationship is schematically illustrated in Figure 2.6, and can be analyzed at every elementary operation performed in an AQS step.

- (a) In the AQS protocol a system is initially in an inherent structure configuration (see Figure 2.6a).
- (b) An affine map of the kind in Equation 1.9 is applied to the coordinates by setting the incremental strain to  $d\gamma$ . At the same time, boundary conditions between the different images are accordingly updated, so that the energy landscape is slightly changed. In general, the new configuration won't be in a local minimum of the new modified landscape anymore, but slightly away from it<sup>3</sup> (Figure 2.6b).

---

<sup>3</sup>In this context, it's useful to note that  $d\gamma$  plays a crucial role in AQS dynamics. If too large,

### 2.3. Simulation of athermal quasi-static deformation

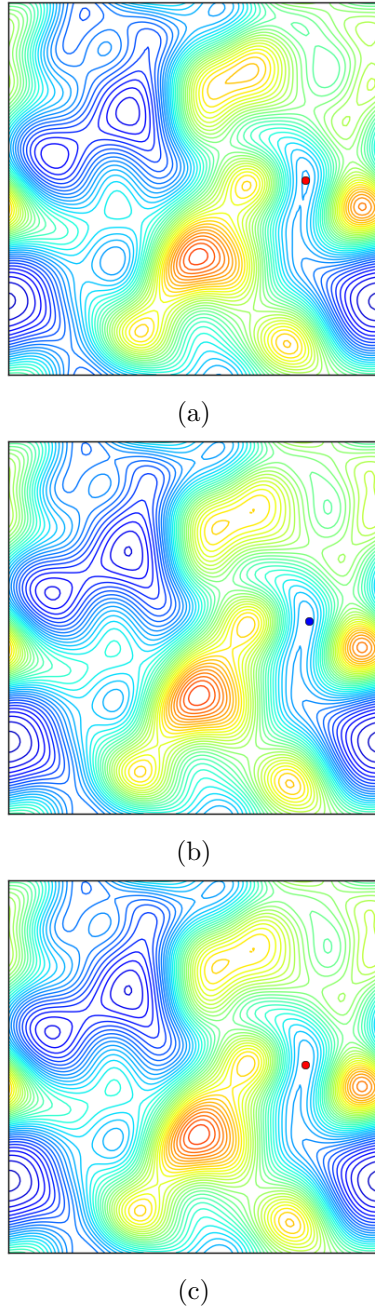


Figure 2.6: In this two-dimensional diagram the steps constituting AQS dynamics are represented. The system initially occupies an inherent structure (a). Subsequently, in (b), as the strain is increased by  $d\gamma$ , the landscape is deformed and the system is affinely deformed and is not in an energy minimum anymore. Another step of energy minimization allows to bring the system to a stable minimum (in this case, to the “same” inherent structure in the deformed landscape) again in (c), and another AQS cycle can start again.

- (c) A minimization routine is employed to bring the system back to an inherent structure of the deformed landscape (Figure 2.6c), and the procedure can be repeated.

During AQS deformation the system thus “travels” in configuration space in two different ways, represented schematically in Figure 2.7:

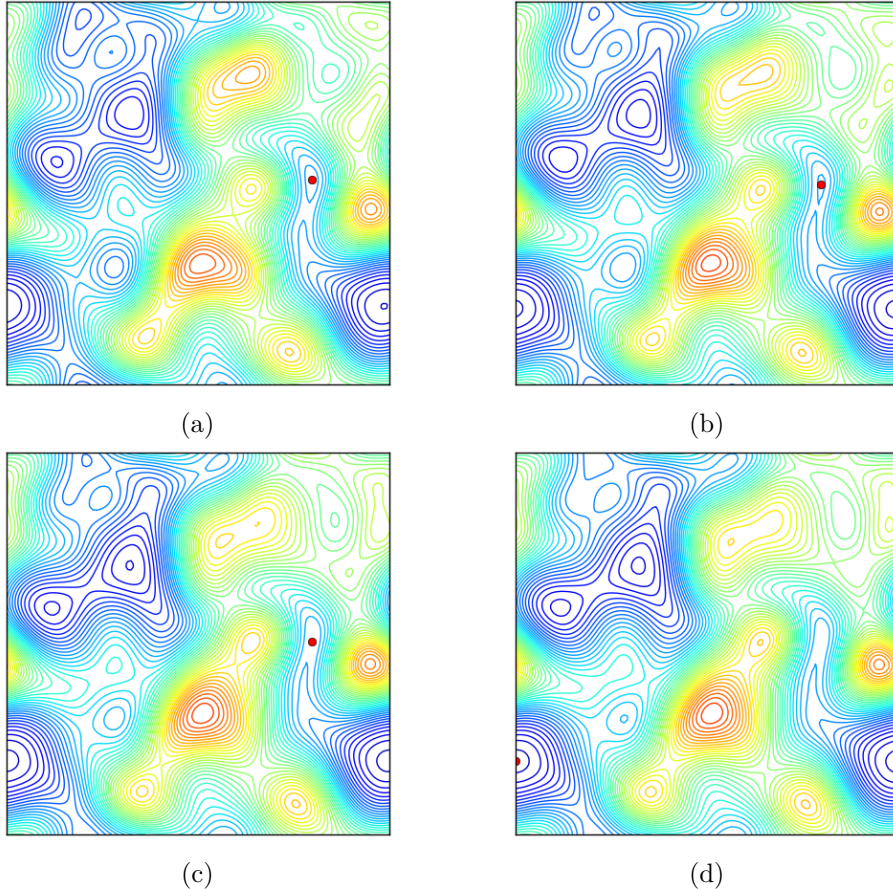


Figure 2.7: Schematic representation in 2D of the two ways in which a system can move in the energy landscape via AQS dynamics. From (a) to (c) the system moves in a continuous way following a single inherent structure as it evolves. When moving from (c) to (d), however, the inherent structure ceases to exist and the system undergoes a transition to another local minimum.

1. Most of the time (like from (a) to (c) in Figure 2.7), the system sits on the same inherent structure. Increasing the strain makes the inherent structure evolve fol-

the deformation of the landscape is dramatic (so that the correlation between the landscapes before and after the deformation is low) and the configuration is fired away in configuration space by the affine transformation, possibly jumping over several valleys and peaks. This is clearly not what AQS is supposed to do, as the system is supposed to follow the changes in the landscape in an “adiabatic way”. So  $d\gamma$  has thus to be small enough to gradually decorrelate the energy landscape and gradually move the system with respect to the lengthscales of the features of the energy landscape in configuration space.

### 2.3. Simulation of athermal quasi-static deformation

lowing a continuous path in the  $3N+1$  dimensional (configuration space +  $\gamma$ ) space, and the system simply follows it through the AQS protocol. As the energy landscape changes gradually, the system moves in the configuration space in a continuous way (that is, to small increments of  $\gamma$  correspond small changes in the configuration and in the potential energy).

2. At some point (like from (c) to (d) in Figure 2.7), increasing the strain can destroy the inherent structure the system is in, and thus the latter is not in a stable point of the energy landscape anymore. Taking a further AQS step brings the system into the basin of *another inherent structure* and the minimization procedure makes the system reach it. In this case, just one small increment in  $\gamma$  is sufficient to make the system reach its *spinodal limit* and jump to a far minimum in configuration space and make it lose abruptly a lot of its potential energy (this is somewhat similar to what happens to a rock brought in small steps on the top of a hill. It can happen that at some point a small step is sufficient to put the rock in an unstable position so that it rolls down the hill<sup>4</sup>). We will refer to this event as to a *transition*.

The AQS dynamics of a system initially residing in an inherent structure can be represented in terms of “configuration space -  $\gamma$ ” diagrams as that reported in Figure 2.4. With that viewpoint, the inherent structure acts as a “skeleton” over which the dynamics of an actual system takes place, as displayed in Figure 2.8.

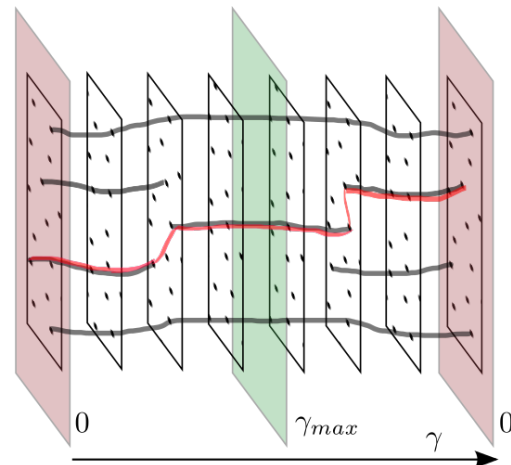


Figure 2.8: Representation of the trajectory (in red) of a system in the “configuration space -  $\gamma$ ” diagram of Figure 2.4 subjected to a deformation semicycle. The system resides in an inherent structure until such structure is destroyed under the effect of strain. At the values of the strain at which the destruction takes place, the system undergoes an abrupt transitions to other inherent structures.

---

<sup>4</sup>Don’t be misled by the metaphor though: here it’s the *landscape itself* that is altered by the change in strain!

It is possible to look at the athermal dynamics using the viewpoint of disconnectivity graphs also. In AQS dynamics, a system resides always on a leaf of a disconnectivity graph. As strain is changed, that leaf can shorten and disappear, as the inherent structure gets destroyed. Just before disappearing, the system resides on a leaf which is very close to an internal vertex of the system, which in turn has different leaves connected to it. At the transition, the leaf where the system is in disappears and the system falls into one of the leaves<sup>5</sup> connected to the internal vertex.

The way in which the system rearranges right after a transition depends on the region of the landscape where the system is in. Rearrangements involving a small number of particles are called in the literature “shear transformations”. Those involving a large number of particles that scales with the size of the system are called “avalanches” instead, and have been interpreted as sequences of shear transformations triggering other shear transformations [43, 69].

### 2.3.3 Oscillatory athermal deformation

Via the AQS protocol (or other procedures of simulation of deformation) one can change the strain (in steps) in an arbitrary way. The kind of deformation that is employed in this thesis is *oscillatory*:  $\gamma$  is incremented/decremented in steps of  $d\gamma$ , and has a triangle wave profile varying in the interval  $[-\gamma_{max}, \gamma_{max}]$  if plotted against the number of AQS steps (see Figure 2.9).

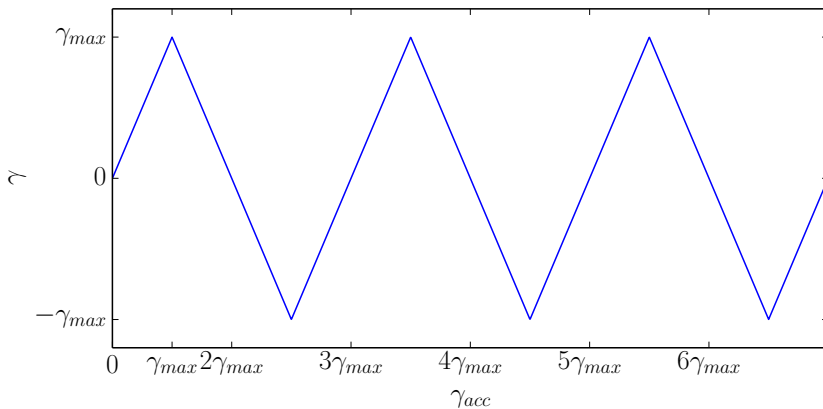


Figure 2.9: In the AQS oscillatory strain simulations performed in this thesis, the relationship between the strain  $\gamma$  and the *accumulated* strain  $\gamma_{acc}$  (i.e. the sum of the absolute incremental strains applied to the system, see Equation 2.5) has a triangle wave profile, oscillating in the interval  $[-\gamma_{max}, \gamma_{max}]$ .

A useful measure of the “total strain” applied to a system during an oscillatory defor-

---

<sup>5</sup>The number of possible leaves depends on the order of the saddle point associated to the internal vertex.

### 2.3. Simulation of athermal quasi-static deformation

mation experiment is the accumulated strain  $\gamma_{acc}$ , which can be written as

$$\gamma_{acc} = \sum_i |d\gamma| \quad (2.5)$$

where the  $d\gamma_i$ 's are the incremental strains applied to the system during the deformation, so that  $\gamma = \sum_i d\gamma$  (without taking the absolute value). Clearly  $\gamma_{acc}$  is a monotonic function of the number of steps.

From what has been said above, a cyclic deformation alters the initial undeformed landscape until the strain reaches the value  $\gamma_{max}$ . Then deformation is reversed and the landscape revisits the shapes assumed in correspondence of identical values of  $\gamma$ , until it finally gets back to its initial form as  $\gamma = 0$ . The same thing happens as  $\gamma$  is varied from 0 up to  $-\gamma_{max}$  and then again back to 0. It's illuminating to focus on the evolution of the inherent structures during such a cyclic modification of the landscape. This is illustrated in Figure 2.10. Starting from such a visualization of the evolution of inherent structures like that in Figure 2.10, in section 4.2 we build the TM model of the athermal dynamics of a deformed system.

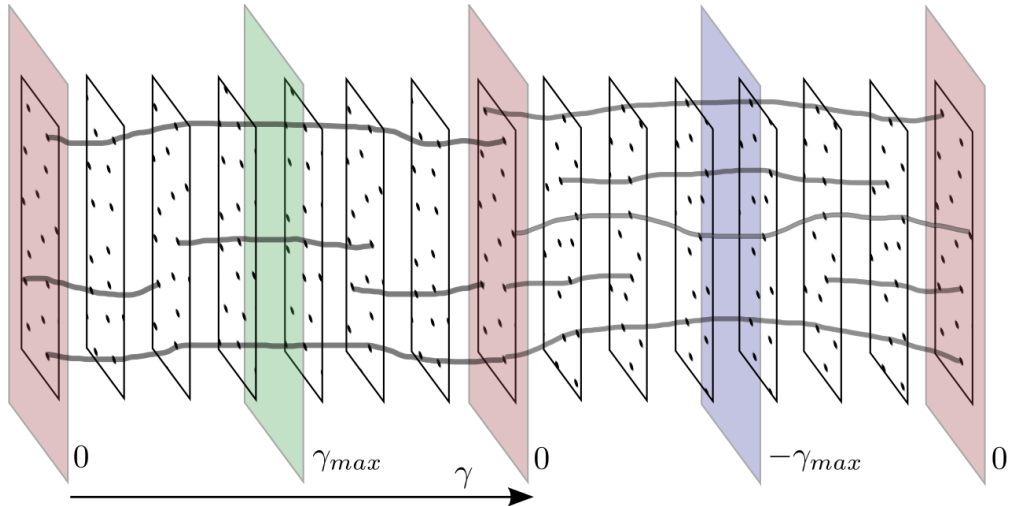


Figure 2.10: Diagram representing the evolution of inherent structures during a full deformation cycle. It is the juxtaposition of two diagrams like that of Figure 2.4. Note how the two halves of the diagram are symmetric with respect with the planes at  $\gamma = \gamma_{max}, -\gamma_{max}$ , but the overall diagram is *not* symmetric with respect to the  $\gamma = 0$  plane in the middle of the cycle.



# 3 Results from Lennard-Jones simulations

Here we report the outcome of computer simulations of deformation of Lennard-Jones systems, using the system and the techniques described in chapter 2. The general idea is simple: after samples are prepared, they are subjected to a series of oscillatory athermal deformation cycles. Our simulations thus extend those performed in [45], where samples were subjected to a single deformation semicycle. As a consequence of oscillatory deformation, particles in the system do rearrange, so that their positions and quantities as the average energy change as more and more oscillations are performed. In this chapter, we show that the way in which a system evolves depends crucially on the amplitude of oscillation  $\gamma_{max}$ , showing a phenomenology similar to that observed experimentally in dilute noncolloidal suspensions under oscillatory shear [55]. The main findings presented here have been published in [70].

## 3.1 Kob-Andersen Lennard-Jones mixtures (KA)

In the simulations presented in this chapter, we consider systems of particles interacting via the LJ potential in Equation 2.1, of sizes equal to  $N = 500, 4000, 32000$ . The composition and pair potential parameters  $\epsilon_{\alpha\beta}$  and  $\sigma_{\alpha\beta}$  are those of introduced by Kob and Andersen (KA) in [71] and are listed in Table 3.1. This system has been chosen because it's one of the most popular choices in the literature to study the dynamics of dense viscous liquids [27]. This in turn is due to the simplicity of the potential and the resistance to crystallization [59] that the model has.

The system is simulated using LAMMPS (Large-scale Atomic/Molecular Massively Parallel Simulator) [72]. The choice of LAMMPS as the code to run the LJ simulations has been made for several reasons: it is able to perform molecular dynamics in different ensembles (and more specifically at constant  $N, V, E$  and  $N, V, T$ ) and potential energy minimization using different minimization strategies; it is fast<sup>1</sup>, designed to run effi-

---

<sup>1</sup>One of the very early stages of this thesis work consisted in writing a Fortran code able to perform

$\alpha\beta$	$\epsilon_{\alpha\beta}$	$\sigma_{\alpha\beta}$
AA	1	1
AB	1.5	0.8
BB	0.5	0.88

Table 3.1: Values of the parameters of the Kob-Andersen (KA) binary Lennard-Jones mixture. Additional parameters are the overall number density  $\rho = 1.2$  and the relative concentrations  $c_A = 0.8$  and  $c_B = 1 - c_A = 0.2$ .

ciently in parallel on multiple CPUs to handle large systems. Its source code is open, freely available, thoroughly documented and supported by a large community. Incidentally, LAMMPS allows the same simulation scripts to be run on both CPU and GPU architectures with very little modifications.

A cut-off is used to truncate the interaction and thus speed up the molecular dynamics (as described in subsection 2.2.1), and this is chosen to be set at  $2.5\sigma_{\alpha\beta}$  for the different species. The potential is cut and shifted, as in [45], to make a direct comparison of the results easier. The modified form of the potential thus reads

$$\phi_{\alpha\beta}^{cut-shift}(r) = \begin{cases} 4\epsilon_{\alpha\beta} \left[ \left(\frac{\sigma_{\alpha\beta}}{r}\right)^{12} - \left(\frac{\sigma_{\alpha\beta}}{r}\right)^6 \right] + c_{\alpha\beta} & \text{if } r < 2.5\sigma_{\alpha\beta} \\ 0 & \text{if } r \geq 2.5\sigma_{\alpha\beta} \end{cases} \quad (3.1)$$

and  $c_{\alpha\beta}$  has the value such that  $\phi_{\alpha\beta}^{cut-shift}(2.5\sigma_{\alpha\beta}) = 0$ , and the pair potential is thus continuous at  $r = 2.5\sigma_{\alpha\beta}$ . From the energy landscape point of view, Equation 3.1 implies that the landscape is continuous, and has no abrupt “cliffs” or steps.

## 3.2 Preparation of the samples - equilibrium simulations

Before starting an AQS deformation, initial inherent configurations need to be generated. To do so, we create configurations equilibrated at some temperature  $T$  using the Nosé-Hoover thermostat and bring them to the inherent structure of the basin they belong to using the conjugate-gradient (CG) algorithm. In this thesis we use the implementation of the Polak-Ribière version of the CG algorithm<sup>2</sup> coded in LAMMPS [72]. To equilibrate configurations, particles are initially placed at random in a simulation box. The consequence of this is that some of their centers can be very close to each other, and in that case will strongly repel each other (the force originating from Equation 2.1 at small  $r$  is strongly repulsive). An energy minimization is thus applied to obtain a relaxed configu-

---

molecular dynamics for a single component LJ system in the canonical ensemble using the Nosé-Poincaré [73] integrator, using *cell lists* [61]. On the same tasks and running on a single CPU, LAMMPS was on average at least 5 times faster.

<sup>2</sup>A pedagogical introduction to the CG method is given in [74], whereas a useful comparison between different minimization strategies in order to find inherent structures is given in [75].

### 3.2. Preparation of the samples - equilibrium simulations

---

ration<sup>3</sup> characterized by less intense pair forces. Then, a set of velocities extracted from the Maxwell distribution at a given  $T$  is assigned to the particles, and the trajectories of the particles are integrated numerically using the Nosé-Hoover scheme implemented in LAMMPS. After an initial transient of duration  $\tau_t$ , the simulation is expected to start following an equilibrium trajectory so that the system visits configurations  $\mathbf{R}_i$  with a probability density proportional to the Boltzmann factor  $\exp(-\beta U(\mathbf{R}_i))$ . Only once that equilibrium has been reached configurations can be recorded and used to calculate thermodynamical averages appropriate to the temperature  $T$  [61]. It is thus important to have a reliable estimate of  $\tau_t$ , in order to discard from the analyses configurations sampled during the initial transient out of equilibrium. To do so, the potential energy  $U$  is fit to the form  $U(t) = (U(0) - U_{eq})e^{-t/\tau_t} + U_{eq}$ , and only configurations sampled for  $t < \tau_t$  are considered for further analysis. To have a more precise estimate of  $\tau_t$ , these configurations can be used to measure a *decorrelation time*  $\tau_r$  needed to the system to reach a state that has no relation with its initial one<sup>4</sup>. Our measure of correlation of choice is the self part of the intermediate scattering function<sup>5</sup> [77, 78]. Given a trajectory  $\mathbf{R}(t)$  such that particles are located at  $\mathbf{r}_1(t), \dots, \mathbf{r}_N(t)$ , the self intermediate scattering function is defined as

$$F_s(\mathbf{k}, t) = \frac{1}{N} \left\langle \sum_{i=1}^N \exp(-i\mathbf{k} \cdot (\mathbf{r}_i(t_0 + t) - \mathbf{r}_i(t_0))) \right\rangle \quad (3.2)$$

It follows from the definition that if the particles don't move from  $t_0$  to  $t_0 + t$ , then  $F_s = 1$ , because all the values in the exponential in Equation 3.2 are equal to zero. If particles move, the real part of  $F_s$  will have a lower value. One can calculate Equation 3.2 by summing over the positions of the  $A$  particles only, thus obtaining  $F_{sA}$ . We define  $\tau_r$  as the time needed to the real part of  $F_{sA}(k, t)$  to decay to 0.1, and we make the further assumption<sup>6</sup> that  $\tau_t = \tau_r$ . Incidentally, the value of  $\tau_r$  strongly depends on  $T$ . Intuitively, this is because at low temperatures the system moves slower in configuration space and is also more prone to be trapped in a valley of the potential energy landscape, with high potential energy barriers around it that prevent it from exploring the configuration space. More specifically, the binary KA is known to exhibit a dependence of  $\tau_r$  on  $T$ , as shown in Figure 3.1. This is a typical feature of glasses, that show a dramatic slowing down of their dynamics as the temperature is lowered below some  $T_g$ . This can be seen in more intuitive terms in Figure 3.2, where the mean squared displacement of our KA system is plotted as a function of temperature. Clearly, as temperature is lowered, the

---

<sup>3</sup>In principle, one could think of starting a simulation from an unrelaxed configuration and thermostating it at some  $T$  using the Nosé-Hoover thermostat or similar schemes, but this would not be very practical due to the large initial forces that generate from particle overlaps. Because of such forces, the simulation would need very small integration times not to lose numerical stability.

<sup>4</sup>This  $\tau_r$ , intuitively, is the time needed to the system to move in configuration space to a state which is as far (on average) as a state picked at random with a probability  $\exp(-\beta U(\mathbf{R}))$ .

<sup>5</sup>Another choice for  $\tau_t$  and  $\tau_r$  could have been the correlation time of  $U$  [7, 76].

<sup>6</sup>In other words, we assume that the time needed to reach equilibrium from the initial non-equilibrium state is comparable to that needed to the system to reach independent states once in equilibrium.

system takes more and more time to move away from its initial configuration at  $t = t_0$ .

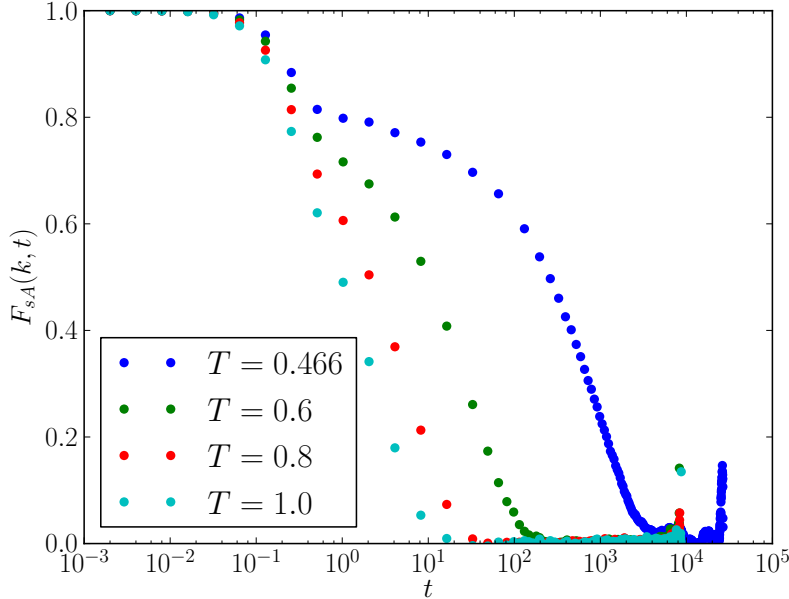


Figure 3.1: Self intermediate scattering function  $F_{sA}(k, t)$  as a function of time obtained from KA samples with  $N = 500$  and equilibrated at different temperatures, at  $k = 7.251$ . At high  $T$  the decay is exponential. At low  $T$  the decay is slower, and has a more complicated two-step decay form.

The increase of  $\tau_r$  at decreasing  $T$  poses a very practical problem: at low  $T$  it becomes increasingly difficult to study equilibrium states, because 1) the time  $\tau_t$  needed to attain equilibrium becomes very large (possibly way beyond timescales accessible by computer simulation) 2) even if equilibrium is reached, the time needed for the system to sample a reasonable number of states (so that one can measure their average properties) is also prohibitively large. Thus, at too low  $T$ , it becomes impossible to study systems in equilibrium. This is the computational analog of the glass transition observed experimentally as supercooled liquids are cooled below the glass transition temperature  $T_g$ .

As it was stated in chapter 1, temperature has clearly an effect on the regions of the landscape that are accessed by the sample. This is shown in Figure 3.3, where the average potential energy per particle of the inherent structures is plotted as a function of  $T$ . Our data are compatible with previous observations contained in [45] (see Figure 1.8).

In order to obtain samples differing in their features, we consider equilibrium samples at two different temperatures  $T = 0.466$  and  $T = 1.0$ , compute their trajectories via an NVE protocol, take samples separated by intervals of duration  $\tau_r$  in the NVE trajectory, neglect the velocities and minimize their energy via CG, so to obtain inherent structures

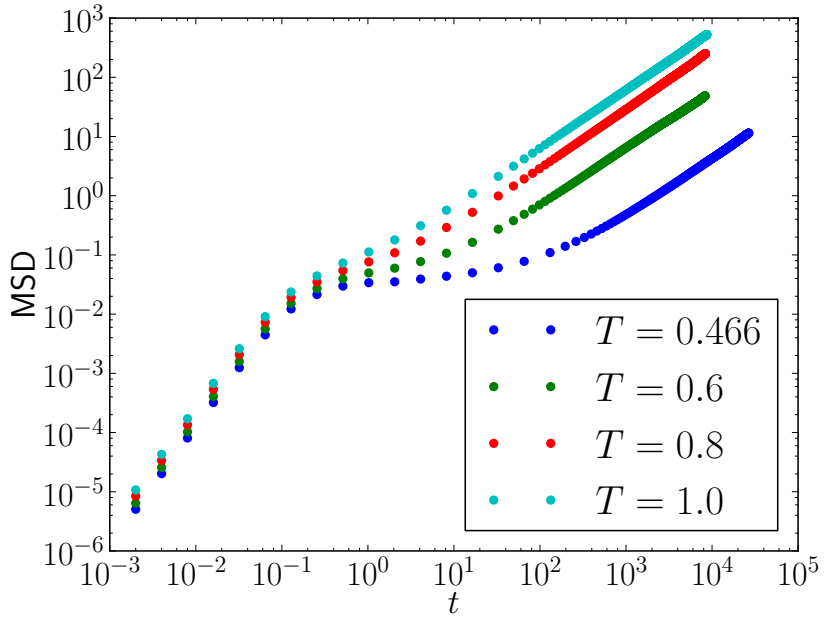


Figure 3.2: Mean squared displacement for the same systems described in Figure 3.1. For all  $T$  at short times the systems are ballistic, and the MSD has a quadratic dependence on time. At larger times the systems become all diffusive, as the MSD is linear in time. This happens only at large times for low  $T$ . At low  $T$ , particles spend a long time in the neighborhood of the  $t = 0$  configuration before they start diffusing away from it. For this reason, the diffusion constant is also much lower at lower  $T$ .

whose respective effective temperature is equal to  $T$ . The plot Figure 3.3 shows that these configurations do have significantly different average potential energies, and thus differ by their statistical properties. These will be the starting configurations of our AQS simulations described in the paragraph below.

### 3.3 Results of AQS shear deformation simulations

We take different samples of different sizes and effective temperature  $T$  and we subject them to AQS oscillatory deformation for different values of  $\gamma_{max}$ . The value of  $d\gamma$  must be carefully chosen, so that the modification of the landscape induced by a strain increment of  $d\gamma$  is weak enough so that all the dynamics is correctly sampled (see also discussion in section 2.3). This condition is assumed to be satisfied if  $d\gamma$  is much smaller than the typical strain interval between two consecutive transitions<sup>7</sup>. To verify that the choice of  $d\gamma$  is appropriate one can check that a choice of a smaller  $d\gamma$  does produce similar dynamics. In what follows we use  $d\gamma = 0.001, 0.0002, 0.00002$  for  $N = 500, 4000, 32000$

<sup>7</sup>In other words, the sampling resolution in the plot Figure 3.12 should be less than the separation between the values of the strain

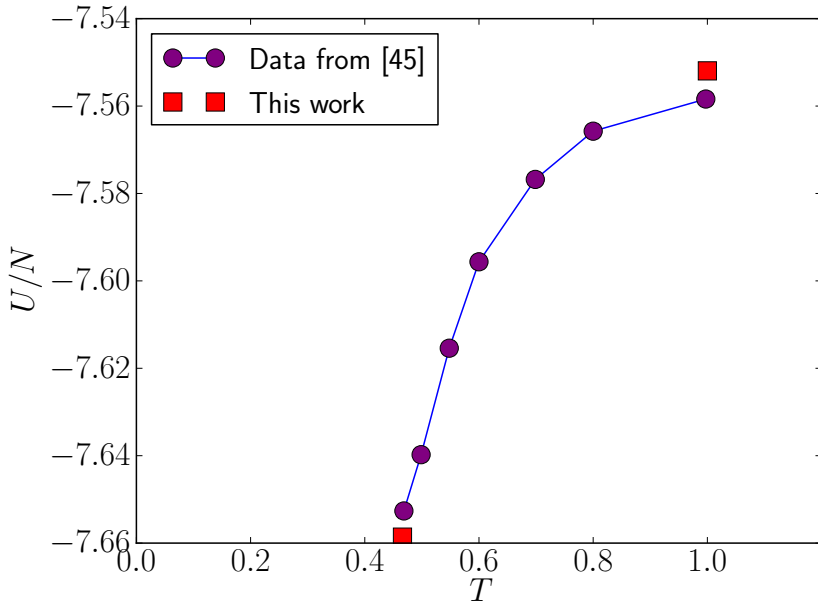


Figure 3.3: Average energy per particle for inherent configurations of the KA mixture at  $N = 500$  for different effective temperatures. Data taken from [45] has been extracted from Figure 1.8.

respectively. We monitor the potential energy  $U$  and the components of the stress tensor  $\sigma$  for every value of the accumulated strain  $\gamma_{acc}$  (see Equation 2.5) and record the positions of the particles at configurations such that  $\gamma = 0$ .

### 3.3.1 Energy of the structures: overaging and rejuvenation

By performing oscillatory deformation of KA samples at different effective  $T$  we extend what has been performed in [45], and apply a large number of cycles rather than just a semicycle<sup>8</sup>. In [45], by monitoring the potential energy behavior of the samples during the application of the deformation, it is noted that depending on the initial  $T$  and on the amplitude of deformation semicycle samples tend either to lower their potential energy  $U$ , reaching deeper inherent structures (they undergo *overaging*) or samples tend to reach higher  $U$ 's (they undergo *rejuvenation*). The data presented in [45], however, do not say more about whether a given choice of the amplitude  $\gamma_{max}$  and initial effective  $T$  leads to rejuvenation and some other leads to overaging. What we show in this thesis is that the results in [45] can be rationalized simply by increasing the number of oscillations cycles. In particular, we measure (in reduced LJ units) the potential energy per particle  $U/N$  of unstrained configurations ( $\gamma = 0$ ) for increasing  $\gamma_{acc}$ . By doing so, one gets the behavior plotted in Figure 3.4 (data are relative to the particular case  $N = 4000$

<sup>8</sup>Our protocol resembles that applied in [79] on crystallizing samples.

### 3.3. Results of AQS shear deformation simulations

---

and averaged over  $\approx 10$  samples): for large enough values of  $\gamma_{acc}$  (i.e. for very many oscillation cycles) after a transient  $U$  tends to approach a plateau value that depends on  $\gamma_{max}$ , is independent from the initial effective  $T$ , and increases with higher  $\gamma_{max}$ . For small values of  $\gamma_{max}$ ,  $U$  reaches a plateau also, but its asymptotic value depends on both  $\gamma_{max}$  and the initial effective  $T$ . These facts imply that:

1. For high  $\gamma_{max}$ , whether a sample at effective temperature  $T$  will undergo overaging or rejuvenation depends on whether the initial  $U(T)$  is higher or lower than the plateau value of  $U$  which is reached for large  $\gamma_{acc}$  by all samples deformed by cycles of amplitudes  $\gamma_{max}$ .
2. For high  $\gamma_{max}$ , and for high enough  $\gamma_{acc}$ , samples at different initial effective  $T$  lose memory of their initial state via oscillatory deformation, reaching states that cannot be distinguished (at least by looking at the energy  $U$ ).
3. For low  $\gamma_{max}$ , the value of  $U$  at high  $\gamma_{acc}$  depends on the initial  $T$ . In this case, one cannot make a general statement about whether rejuvenation or overaging will take a place. Still, generally speaking, small  $\gamma_{max}$  will tend to overage the samples, whereas large  $\gamma_{max}$  will tend to rejuvenate them, and samples with low effective  $T$  will tend more easily to rejuvenate than those with a higher effective  $T$ .
4. For low  $\gamma_{max}$ , samples retain memory of their initial  $T$ , even for high values of  $\gamma_{acc}$ .

Note that the results in [45] can be viewed as a transient of the curves plotted in Figure 3.4. In fact, as just a single semicycle is performed in [45], results in [45] correspond to our data at  $\gamma_{acc} = 2\gamma_{max}$ . Overaging or rejuvenation in [45] is thus the very beginning of the approach to a plateau value which is associated to  $\gamma_{max}$  only (for  $\gamma_{max}$  high enough) or to  $\gamma_{max}$  and  $T$  (for lower values of  $\gamma_{max}$ ).

#### **Relaxation behavior of the energy curves under deformation**

The potential energy trends as a function of  $\gamma_{acc}$  are curves approaching an asymptote for large values of  $\gamma_{acc}$ . We thus try to fit the  $U$  data using a stretched exponential model of the form

$$U(\gamma_{acc}) = (U(0) - U(\infty))e^{-(\gamma_{acc}/\tilde{\gamma}_{acc})^\alpha} + U(\infty) \quad (3.3)$$

The choice of such a model is justified by the fact that we're dealing with a decay behavior. The stretching exponent  $\alpha$  is introduced to approximately take into account the fact that by increasing  $\gamma_{acc}$  samples do travel in different regions of the landscape which change as  $\gamma_{acc}$  increased, each with a characteristic  $\tilde{\gamma}_{acc}$ . The fitting curves are superimposed to the data in Figure 3.4. Note how the curves reach a plateau faster for

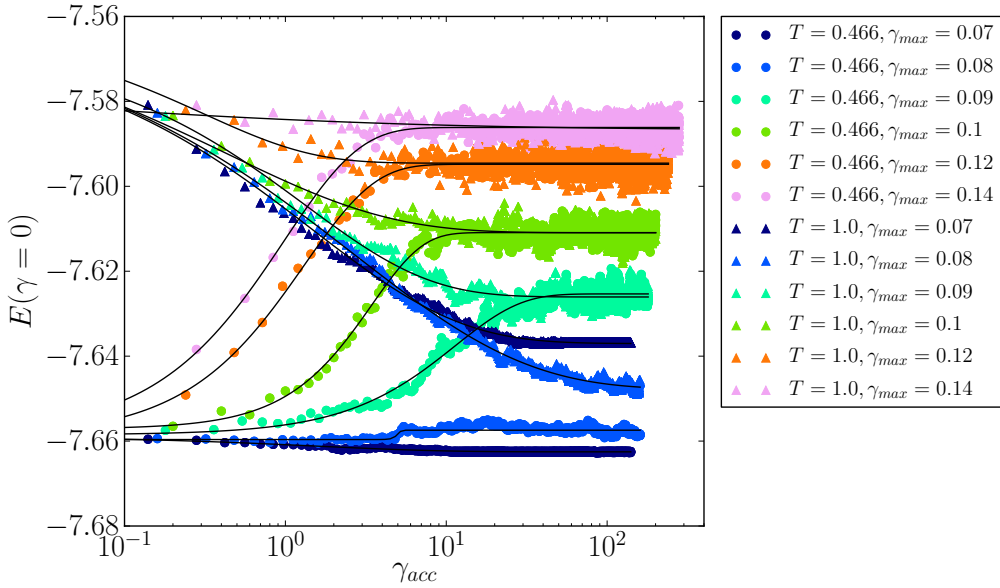


Figure 3.4: Potential energy per particle  $U/N$  as a function of  $\gamma_{acc}$ , for different initial effective temperatures and different deformation amplitudes  $\gamma_{max}$  and averaged over  $\approx 10$  sample realizations. The sizes of the considered systems is  $N = 4000$ , and the data refer to configurations with  $\gamma = 0$ . Fits using Equation 3.3. For low values of  $\gamma_{max}$ , the average energy assumes a fixed value beyond some characteristic  $\tilde{\gamma}_{acc}$ , which depends both on  $\gamma_{max}$  and on the initial effective temperature. For large values of  $\gamma_{max}$  the energy fluctuates around some value which depends on  $\gamma_{max}$  only. Approximatively, small  $\gamma_{max}$  correlate with overaging and large  $\gamma_{max}$  are associated with rejuvenation, as in [45].

higher values of  $\gamma_{max}$ , meaning that at larger oscillation amplitudes a lesser number of cycles is needed to make samples relax. This observation can be made more quantitative by plotting the values of  $\tilde{\gamma}_{acc}$  obtained from the fits in Equation 3.3 against the oscillation amplitude  $\gamma_{max}$ . This is done in Figure 3.5, where one can note that  $\tilde{\gamma}_{acc}$  is low for high and low values of  $\gamma_{max}$  and peaks at intermediate values of  $\gamma_{max}$ .

Fitting the data in Figure 3.5 would allow to draw a similarity with what is found in Figure 1.14 in the case of suspensions. However, the number of points we have is not large enough to quantitatively model and fit the data. Gathering data in the region of the peak requires to perform AQS simulations whose duration scales with  $\tilde{\gamma}_{acc}$ , and can thus become prohibitively long close to the region where  $\tilde{\gamma}_{acc}$  has a large value.

Two aspects of the energy behavior remain somewhat unexplained by the analysis of the energy data in Figure 3.4 and Figure 3.5. First, even though for both high and low values of  $\gamma_{max}$  samples evolve to energy plateaus for a large number of oscillation cycles, the nature of the plateaus seems to be very different in the two cases: a closer inspection of Figure 3.4 shows that for large values of  $\gamma_{max}$  the energy fluctuates around an average value of  $U$ , whereas for the lowest values of  $\gamma_{max}$  the potential energy reaches a *fixed*

### 3.3. Results of AQS shear deformation simulations

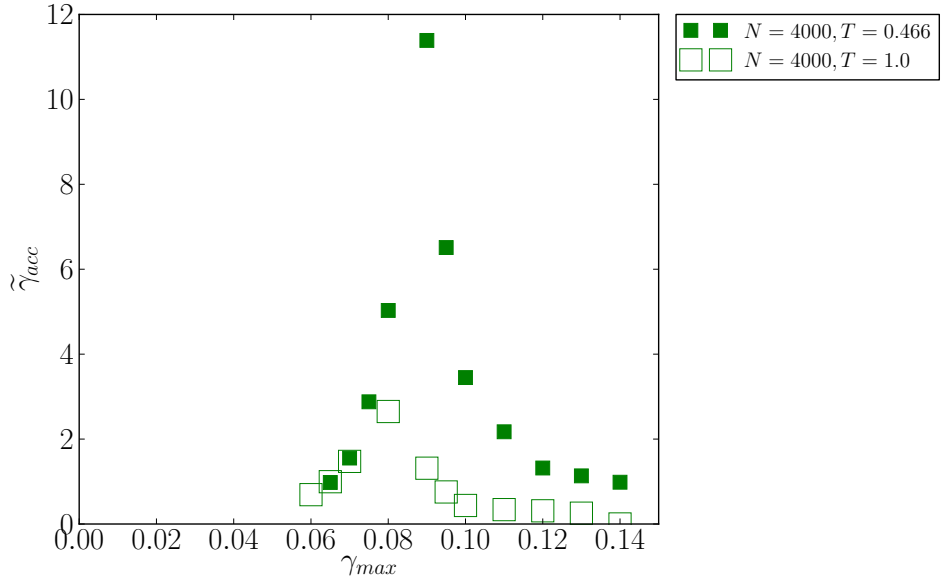


Figure 3.5: Plot of the characteristic accumulated strain  $\tilde{\gamma}_{acc}$ , extracted from the fits of  $U$  with the stretched exponential curves in Figure 3.4, for different values of  $\gamma_{max}$ . The two curves look different for different effective  $T$ , but do both show a marked increase for intermediate values of  $\gamma_{max}$  ( $\approx 0.08$ ).

value of  $U$ . Second, there is no indication of the mechanism that leads to the formation of a peak in the  $\tilde{\gamma}_{acc}$  plot for intermediate values of  $\gamma_{max}$ . These problems can be solved by looking at the motion that particles follow as a consequence of the external driving. We perform such analysis below, in subsection 3.3.3.

#### 3.3.2 Stress tensor behavior

The potential energy  $U$  is not the sole variable that is accessible through simulations. Another quantity we examined is the stress tensor  $\sigma$ , which was monitored at every AQS step.

The stress components are defined by the expression:

$$\sigma_{ij} = \frac{1}{V} \sum_k^N r_{k,i} \cdot f_{k,j} \quad (3.4)$$

where  $r_{k,i}$  is the  $i$  coordinate of the position vector of particle  $k$ , and  $f_{k,j}$  is the  $j$  component of the total force acting on particle  $k$ . As the system is athermal, there is no kinetic contribution to the stress tensor.

Rather than plotting each component of  $\sigma$  as a function of  $\gamma_{acc}$ , in Figure 3.6 we draw the scatter plots of the components of  $\sigma$  and the potential energy  $U$  for high values of  $\gamma_{max}$ . Data are relative to samples with  $N = 4000$  and with  $\gamma = 0$ , and are parametric

plots of  $\gamma_{acc}$ .

All the scatter plots in Figure 3.6 are parametric in  $\gamma_{acc}$ , so that each point in them represents a value of  $U$  and/or a component of  $\sigma$  at a different value of  $\gamma_{acc}$  (multiple of  $4\gamma_{max}$ ). Figure 3.6 contains a lot of information. One of these is that large oscillation amplitudes make all components of  $\sigma$  and  $U$  converge to a common value that depends on  $\gamma_{max}$ , regardless the initial effective  $T$  of the samples. This is clear from the fact data relative to two different initial temperatures  $T$  all fall into the same “blobs” in the steady state if they are associated to a common  $\gamma_{max}$ . As for the steady state, large  $\gamma_{max}$  oscillations do bring systems to configuration of higher  $U$  and residual  $\sigma_{xx}$ ,  $\sigma_{yy}$ ,  $\sigma_{zz}$  and  $\sigma_{xy}$  (the shear stress on the plane of deformation), whereas  $\sigma_{xz}$  and  $\sigma_{yz}$  seem unaffected by the deformation. The relationship between  $U$  and the diagonal components of the stress and  $\sigma_{xy}$  appears to be approximately linear (see first row of panels), but our data does not allow a very precise determination of the functional form [54].

### 3.3.3 Diffusion behavior

To quantify particle motion we first measure the mean squared displacement (MSD) of the sample from the initial configuration  $\mathbf{R}(0)$  for increasing values of  $\gamma_{acc}$ , for samples with  $N = 4000$  such that  $\gamma = 0$ :

$$\text{MSD}(\gamma_{acc}) = \frac{1}{N} \sum_i (\mathbf{r}_i(\gamma_{acc}) - \mathbf{r}_i(0))^2 \quad (3.5)$$

The result is plotted in Figure 3.7. Depending on  $\gamma_{max}$  the behavior of the MSD is strikingly different: for low values of  $\gamma_{max}$  the MSD saturates to a finite value, whereas for higher values it behaves linearly.

Such behavior is remarkable: samples below some value of  $\gamma_{max}$  at some point do stop their motion in configuration space, whereas if  $\gamma_{max}$  is high enough samples get farther and farther from the initial configuration. In the first case a system reaches a state that is a sort of “trap” which is stable under an oscillation of amplitude  $\gamma_{max}$ . The nature of such traps (named “absorbing” states) is explored in more detail in chapter 5. The observation of such transition in the dynamics resolves one of the issues raised during the observation of the potential energy trends: oscillations at low values of  $\gamma_{max}$  reach a fixed value of  $U$  just because samples do cease to travel in configuration space.

In order to interpret the data in Figure 3.7 one can assume that systems diffuse in configuration space like random walkers in 3ND as a consequence of deformation. Their diffusion constant is  $D$ , and can they stop permanently their motion with a probability  $\lambda$  per unit  $\gamma_{acc}$ . The details of such a “mortal random walk” model (recently explored also in [80]) are given in Appendix B. Within such a model the MSD can be expressed

### 3.3. Results of AQS shear deformation simulations

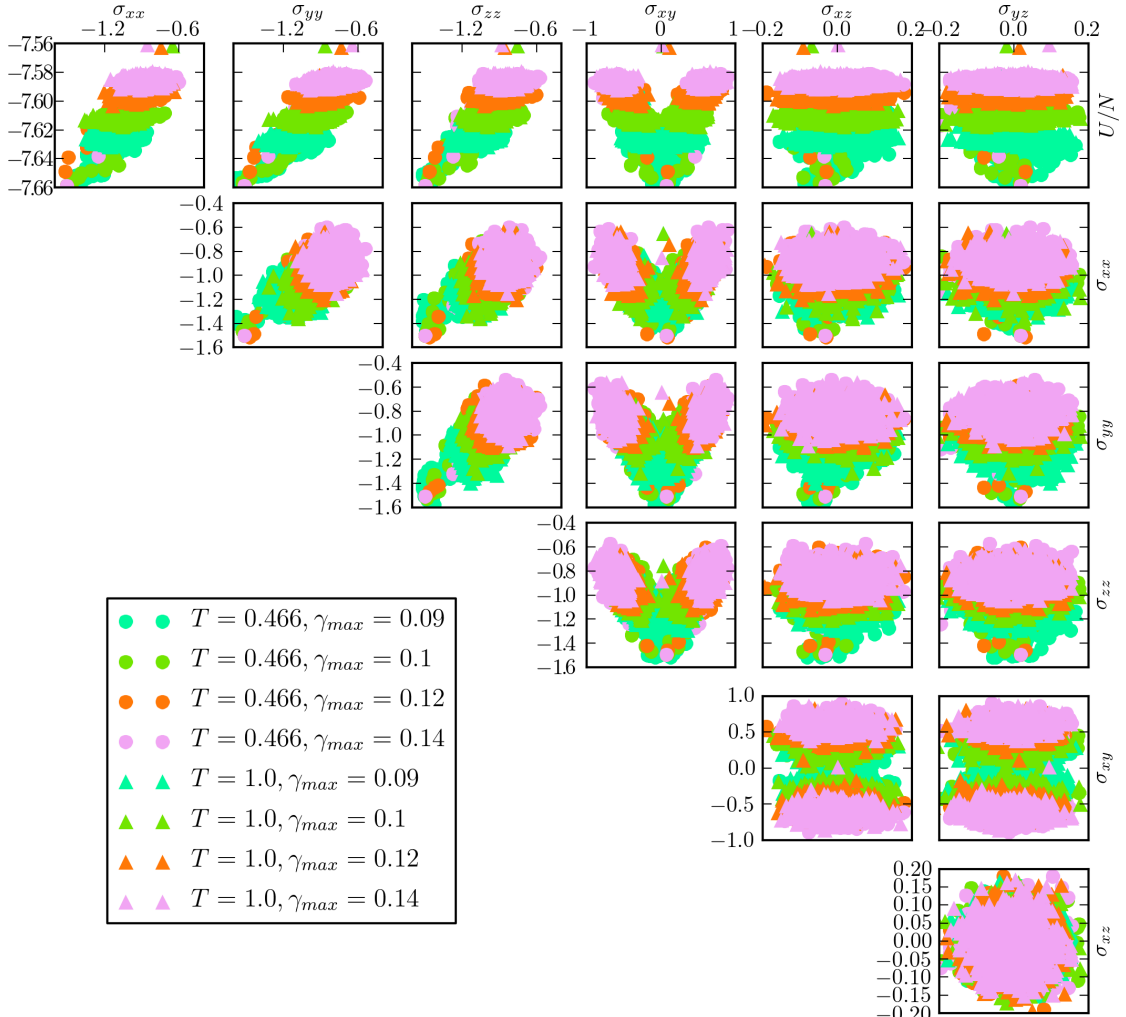


Figure 3.6: Matrix of scatter plots of  $\sigma_{ij}$  and  $U$ , which both depend parametrically on  $\gamma_{acc}$ , for different (and large) values of  $\gamma_{max}$  and initial effective temperatures  $T$ , in samples with  $N = 4000$ . Data are all relative to  $\gamma = 0$ , so that the stress components are all *residual* stress components. The “blobs” correspond to points obtained where the majority of data fall, which is the steady state. Outliers refer to points collected at the very beginning of the deformation oscillations. The ensemble of plots indicates that samples with different effective temperatures do assume the same values of  $U$  and  $\sigma_{ij}$  in the steady state if they are sheared with the same amplitude  $\gamma_{max}$  (as triangle and circles of the same color overlap in the blobs). From the first row of scatter plots, it’s clear that an increase of  $\gamma_{max}$  corresponds to a higher potential energy  $U$ , increasing values of the diagonal values of the stress  $\sigma_{ii}$  and an increasing shear stress in the plane of deformation  $\sigma_{xy}$ . In particular, the residual stress  $\sigma_{xy}$  is also seen oscillating between negative and positive values (whose absolute value increases as  $\gamma_{max}$  is increased), depending on the direction of the deformation. The dependence of  $U$  from  $\sigma_{ii}$  and  $\sigma_{xy}$  seems approximately linear. From the plot of  $\sigma_{xz}$  against  $\sigma_{yz}$  one sees that these components of the stress tensor are basically unaffected by the deformation.

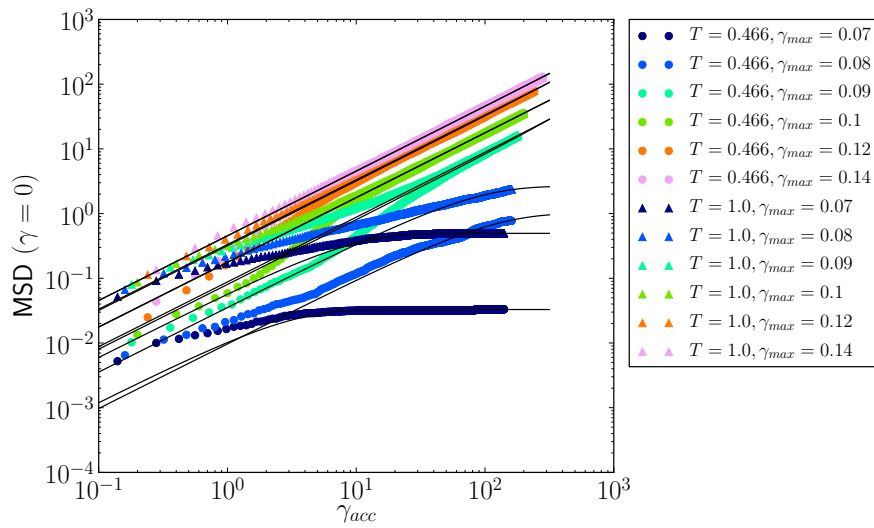


Figure 3.7: Mean squared displacement as a function of  $\gamma_{acc}$ , for different initial effective temperatures and different deformation amplitudes  $\gamma_{max}$ , measured from the initial undeformed configuration and averaged over several samples with  $N = 4000$  particles. For low  $\gamma_{max}$ , after a transient the systems do stop moving, and the respective MSD reaches a plateau. For larger values of  $\gamma_{max}$ , the systems are diffusive. This behavior can be described with the mortal random walk model in Equation 3.6 (black curves), but the fits are not completely satisfying.

as

$$\text{MSD}(\gamma_{acc}) = \frac{D}{\lambda N} (1 - e^{-\lambda \gamma_{acc}}) \quad (3.6)$$

where  $D$  is  $\gamma_{max}$  dependent. In fact, it's reasonable to assume that higher values of  $\gamma_{max}$  will make the sample undergo longer leaps in configuration space<sup>9</sup>. The parameter  $\lambda$  is also expected to be dependent on  $\gamma_{max}$ , as for higher oscillation amplitudes fewer points of configuration space will be able to act as "traps". As the density of such states in configuration space is lower, so will be the likelihood to encounter them. Fits obtained using the expression in Equation 3.6 varying  $D$  and  $\lambda$  are plotted for different data series in Figure 3.7. The quality of the fits is not excellent, possibly because the dynamics of the system depends on the features of the landscape explored by the system. These change as  $\gamma_{acc}$  is increased: this can be seen, for instance, in Figure 3.4, where the average  $U$  of the configurations explored by the system depends on  $\gamma_{acc}$  until a plateau is reached. If  $U$  changes with  $\gamma_{acc}$ , so will the landscape. It is thus reasonable to assume that  $D$  and  $\lambda$  will change as well as  $\gamma_{acc}$  increases. In other words, the partial failure of the mortal random walk model can be attributed to the initial transient that the system experiences at low number of oscillation cycles.

<sup>9</sup>This is because the larger the oscillation amplitudes, the larger are the probabilities for the system to "get lost" in configuration space and find itself displaced from the initial configuration after a full oscillation cycle.

### 3.3. Results of AQS shear deformation simulations

An alternative approach to describe particle motion is to exclude from the analysis the transient altogether, and study the MSD of the system starting from a reference configuration at a value of  $\gamma_{acc}$  such that a “steady” state has already been attained. For instance one can measure the MSD starting from the state visited at  $\tilde{\gamma}_{acc}$ , as determined from the fits of the energy trends of the kinds shown in Figure 3.4:

$$\text{MSD}(\gamma_{acc} - \tilde{\gamma}_{acc}) = \frac{1}{N} \sum_i (\mathbf{r}_i(\gamma_{acc}) - \mathbf{r}_i(\tilde{\gamma}_{acc}))^2 \quad (3.7)$$

Plots of the MSD obtained this way are shown in Figure 3.8 and are much easier to interpret: for low  $\gamma_{max}$  systems simply do not move, so their  $\text{MSD}(\gamma_{acc} - \tilde{\gamma}_{acc})$  is close to zero, whereas for higher  $\gamma_{max}$  the MSD increases linearly, with no samples seeming to reach absorbing states within our range of  $\gamma_{acc}$ . One can thus simply write:

$$\text{MSD}(\gamma_{acc} - \tilde{\gamma}_{acc}) = D(\gamma_{acc} - \tilde{\gamma}_{acc}) \quad (3.8)$$

Linear fits are superimposed to the data in Figure 3.8.

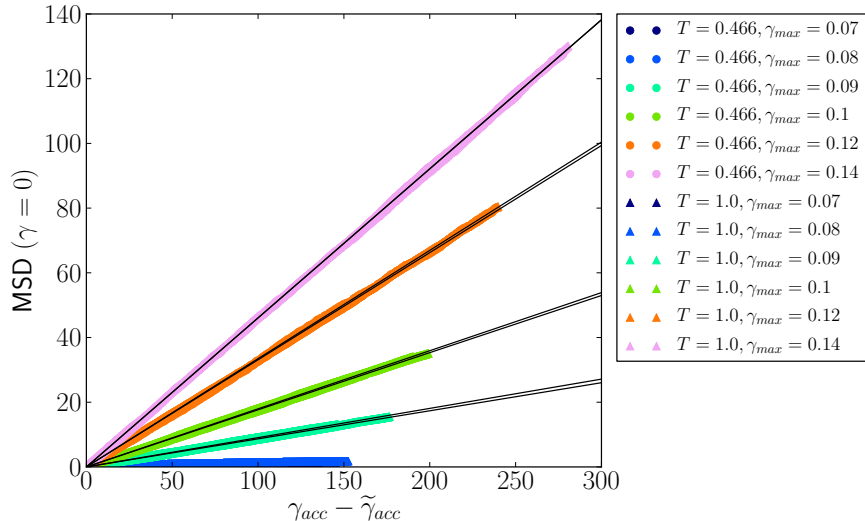


Figure 3.8: Mean squared displacement as a function of  $\gamma_{acc} - \tilde{\gamma}_{acc}$ , for different initial effective temperatures and different deformation amplitudes  $\gamma_{max}$ , measured from configurations such that  $\gamma = 0$  and  $\gamma_{acc} > \tilde{\gamma}_{acc}$ . For low  $\gamma_{max}$ , the systems don’t move, and their respective MSD is 0. For larger values of  $\gamma_{max}$  instead the systems are diffusive. This allows to fit the data with the model in Equation 3.8 (black curves). The diffusion constant depends on  $\gamma_{max}$  only, and not on the effective  $T$  of the samples.

Data series obtained from samples at different effective  $T$  do overlap, showing that after the transient systems reach states having an equivalent behavior in terms of particle motion.

The linear fits of  $\text{MSD}(\gamma_{acc} - \tilde{\gamma}_{acc})$  allow to study the way  $D$  depends on  $\gamma_{max}$ , and from Figure 3.9 one can see how particle motion under oscillatory strain depends crucially on

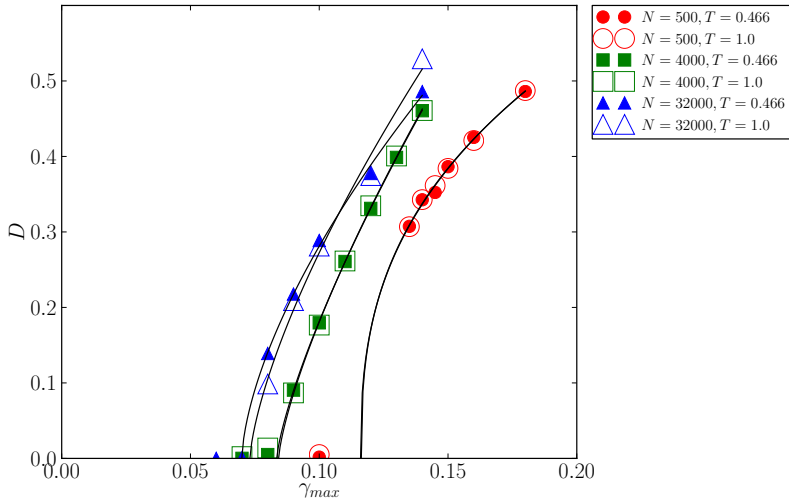


Figure 3.9: Diffusion constant of the model Equation 3.8 determined from fits as those in Figure 3.8 as a function of  $\gamma_{max}$ , for different system sizes.  $D$  seems in all cases to become non-zero at a value  $\gamma_c$ , which depends on the system size. Data can be described approximately with a power law (Equation 3.9, black curves).

the oscillation amplitude for the class of systems under consideration. This is one of the main results of this thesis and the main result in [70]. For low  $\gamma_{max}$   $D$  is zero and at some value of the amplitude (which we will refer to as “critical”  $\gamma_c$ ), systems increase their MSD in Equation 3.8 linearly. The values of  $D$  can be fitted by a power law of the form

$$D = A(\gamma_{max} - \gamma_c)^\beta. \quad (3.9)$$

The values of  $\gamma_c$  as determined via the fits are dependent on the sizes of the systems, with  $\gamma_c$  decreasing for increasing  $N$ . This raises the doubt that  $\gamma_c$  could be an artifact of our simulations and thus vanish in the limit  $N \rightarrow \infty$ . To check if this is the case we plot in Figure 3.10 the values of  $\gamma_c$  against the inverse system size. An analysis of Figure 3.10 seems to exclude this scenario, even though our data points are too few to completely rule out the possibility of a sharp turn in the  $\gamma_c$  dependence at low  $1/N$  such that  $\gamma_c \rightarrow 0$  for large  $N$ .

The values of  $\beta$  in Equation 3.9 obtained from the fits in Figure 3.9 are reported in Table 3.2. Such values seem not to be compatible with the exponent  $\beta = 0.84$  which pertains to conserved directed percolation in 3D [56], so our model does not seem to fit in this non-equilibrium universality class [57]. However, more precise estimates of  $\beta$  (through better statistics on the data in Figure 3.9 and a precise estimate of size effects) would be needed to conclusively confirm this.

### 3.3. Results of AQS shear deformation simulations

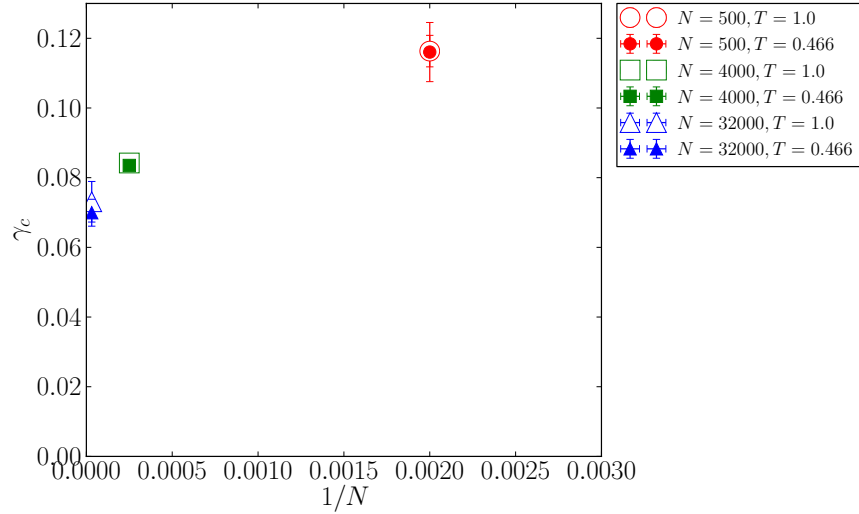


Figure 3.10: Values of  $\gamma_c$  determined from the fits in Figure 3.9 as a function of the inverse system size.  $\gamma_c$  is lower at larger  $N$ , but our data tend to suggest that  $\gamma_c$  will be non-zero in the limit  $N \rightarrow \infty$ .

$N$	$\beta$
500	$0.37 \pm 0.11$
4000	$0.74 \pm 0.08$
32000	$0.69 \pm 0.11$

Table 3.2: Average values of the exponents  $\beta$  obtained from the fits of the data in Figure 3.9 as a function of the size of the systems.

For the system sizes studied,  $\gamma_c$  seems to have a crucial role and separates two regimes, so that the data in Figure 3.7, 3.8, 3.10 and especially the peak of  $\tilde{\gamma}_{acc}$  in Figure 3.5 can be interpreted in the following way:

- For  $\gamma_{max} \ll \gamma_c$ : Due to the low value of  $\gamma_{max}$ , the undeformed ( $\gamma_{acc} = 0$ ) system initially travels slowly in configuration space, but soon reaches an absorbing state. This is because there's a large number of states in configuration space that can act as traps for the system if it falls in one of them. For these reasons, the value of  $\tilde{\gamma}_{acc}$  extracted from the fits of the potential energy is low and the MSD (computed with the expression in Equation 3.5 and plotted in Figure 3.7) saturates at correspondingly low values of  $\gamma_{acc}$ .
- For  $\gamma_{max} < \gamma_c$ : A higher amplitude means a faster exploration of configuration space, but the number of states that are absorbing is severely reduced as  $\gamma_{max}$  approaches  $\gamma_c$ , so that  $\tilde{\gamma}_{acc}$  becomes increasingly high, and the MSD takes a correspondingly large value of  $\gamma_{acc}$  to saturate.
- For  $\gamma_{max} > \gamma_c$ : Virtually no absorbing states exist above  $\gamma_c$  so that the MSD can't

saturate. The exploration of configuration space is still not very fast, so that the transient in the energy  $U$  lasts long ( $\tilde{\gamma}_{acc}$  high). The MSD is linear when calculated with both Equation 3.5 and Equation 3.7.

- For  $\gamma_{max} \gg \gamma_c$ : No absorbing states exist above  $\gamma_c$ , and the exploration of configuration space is fast. The value of  $\tilde{\gamma}_{acc}$  is thus low, and the MSD is linear with a steep slope.

### Nature of the absorbing and “diffusive” states, “shear banding”

The MSD computed with Equation 3.5 and Equation 3.7 gives an average isotropic measure of particle motion of deformed systems. But it does not say, for instance, if particles do move preferentially in some direction rather than others, or if some particles move more than others when samples are subjected to oscillatory deformation.

Inspection of the displacement of the particles does show that the distribution of particles that move the most can be spatially inhomogeneous. In Figure 3.11 we plot configurations of particles at  $\gamma = 0$  which have reached the steady state for oscillatory deformation of  $\gamma_{max} > 0.1$ , highlighting in red particles that move more than 0.8 (in reduced units) when they are subjected to a single additional deformation cycle. In samples with  $N = 32000$  particles that move the most are clearly localized in a band which is parallel to the  $xz$  plane and whose thickness is approximately half of the simulation box. In addition, such band doesn’t change in thickness and position if it is recomputed after having applied several cycles to the sample, and its thickness is weakly dependent on  $\gamma_{max}$ . Smaller samples do not show this kind of phenomenon (see for instance the  $N = 4000$  samples in Figure 3.11a and Figure 3.11c). In smaller samples the particles that move the most do correlate in space, but without giving rise to band-like structures. We thus surmise that bands observed in our largest samples could be observed in even larger samples, possibly showing the same thickness. Bands wouldn’t occur in our smaller samples simply because these are smaller than the characteristic thickness of such bands. It would be interesting to check whether such bands exist in larger samples, and if *multiple* bands can arise and interact. However, such investigation has proved to be beyond the computational power at our disposal (samples with  $N > 100000$  would have required running times exceeding a month on our 48 CPU cluster nodes).

#### 3.3.4 Energy dissipation

When LJ samples are deformed by means of AQS deformation, they change their energy as a consequence of the deformation of the landscape. Most of the time energy changes are continuous, but sometimes abrupt changes due to collisions with saddle points in the energy landscape occur (see discussion in subsection 2.3.2 and [66]). In particular, if one looks at the potential energy  $U$  as a function of  $\gamma$  during cyclic deformation of an inherent structure (Figure 3.12), the behavior for small amplitudes is to a first

### 3.3. Results of AQS shear deformation simulations

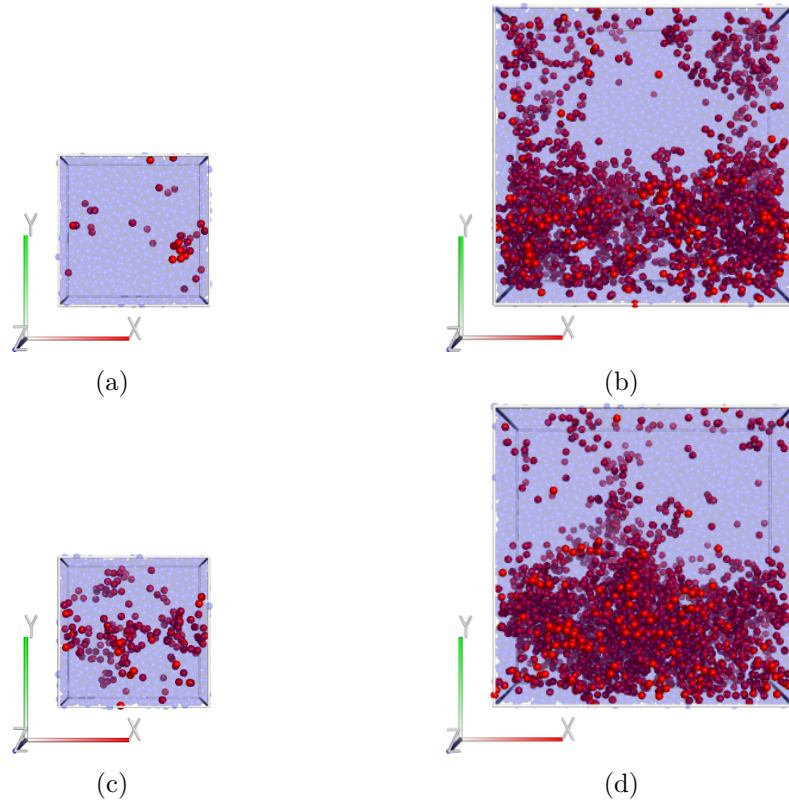


Figure 3.11: Typical samples with  $N = 4000, 32000$  in the steady state for oscillatory deformations of  $\gamma_{max} = 0.1$  ((a) and (b)) and  $0.12$  ((c) and (d)). Particles which move more than 0.8 (in reduced units) if the samples are subjected to an additional cycle are highlighted in red. Clearly such particles are organized in bands in the largest samples, whereas no such spatial heterogeneity is visible in the smaller samples.

approximation elastic, with the potential energy depending quadratically from the strain  $\gamma$ . In fact, incrementing the strain of an initially undeformed sample has usually the effect of increasing smoothly its potential energy, so that energy is pumped into the system if the strain is increased by some amount  $d\gamma$ . If the sample is sheared back, it goes back spontaneously to the configuration assumed before deformation, so that no additional energy is required to bring the system to the initial state. However, this is not always the case: by looking closely at the  $U$  vs  $\gamma$  curves in Figure 3.12 one can see small discontinuities in  $U$ , due to the collisions with saddle points mentioned above. In correspondence of these, if the system is deformed it loses stability and rearranges by losing energy before finding a new stable configuration. If sheared back, it doesn't assume the configuration it had prior to the deformation, but a state with a lower energy. Additional energy is thus required to restore the original state, and some energy is thus *dissipated* in the process.

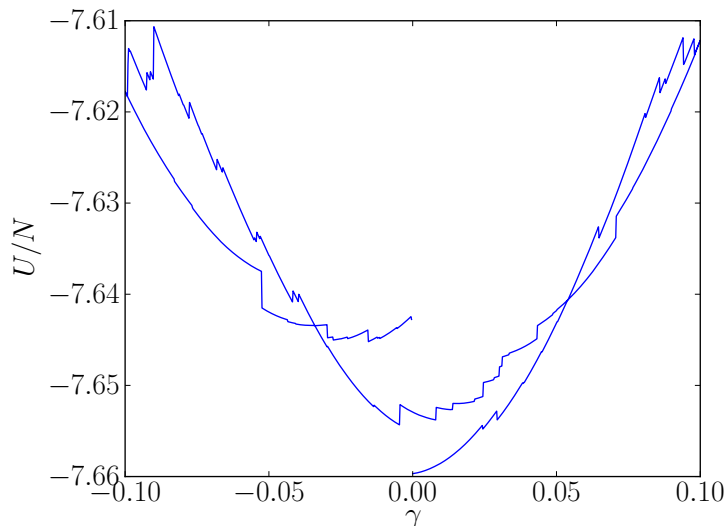


Figure 3.12: Energy per particle as a function of the strain  $\gamma$  for a sample of  $N = 4000$  starting from an undeformed sample. The curve shows a large number of discontinuities, each of which corresponds to a transition due to a collision with a saddle point of the energy landscape in the course of deformation. After the full cycle the system has not the same potential energy it had before the cycle, because the deformation has modified its structure.

Rearrangements and dissipation appear more frequent as  $\gamma_{max}$  is increased (this is because the system can't store arbitrarily large amounts of potential energy elastically, and rearrangements are the mechanism to release it). To quantify dissipation as a function of  $\gamma_{max}$ , one could simply measure the  $U$  drops that occur during a cycle. An alternative, more intuitive way to do this, is to look at the behavior of the stress tensor component in the same plane of the deformation  $\sigma_{xy}$  (see Equation 3.4) as a function of  $\gamma$ . The

### 3.3. Results of AQS shear deformation simulations

area inside the curve  $\sigma_{xy}(\gamma)$  correlates<sup>10</sup> with the work done on the system during deformation. For small values of  $\gamma$ ,  $\sigma_{xy}$  is linear in  $\gamma$ , and deviates from linearity at higher  $\gamma$ . The linearity of  $\sigma_{xy}$  is required to make work linear in  $\gamma$  and thus  $U$  quadratic in  $\gamma$ . When  $U$  undergoes energy drops as a consequence of rearrangements, its derivative often also has a drop, leaving a mark in  $\sigma_{xy}$ , which is thus sublinear Figure 3.13.

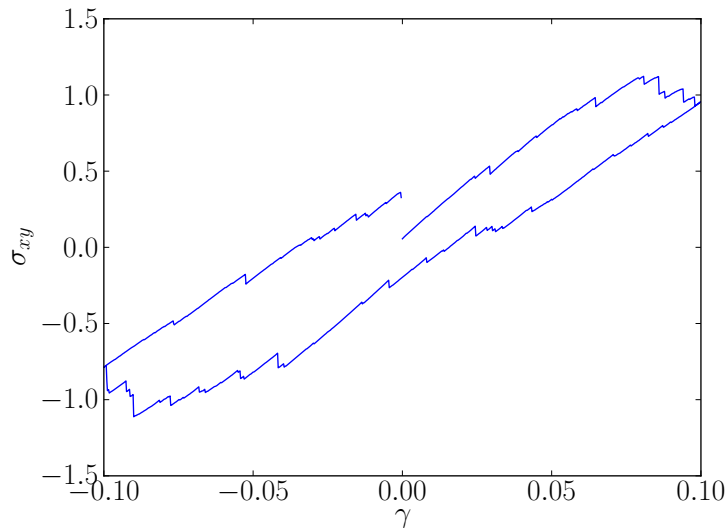


Figure 3.13: As in Figure 3.12, but plotting the stress component on the plane of the deformation rather than the energy. Again, the stress drops reflect transitions, and the fact that the stress values at the beginning and at the end of the cycle are different indicates that the sample has been modified by the deformation.

The area of the  $\sigma_{xy}(\gamma)$  curve in a full cycle is thus related to the work done by the system to complete a full cycle. In the steady state mentioned in subsection 3.3.1 and subsection 3.3.3, after a full cycle the samples return to states which are *statistically* similar to the initial one (for instance,  $U$  is on average unchanged, by definition of steady state). This means that the work done on the system is a good measure of the dissipated energy. In order to measure it, we plot in Figure 3.14 the  $\sigma_{xy}$  hysteresis curves for different values of  $\gamma_{max}$ , averaged on several cycles. Hysteresis curves are very narrow and almost linear for small  $\gamma_{max}$ , where only few particle rearrangements and dissipation occur. For larger  $\gamma_{max}$ , curves widen, showing a much higher amount of dissipation per cycle.

It is meaningful to plot the values of the areas of the hysteresis curves in Figure 3.14 as a function of  $\gamma_{max}$ . This is done in Figure 3.15, where the values are seen to increase dramatically after some threshold value of  $\gamma_{max}$  which appears compatible with the  $\gamma_c$  extracted from the fits of particle diffusion in subsection 3.3.3. In other words, the onset

<sup>10</sup>The area inside the  $\sigma_{xy}$  curve is not *all the work* performed on the system, because other work is performed related to variation of the other stress components.

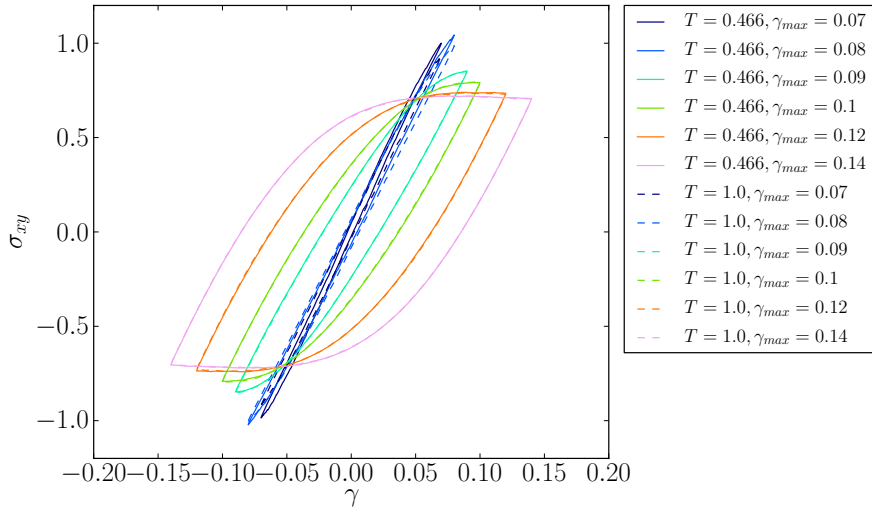


Figure 3.14: Average stress in the plane of deformation as a function of shear strain, averaged on deformation cycles such that  $\gamma_{acc} > \tilde{\gamma}_{acc}$  on systems with  $N = 4000$ . The systems show wide hysteresis for high  $\gamma_{max}$ , whereas at smaller  $\gamma_{max}$  the curve almost retraces itself when strain is reversed. This indicated that dissipation is much higher at larger values of  $\gamma_{max}$ .

of particle diffusion at  $\gamma_c$  marks also the start of energy dissipation.

The exact dependence of the areas of the hysteresis curves as a function of  $\gamma_{max}$  is not known to us. This stems from the fact that we didn't build a model for the dependence of  $\sigma_{xy}$  as a function of the shear strain  $\gamma$ . However, for large values of  $\gamma_{max}$  the hysteresis curve becomes just "longer" on the strain axis of the stress-strain curve, and thus its area is expected to be linear in  $\gamma_{max}$ .

### 3.3.5 Is $\gamma_c$ equal to the yield strain?

We've seen above that one can identify an amplitude  $\gamma_c$  which is convincingly related to a slowdown in the relaxation of  $U$  as a function of  $\gamma_{acc}$  (subsection 3.3.1), the onset of particle diffusion (subsection 3.3.3) and that of dissipation (subsection 3.3.4). Can the value of  $\gamma_c$  be related to other relevant strain values? One possible candidate is the *yield strain*  $\gamma_y$ , which we define here as the maximum of the stress-strain curve. To calculate  $\gamma_y$  from our simulations, we take inherent structures at effective  $T = 0.466$  and subject them to shear deformation up to some large value of the strain. As seen above, the stress-strain curve is initially linear, but eventually saturates to a plateau value. Depending on the effective  $T$  curves can peak in correspondence of some value that we identify as  $\gamma_y$  (see Figure 3.16). Such value can be determined with precision by fitting a quadratic curve on the peak of the stress curve.

How does  $\gamma_y$  compare to the values of  $\gamma_c$  measured from systems with the same size and initial effective temperature? As it can be seen from Figure 3.17 the values do not seem

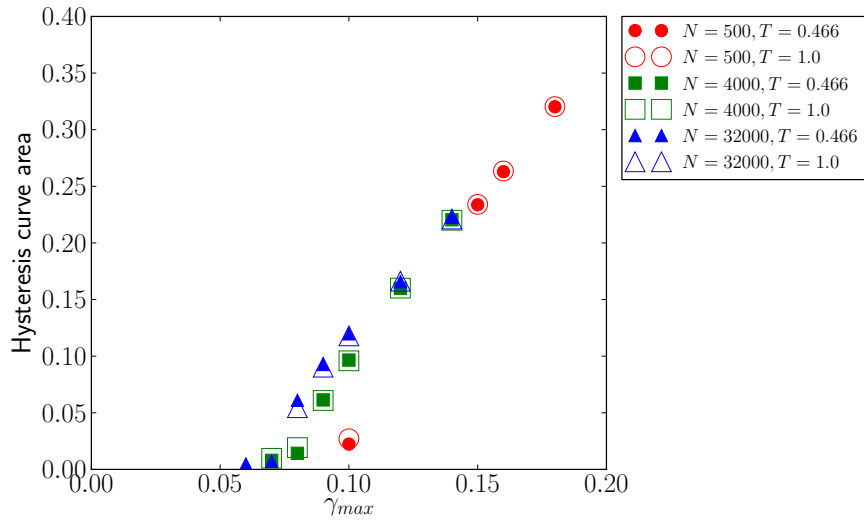


Figure 3.15: Areas of hysteresis curves like those in Figure 3.14 as a function of  $\gamma_{max}$  for different system sizes. It's evident how dissipation sets in at a some value  $\gamma_{max}$  that depends on the system size. Incidentally, this value is compatible with the values of  $\gamma_c$  obtained from the analysis of the diffusion for the respective system size. As expected, for large values of  $\gamma_{max}$  the hysteresis area approaches a linear behavior.

to match. At first sight, this could sound somewhat surprising:  $\gamma_c$  is related to the onset of dissipation in the samples, which will set in as samples leave the elastic regime and exhibit a peak in the stress at  $\gamma_y$ . Strictly speaking, however,  $\gamma_y$  is a property of initially *undeformed* structures, because it is measured starting from samples that haven't experienced any prior deformation;  $\gamma_c$ , instead, is a property of oscillatory deformed samples that have undergone deformation and have consequently reached a “steady” state. Thus, there is no reason for  $\gamma_c$  to coincide with  $\gamma_y$ , as they are associated to quite different objects. In addition, we don't expect the discrepancy between  $\gamma_c$  and  $\gamma_y$  to be influenced by our choice of definition of  $\gamma_y$ . In fact, as stress-strain curves in Figure 3.16 relative to different  $N$  do almost overlap, any definition of  $\gamma_y$  will give values of  $\gamma_y$  that depend on  $N$  very weakly, whereas  $\gamma_c$  is significantly influenced by system size.

## 3.4 Summary

We have performed simulations of oscillatory athermal shear deformation of dense binary mixtures of Lennard-Jones particles.

Our main finding is the existence of a “critical” shear deformation amplitude  $\gamma_c$  which has a crucial role in the dynamics of our system under deformation.

Below  $\gamma_c$ , particle motion comes to a stop after a finite number of cycles, with samples reaching absorbing states that are invariant under the application of additional deformation cycles and are correlated with the starting configurations prior to deformation.

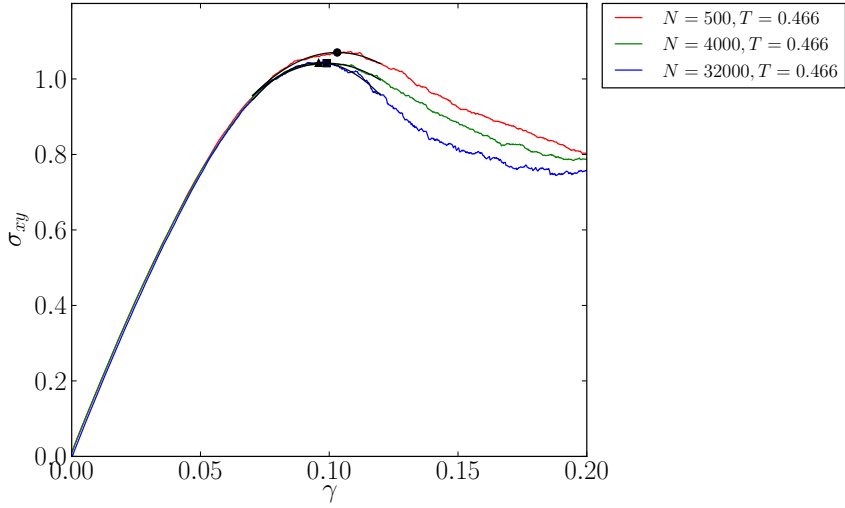


Figure 3.16: Stress in the plane of deformation plotted as a function of strain starting from undeformed samples with  $N = 4000$ . Stress at low  $\gamma$  is linear, and then it peaks in correspondence of a value of the strain  $\gamma_y$ . The value of  $\gamma_y$  is calculated by fitting the peak of the curve with a quadratic function. The value of  $\gamma_y$  has a weak dependence on the size of the system.

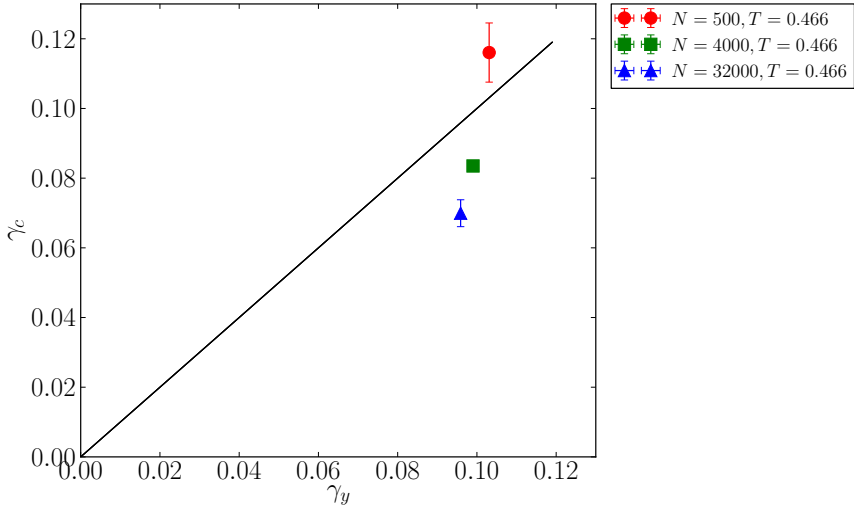


Figure 3.17: Values of  $\gamma_c$  determined from the fits in Figure 3.9 of the diffusion against the values of  $\gamma_y$  determined from the fits in Figure 3.16.

Consequently, upon deformation, the average potential energy of the samples reaches a fixed value that depends on the initial effective  $T$  and on the amplitude of the deformation  $\gamma_{max}$  (Figure 3.4). The amount of cycles needed to reach such fixed value depends on the oscillation amplitude  $\gamma_{max}$ , and is seen to increase dramatically as  $\gamma_{max}$  approaches  $\gamma_c$  (Figure 3.5). Absorbing states below  $\gamma_c$  are characterized by narrow hys-

teresis curves and by a low amount of energy dissipation (Figure 3.14 and Figure 3.15). Above  $\gamma_c$ , systems move indefinitely in configuration space as more and more deformation cycles are performed. Motion under cyclic deformation is characterized by loss of memory of the initial effective temperature  $T$ . In fact, after some number of deformation cycles, samples assume states whose potential energy fluctuates around a value that depends on  $\gamma_{max}$  only. The number of cycles needed to reach such steady energy state depends on  $\gamma_{max}$ , and increases as  $\gamma_{max}$  approaches  $\gamma_c$ . In this regime samples exhibit large values of energy dissipation per cycle, and wide hysteresis curves.

By looking at the mean squared displacement of samples with  $\gamma = 0$ , the overall particle dynamics both below and above  $\gamma_c$  can be approximated as a random walk of walkers having a finite probability to halt their motion (Figure 3.7). In the steady state, a simple linear model is able to describe the MSD of the systems (Figure 3.8). Interestingly, the diffusion constants measured for the various systems can be described by a power-law model (Equation 3.9). This is the same model used to fit the behavior of noncolloidal suspensions in [55] (see Equation 1.10). The power-law behavior observed in noncolloidal suspensions was rationalized in [55] by means of a mapping to the problem of conserved directed percolation [56], which exhibits a non-equilibrium transition. However, it is not clear how a dense system like ours could be mapped onto a directed percolation problem [81]. In this sense, more precise measurements of the characteristic accumulated strain needed to reach asymptotic values of the potential energy under deformation and more precise data about particle diffusion in the vicinity of  $\gamma_c$  could allow to place our systems into a non-equilibrium universality class.

The analysis of particle motion under deformation reveals another interesting detail: for our largest system size ( $N = 32000$ ) we observe that above  $\gamma_c$  particles that move the most organize in bands (Figure 3.11) that occupy the same position in the simulation box as more and more deformation cycles are performed. To our knowledge, this is the first observation of “shear bands” in simulations of systems under oscillatory shear employing Lees-Edwards boundary conditions. The spatial heterogeneity in particle motion suggests that particle diffusion won’t be isotropic (for instance, particles in a band will preferentially move in the plane of the band rather than orthogonally to it), and can’t thus be described by simple isotropic diffusion. A more detailed analysis of such features of the dynamics would allow to explore all these aspects quantitatively.

The value of  $\gamma_c$  has been compared to that of yield strain  $\gamma_y$ . Several definitions of  $\gamma_y$  exists, and in our case we have considered  $\gamma_y$  to be the strain corresponding to the peak in the shear stress-strain curve (Figure 3.16). Even though the two values must be correlated (in fact, there can’t be particle diffusion without the system deviating from a perfectly elastic behavior and thus “yielding” in some way), they refer to the properties of quite different objects:  $\gamma_c$  is extrapolated from the properties of oscillatory deformed samples in their steady state, whereas  $\gamma_y$  is a property of undeformed samples. We indeed find that in our samples  $\gamma_c$  and  $\gamma_y$  are significantly different at the different system sizes that we have analyzed (Figure 3.17). In addition, we don’t expect this result to be influenced by our choice of definition of  $\gamma_y$ .

### Chapter 3. Results from Lennard-Jones simulations

---

Even though the value of  $\gamma_c$  shows a significant size dependence, our data in Figure 3.10 suggest that  $\gamma_c$  will remain larger than 0 as  $N$  becomes large. This makes us conclude that our results (and in particular the existence of a transition at  $\gamma_c$ ), even though affected by finite size effects, will be valid at macroscopic scales.

# 4 Toy models of athermal deformation

Simulations of athermal deformation of Lennard-Jones systems are expected to give insight about the behavior of slowly oscillatory sheared particle systems. Understanding the phenomenology observed in such simulations, however, appears as a daunting task. The main difficulty arises from the complicated AQS dynamics in a highly dimensional configuration space. A fruitful strategy to get a clearer idea of what are mechanisms that lead to the transition observed at  $\gamma_c$  in chapter 3 is the development of toy models. These should be more easily tractable and understandable (ideally analytically solvable), but still show the key phenomenology observed in the Lennard-Jones simulations. In this chapter, for this scope, we describe and employ two models: the NK model [47], which we describe in section 4.1, and the TM (transition matrix) model, a novel representation that treats AQS deformation cycles as transition matrices and is described in section 4.2. With the aid of such toy models, the essential ingredients needed to observe the same phenomenology seen in the Lennard-Jones simulations can be identified. One example of common behavior observed in all these systems (LJ, NK and TM models) is the capability to retain a memory of their history, similarly to what is observed in the noncolloidal suspensions in [58]. We will deal with this subject separately, in chapter 5.

## 4.1 NK model

In this section we review the so-called NK model mentioned in chapter 1 and used in [47] to get insights about rejuvenation and overaging in glasses<sup>1</sup>. This model takes its name from the two main parameters in it. In what follows, we perform (whenever possible) on it measurements that are equivalent to those performed on the LJ system in chapter 3. In this sense we extend the work in [47] on the NK model to multiple driving cycles, in the same way as chapter 3 extends the study in [45] on LJ systems.

---

<sup>1</sup>The only difference between our version of the NK model and that in [47] is the addition of the constraint of constant sum of the values of the spins.

### 4.1.1 Features of the NK model

The NK model is constructed on a lattice of  $N$  (even) lattice sites occupied by “spins”  $m_i$  that can take either the values 0 or 1.

$$\{m_1, m_2, \dots, m_i, \dots, m_N\} \in \{0, 1\}^N \quad (4.1)$$

Furthermore, we limit (for reasons clarified in Appendix C) the space of allowed configurations to those that satisfy the constraint

$$\sum_i m_i = \frac{N}{2} \quad (4.2)$$

(this is equivalent to taking the set of states of constant magnetization  $N/2$  in the Ising model). There are  $\binom{N}{N/2}$  such configurations. From a geometrical point of view these configurations are the  $N$ -tuples that identify the coordinates of the vertices which define a  $N$ -dimensional unit hypercube and that lie on the  $\sum_i m_i = N/2$  hyperplane.

In addition, we introduce:

- an ordered list of  $K$  “neighbors” for each  $i$ -th spin, specified by the map  $J$ :

$$m_i \xrightarrow{J} \{m_i^1, \dots, m_i^K\} \quad (4.3)$$

The choice of the list of neighbors for a given spin is random.

- two functions  $a$  and  $b$  connecting the set  $\{0, 1\}^{K+1}$  (the set of all the  $(K+1)$ -tuples formed by ones and zeros) to the intervals  $[-1, 1]$  and  $[0, 1]$  respectively

$$\{0, 1\}^{K+1} \xrightarrow{a} [-1, 1] \qquad \qquad \qquad \{0, 1\}^{K+1} \xrightarrow{b} [0, 1] \quad (4.4)$$

The correspondence between a given  $(K+1)$ -tuple and the numerical value is chosen randomly with a uniform probability within the respective intervals.

The energy of the system depends on the values of the spins,  $E = E(m_1, \dots, m_N)$  according to

$$E = -\frac{1}{2} \sum_{i=1}^N [1 + \sin(2\pi(a_i + \gamma b_i))] \quad (4.5)$$

where  $\gamma$  is a parameter that can be varied continuously.

In addition, we define two NK configurations as adjacent if one is turned into the other by swapping the values at two sites  $i$  and  $j$  such that  $m_i \neq m_j$ . Said in geometrical terms, two configurations are adjacent if they represent two vertices that lie at the extremes of a diagonal of a face of the  $N$ -dimensional unit hypercube. Each configuration has thus

$N^2/4$  configurations that are adjacent to it.

### 4.1.2 Energy landscape of the NK model

The NK model is known to possess a discrete energy landscape whose roughness (a measure of which is given by the number of local minima in the landscape) is tuned by the value of the parameter  $K$ . The landscape is smooth for  $K = 0$  and the roughness is increased as  $K$  is increased. To see this consider the case  $\gamma = 0$  for simplicity. If  $K = 0$ , when performing the sum in Equation 4.5 one sums contributions that are simply  $1 + \sin(2\pi a_i)$ , where  $a_i$  can assume only two values in the interval  $[-1, 1]$ , depending solely on whether  $m_i = 1$  or  $0$ , as no spin has neighbors. It's clear that the energy increases or decreases monotonically with the "magnetization"  $\sum_i m_i$ . As in our case such quantity is fixed, all the allowed configurations have the same  $E$ . This implies that by moving from a given configuration to any adjacent one the energy can't change and the landscape is thus *flat*. In the case  $K = N - 1$  each spin is a neighbor of any other. To estimate the roughness of the landscape, we compare the energies of two adjacent structures, that differ by the swapping of two spins. Each term in Equation 4.5 is affected by such a swap, and so all the  $a_i$ 's that contribute to the energy of the two configurations differ. Being the  $a_i$ 's random and uncorrelated, there won't be correlation between the energies of two adjacent configurations. Consequently, the structure of the overall landscape will be rough.

While  $K$  is able to tune the roughness of the landscape, the parameter  $\gamma$  is able to change continuously the values of the energy of the configurations (and thus the overall landscape). This is similar to what happens in a Lennard-Jones system, in which a macroscopic strain is externally imposed. For this reason, with a slight abuse of terminology,  $\gamma$  will be called "shear strain" also in the context of the NK model in what follows.

A graph representation of the landscape for low values of  $N$  and  $K$  is given in Figure 4.1. Nodes represent single configurations, and edges connect adjacent configurations. To summarize, the NK model is similar to the LJ model because it possesses a rugged energy landscape which is deformable by varying the parameter  $\gamma$ , and concepts and protocols that apply for the latter can be transferred to the former. For instance, starting from an initial configuration, energy can be minimized by a steepest descent (SD) procedure. A SD in the NK energy landscape consists in moving from a configuration to the adjacent one with the lowest  $E$ , and iterating this procedure until when no move to an adjacent configuration results in a decrease in  $E$ . Using such a protocol, any configuration can be mapped onto a local minimum, i.e. an inherent structure of the NK landscape. This fact, together with the dependence on  $\gamma$  of the landscape, allows to define an athermal quasi static "deformation" procedure on NK systems too. The procedure follows closely that described in section 2.3:

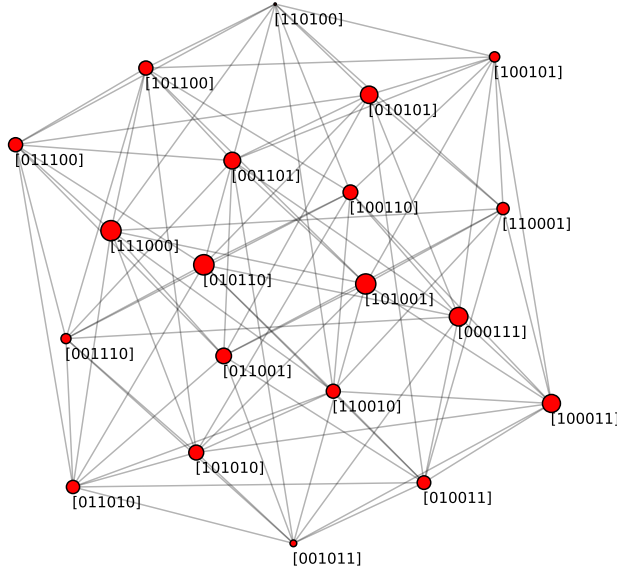


Figure 4.1: Graph representation of the space of configurations of the NK model with  $N = 6$ . In this case, only 20 configurations are allowed. Edges in the graph connect adjacent configurations, and the size of the node denotes the value of  $E$  (in arbitrary units), with bigger nodes indicating a lower energy. As  $\gamma$  in Equation 4.5 is changed, one can imagine that the sizes of the nodes vary accordingly. Following the steepest descent (SD) starting from a given node, in this case, means moving from node to node by choosing the largest node accessible via an edge at each step.

1. Take an inherent structure of the NK landscape. This can be obtained by any configuration by means of the SD algorithm.
2. Increment the value of  $\gamma$  in Equation 4.5 by a small amount  $d\gamma$ . As in the LJ case, the value of  $d\gamma$  should be small enough so that the modification of the landscape is slow enough and no displacements to adjacent inherent structures are “missed”<sup>2</sup> by the AQS dynamics.
3. Apply the SD procedure to the configuration.

As AQS can be applied to the NK model, it’s interesting to check whether the same phenomenology seen in AQS deformation of Lennard-Jones systems can be observed in it. However, one should be aware that the two models still bear differences:

- The NK model has a *discrete* configuration space. This makes the AQS dynamics of NK systems somewhat different to that of LJ systems. In the NK case, the system occupies one given point of the available configuration space as  $\gamma$  is changed, and stays there until it “jumps” to another inherent configuration as soon as the initial point is not an inherent configuration anymore. In the LJ case, instead, systems do *always move* in the configuration space as  $\gamma$  is varied (as described in section 2.3).
- Due to the discrete nature of the landscape, minimization is trickier in the NK case. While in the LJ case *local* quantities (e.g. the calculation of a potential energy gradient) allow to determine the direction to follow to reach an inherent structure, in the NK model *all* the energies of adjacent configurations need to be calculated in order to choose the adjacent configuration with the lowest energy (if there is one). This operation requires  $O(N^2)$  energy calculations to be performed (as the number of adjacent configurations scales with  $N^2$ , see above) and is thus computationally unfeasible for large values of  $N$ . More details about the complexity of the minimization in the NK space are reported in Appendix C.
- While the LJ energy landscapes depend on the values of the  $\epsilon$  and  $\sigma$  parameters in Equation 2.1 and the boundary conditions of the simulation boxes, the definition of the landscape in the NK case requires the introduction of a much larger number of parameters. This is because the lists of neighbors specified by  $J$  can be realized in many different ways<sup>3</sup>, and  $a$  and  $b$  in Equation 4.3 and Equation 4.4 require  $2^K$  values each to be defined.

---

<sup>2</sup>In other words,  $d\gamma$  should be small enough that if a smaller  $d\gamma'$  was employed it would yield exactly the same evolution.

<sup>3</sup>The number of ways in which  $J$  can be chosen is related to the number of possible “friendship networks” in a group of  $N$  people if everyone has  $K$  friends and “friendship” is a symmetric relation (so that if  $A$  is a friend of  $B$  then  $B$  is a friend of  $A$ ). In more formal terms, this is also related to the number of *regular graphs* having degree  $K$  (as in the NK model each spin has  $K$  other spins coupled to it) and  $N$  vertices. Actually this number cannot be expressed in a closed form (only asymptotic results exist in the literature)!

Having noted this, we can study the NK model under athermal quasi-static deformation, and compare the results with what is obtained with the LJ model. Such comparison is meaningful, because the two systems share important features. At the same time it's not trivial, because, as explained above, the two models are “sufficiently different” so that a common qualitative behavior can't be taken for granted a priori.

## 4.2 Transition matrix (TM) model

Both the LJ and NK models possess a rugged landscape that is modified during the deformation. The behavior under oscillatory deformation, in particular, thus depends on the detailed features of the landscape. Would it be possible to predict the behavior of such models qualitatively, without encoding in detail the features of the energy landscape, but using a sort of “high-level”, abstract description of its evolution? This is what the “transition matrix” method (TM) aims to do, by exploiting some of the ideas already outlined in section 2.3. A nice feature of it is that it provides a description that can be applied both to the LJ and NK models.

The starting point of the TM approach is to look at a cycle of AQS deformation from a mere “mathematical” point of view. In that perspective, an AQS cycle is a correspondence between the set of  $M$  inherent structures of the energy landscape at  $\gamma = 0$  into itself<sup>4</sup>. This is because a valid starting configuration is an inherent structure of the  $\gamma = 0$  landscape, and it is transformed into another inherent structure of the same landscape at the end of the deformation cycle. Each of these inherent structures can be identified by an index  $i$ , and associated to a  $M$ -dimensional vector  $\mathbf{R}_i$  whose components are all zero but for the  $i$ -th one, which is set equal to 1. Then, they can be taken as starting points of a deformation experiment where a single AQS cycle is performed and the inherent structure reached at the end is recorded. This allows to construct a *transition matrix*  $P$ , such that

$$P\mathbf{R}_i = \mathbf{R}_f \tag{4.6}$$

where  $\mathbf{R}_i$  and  $\mathbf{R}_f$  are the vectors associated to the initial and final inherent states. Here we list some of the properties of the  $P$  matrix, which descend directly from the features of AQS dynamics:

- $P$  encodes the entire information about the evolution of any inherent structure under cyclic deformation, as by using Equation 4.6 one can determine the final inherent structure  $\mathbf{R}_f$  given any initial one  $\mathbf{R}_i$ .

---

<sup>4</sup>In more mathematical terms, an AQS cycle defines an *endomorphism* of the set of inherent structures of the landscape such that  $\gamma = 0$ .

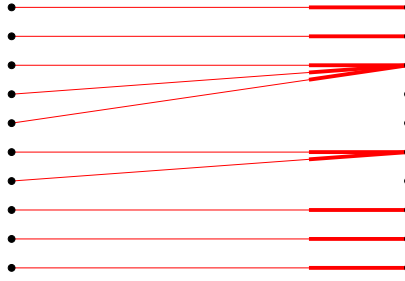


Figure 4.2: Graph representation of an AQS cycle, that has the effect of mapping the set of inherent structures of the  $\gamma = 0$  landscape onto itself. If the application is not injective, it can't be surjective either.

- $P$  is a sparse  $M \times M$  matrix, and  $P_{ij} = 1$  if and only if the state associated to  $\mathbf{R}_j$  is mapped onto the inherent structure  $\mathbf{R}_i$  in the AQS cycle. The consequence is that all the columns have exactly one non-zero entry (equal to one) because each  $\mathbf{R}_j$  configuration is sent to some other  $\mathbf{R}_i$  inherent structure by the AQS cycle.
- $P$  depends on the value of  $\gamma_{max}$ , i.e. on the amplitude of the deformation. For very small amplitudes, a sizable fraction of the inherent structures will be unchanged under the deformation, because an AQS cycle will not be effective at destabilizing the starting inherent structures. In this case a given structure will often map onto itself through  $P$  and thus  $P$  will be very close to the diagonal unit matrix. In general this won't be any longer true for higher values of  $\gamma_{max}$ .
- The determinant of  $P$  is, in general, zero. In general, more than one structure will map onto the same final state  $\mathbf{R}_f$ , so that in that case  $P$  will define a non-injective function. As the domain of  $P$  is also its codomain,  $P$  is not surjective, so that there will be structures that are not arrival configurations for any inherent structure (this is illustrated in Figure 4.2). This has the consequence that some rows of the  $P$  matrix, in general, are identically zero, and so is the value of  $\det P$ .
- $M$ , in general, is a large number. The size of  $P$  is equal to the number of inherent structures of the landscape, and this number, for typical LJ and NK landscapes, is large (exponential in  $N$  in the first case, and equal to  $\binom{N}{N/2}$  in the second).
- The result of a deformation experiment where  $L$  cycles (rather than just one) are applied to a given starting configuration  $\mathbf{R}_i$  is obtained by applying Equation 4.6 repeatedly:

$$P^L \mathbf{R}_i = \mathbf{R}_f \quad \text{where } P^L = \underbrace{P \cdot \dots \cdot P}_{L \text{ times}} \quad (4.7)$$

#### 4.2.1 Classification of states by their transformation properties

A given configuration  $\mathbf{R}_i$  can transform under the effect of  $P$  in different ways:

1.  $P\mathbf{R}_i = \mathbf{R}_i$ : in this case  $P$  has no effect on  $\mathbf{R}_i$ , so that  $\mathbf{R}_i$  is an eigenvector of  $P$  relative to the eigenvalue 1, and  $P_{ii} = 1$ . We name such a  $\mathbf{R}_i$  an *absorbing* state, in agreement with the usage of this term in chapter 3 in the context of absorbing LJ states.
2.  $P^L\mathbf{R}_i = \mathbf{R}_i$  for some  $L > 1$ : in this case the oscillatory deformation starting from  $\mathbf{R}_i$  makes it cycle through a sequence of states, and after  $L$  cycles  $\mathbf{R}_i$  is reached again.  $\mathbf{R}_i$  an eigenvector of  $P^L$  relative to the eigenvalue 1. We name such a  $\mathbf{R}_i$  a *recurring* state.
3.  $P^J\mathbf{R}_i = \mathbf{R}_{\text{abs}}$  for some  $J \geq 1$ , where  $\mathbf{R}_{\text{abs}}$  is an absorbing state. We name such a  $R_i$  as *mapping to absorbing state*.
4.  $P^J\mathbf{R}_i = \mathbf{R}_{\text{rec}}$  for some  $J \geq 1$ , where  $\mathbf{R}_{\text{rec}}$  is a recurring state. We name such a  $R_i$  as *mapping to recurring state*.

Note that *every* configuration falls in one of the categories enumerated above. This can be demonstrated as follows: suppose that a configuration  $\mathbf{X}$  exists that doesn't fall in any of the categories listed above. If  $P$  is applied to it, then some other configuration  $\mathbf{Y}_1 \neq \mathbf{X}$  is obtained, else  $\mathbf{X}$  would belong to the category in item 1. Repeated application of  $P$  yields always new states  $\mathbf{Y}_2, \mathbf{Y}_3, \dots$ , so that no absorbing nor recurring states are encountered, else  $\mathbf{X}$  would belong to one of the categories in item 2, item 3 or item 4. After  $M$  applications of  $P$ , a sequence of  $M+1$  distinct inherent configurations has been generated, but only  $M$  distinct inherent structures exist! So the initial hypothesis (the very existence of  $\mathbf{X}$ ) can't be true.

What is the correspondence between this classification of states and the absorbing and the diffusive states encountered in chapter 3? Absorbing states of the LJ models clearly correspond to those of the TM model. Diffusing states in the LJ models correspond to the recurring states of the TM picture. In fact, even though a diffusing LJ system does not seem to revisit the same inherent structure as it travels in configuration space, after a large number of oscillation cycles it *has to*, as the number of possible inherent structures is finite<sup>5</sup>. Thus the diffusing states of chapter 3 can be viewed as recurring states, which just take a *very* large number of cycles to come back to their starting state.

---

<sup>5</sup>However, in our LJ simulations, this is true only if particle coordinates are forced to be wrapped into the volume of the simulation box, an operation that was *not* performed by us when computing the MSD.

### 4.2.2 Construction of the $P$ matrix

The  $P$  matrix contains the entire information about the outcome of oscillatory AQS deformation, but how can one construct it? Computing it for LJ or NK systems can in principle be done by brute force: one needs to have a list of the inherent structures, use each of them as a starting configuration for a shear deformation cycle and see which structures they eventually reach at the end of the cycle. This idea is easier to apply for the NK model than in the LJ case: in the former one can (at least in principle) enumerate all the  $\binom{N}{N/2}$  allowed configurations, minimize each and every one of them so to get all the inherent structures of the landscape; in the latter, which has a continuous energy landscape and a continuous set of configurations, the determination of the local minima of the landscape is a less trivial task<sup>6</sup>. The unfeasibility of a brute force approach is the reason why one would like to construct  $P$  by less expensive means, albeit in an approximate way. To do so, we make a series of observations and assumptions about the evolution of the energy landscape, that allow to construct  $P$ .

#### Axioms of the TM model

The TM model is based on some assumptions on the dynamics of inherent structures in the course of a deformation cycle:

1. During the deformation (at non-zero values of  $\gamma$ ) the number of energy minima is assumed to be *always* equal to  $M$ , no matter the value of  $\gamma$ . The number of local minima present in the landscapes of LJ and NK models will, in general, weakly<sup>7</sup> depend on the value of  $\gamma$ .
2. Minima are destabilized by changing  $\gamma$ , i.e. that some of them are destructed by the deformation. As the number of structures is assumed to be conserved (see above) to each inherent structure destruction corresponds the creation of a new one.
3. The probability per unit strain of an inherent structure to be destabilized is assumed to be the same for all the  $M$  structures and equal to a value  $\tau$  independent from  $\gamma$ .
4. A system sits on a given inherent structure until such inherent structure is destabilized. When this happens, the system jumps to another inherent structure of

---

<sup>6</sup>Also in the NK case, however, this brute force approach to the determination of  $P$  is very expensive computationally, as  $\binom{N}{N/2}$  minimizations need to be performed at every AQS step.

<sup>7</sup>A weak dependence of the number of inherent structures in a Lennard-Jones system can be justified by the fact that one does not expect that the physics of a system depends on the boundary conditions. The detailed energy landscape of the system will depend on the value of  $\gamma$  in a simulation that employs Lees-Edwards conditions, but the *statistical* properties of the system (like the value of  $M$ ) will not vary much with it.

the deformed landscape. For simplicity such a structure is assumed to be picked at random in the landscape (whereas, in a realization of the NK or LJ models, a system will land on a structure which is not far from the starting one in the space of configurations).

In addition, the model relies on two facts that are true in general:

5. As a deformation *semicycle* brings the system from 0 up to  $\gamma_{max}$  and then back to the undeformed landscape, there is a *symmetry* in the structures that are created and destroyed as  $\gamma$  is incremented from 0 to  $\gamma_{max}$  and those that are created/destroyed as  $\gamma$  is reduced back to 0 in the second part of the semicycle. In fact, if a structure **R** is destroyed when incrementing  $\gamma$  above some value  $\gamma^*$ , the same structure **R** will be created at  $\gamma^*$  as the deformation is reversed. The converse is true for a structure **S** that is created in the first half of the semicycle.
6. The matrix  $P$  can be viewed as the product of  $P_+$  and  $P_-$ , the matrices that describe the two semicycles (one denoted by positive, the other by negative strain  $\gamma$ ) that form a full oscillation cycle.

A description of how these assumptions and observations are combined to calculate an approximation of the  $P$  matrix is presented in Appendix D. A graphical and more intuitive way to present how the assumptions above can be used to construct the  $P_+$  (or  $P_-$ ) matrix is given below.

#### 4.2.3 Intuition for the TM model

A graphical representation of the effect of the assumptions of the TM model listed above in subsection 4.2.2 can be useful to clarify their meaning and their limitations. In Figure 4.3 we show “configuration space -  $\gamma$ ” diagrams in a sequence displaying an increasing number of details of the model. It is very important to note that Figure 4.3 is nothing but a representation equivalent to that seen in Figure 2.4 and Figure 2.8 in the discussion of the evolution of inherent structures and the dynamics of systems in a deforming energy landscape in chapter 2. In Figure 4.3, minima are represented as black dots, and those belonging to the same energy landscape are aligned on the same vertical line (whereas they were represented as lying on the same plane in Figure 2.4). The incremental strain  $\gamma_{acc}$  changes in steps of  $d\gamma$  when moving from the left to the right. As dictated by the assumption of conservation of the number of  $M$  inherent structures, on each vertical line in Figure 4.3 lie always  $M$  inherent structures. The red lines represent the energy landscapes relative to  $\gamma = 0$ , and the green one represents the landscape such that  $\gamma = \gamma_{max}$ . The higher the value of  $\gamma_{max}$  the higher the number of columns that are present in the diagram. In addition, as  $\gamma$  is incremented, structures can

## 4.2. Transition matrix (TM) model

---

survive (so that they're connected continuously to an inherent structure of the deformed landscape) or have some probability  $\tau d\gamma$  to be destroyed. In Figure 4.3b, only if a structure survives it is connected with a black segment to its corresponding inherent structure in the deformed landscape. If a structure is destroyed, a new one needs to be created in the deformed landscape in order to ensure the conservation of the number of structures. In Figure 4.3b, for simplicity, the newly created inherent structures are placed on the same line of those that have been destroyed. Note also that, in order to respect the symmetry of the energy landscapes, the connections between minima must be symmetric with respect to the green line denoting the  $\gamma = \gamma_{max}$  landscape in Figure 4.3b. The continuous connections between minima in black in Figure 4.3b represent the “skeleton” over which AQS dynamics takes place. A system in a given inherent structure will follow the black connections up to when they turn out to be “dead ends” as the inherent structure is destroyed. As the system witnesses the destruction of the inherent structure that it is occupying, it will jump to another inherent structure of the deformed landscape as  $\gamma$  is increased. The trajectory followed by systems initially located in different minima is drawn with red arrows in Figure 4.3c. The evolution of a single minimum can be traced in Figure 4.3c by simply following the arrows<sup>8</sup>. By doing so, one can see the effect that a single cycle of deformation has on the configurations, and reconstruct the matrix  $P_+$  by seeing which structures map into which. The matrix encoded in the red directed graph in Figure 4.3c is displayed in Figure 4.4, showing that the “graph representation” that we've just described is not only useful to illustrate the TM model, but can be used to construct the  $P_+$  and  $P_-$  matrices. The same construction can be repeated for a different value of  $\gamma_{max}$  (Figure 4.3d), thus allowing to construct  $P_\pm$  matrices associated to different oscillation amplitudes.

The construction of the graphs described above can be implemented in a computer program (by using graph manipulation libraries such as NetworkX). It turns out, however, that the matrix approach followed in Appendix D is computationally more efficient.

---

<sup>8</sup>In other (and more precise) terms, one takes a node on the left of the directed graph in red in Figure 4.3c and looks at the list of its successors in the directed graph. If one does so one can see that in the graph in Figure 4.3c, if structures in the  $\gamma = 0$  landscape on the left and on the right of the diagram are labeled with increasing indices, one gets the correspondences  $1 \rightarrow 1, 2 \rightarrow 2, 3 \rightarrow 3, 4 \rightarrow 3, 5 \rightarrow 3, 6 \rightarrow 6, 7 \rightarrow 6, 8 \rightarrow 8, 9 \rightarrow 9, 10 \rightarrow 10$ . These correspondences are expressed in matrix form in Figure 4.4.

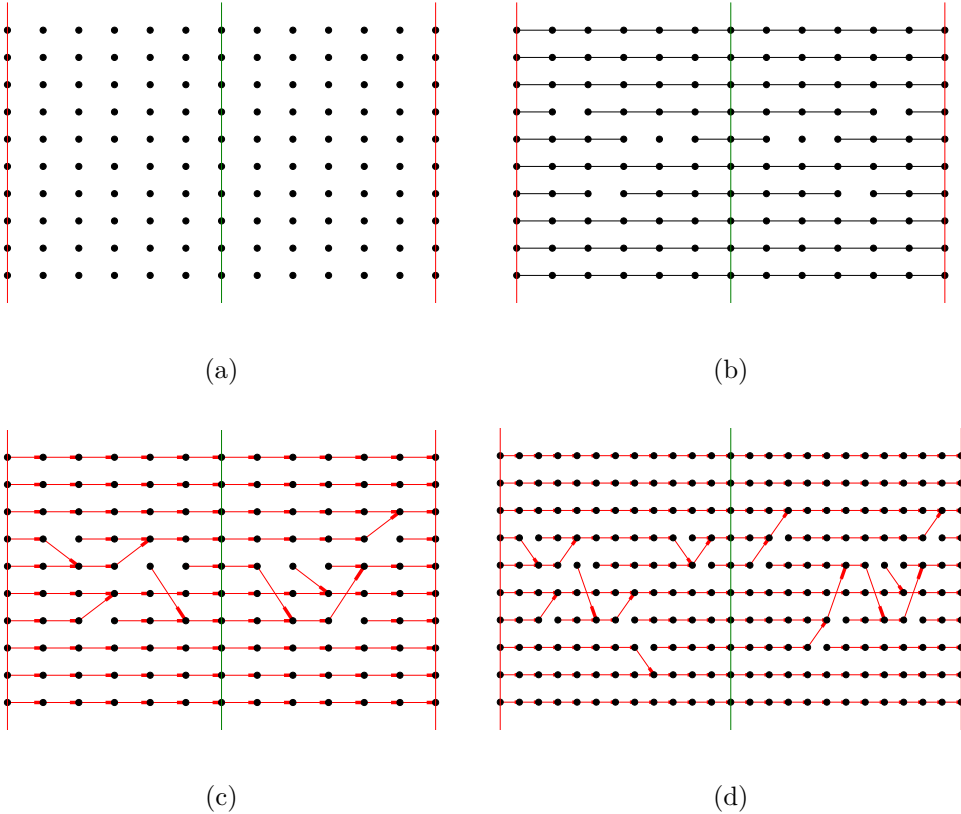


Figure 4.3: Diagrams exemplifying the assumptions of the TM model. It can be seen as a even more stripped down version of Figure 2.4. In (a), just the minima of the energy landscapes associated to different values of  $\gamma$  are plotted as black dots, with structures in the same landscape aligned on the same vertical line as  $\gamma_{acc}$  is increased. The red lines represent the  $\gamma = 0$  energy landscape, and the green one the  $\gamma = \gamma_{max}$  landscape. In (b), minima that continuously transform into each other as  $\gamma_{acc}$  is changed are connected by black segments. If a structure is destroyed, it has no connection to any inherent structure on its right, whereas if an inherent structure is created, it is not connected to any minimum on its left. In (c), the AQS dynamics of the systems moving from inherent structure to inherent structure is represented by red arrows. Whenever an inherent structure is destroyed, systems choose randomly a new inherent structure, accordingly to the assumptions of the TM model. The result is a directed graph that can be used to construct the  $P_+$  and  $P_-$  matrices associated to  $\gamma_{max}$ . In (d), the same construction is applied for a different (larger) value of  $\gamma_{max}$ , obtaining a graph which extends the one in (c) and has additional nodes in correspondence of the green line.

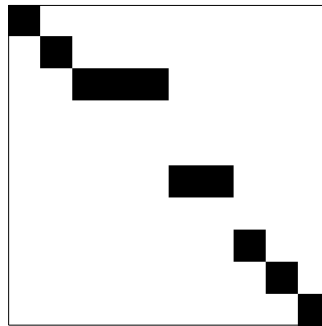


Figure 4.4: Matrix  $P_+$  summarizing the correspondences between the inherent structures in the graph in the directed graph in Figure 4.3c representing AQS dynamics. A black (or white) square at position  $(i, j)$  means that the entry at that position is one (or zero). A square at the position  $(i, j)$  is black if the inherent structure  $j$  maps into the structure  $i$  through the AQS cycle represented in Figure 4.3c.

### 4.3 Results from the NK model

The NK and the LJ models share enough similarities so that one can perform on the former measurements that mirror those that have been performed on the latter in chapter 3. In particular, the NK model possesses a deformable but *discrete* energy landscape, that can be deformed in an oscillatory way. In what follows we show that the ingredients that the NK model retains are sufficient to display (at least qualitatively) the behavior observed in binary LJ mixtures, and in particular the existence of an absorbing to diffusive behavior transition at  $\gamma_c$ . The study of the NK model is thus helpful to single out the features of the LJ model that lead to the transition.

Unless noted otherwise, results below are averaged over  $\approx 200$  different instances of the couplings  $a$ ,  $b$  and  $J$  in Equation 4.3 and Equation 4.4, and obtained with a C code written by the author (see Appendix F).

#### 4.3.1 NK at equilibrium

Before performing simulations of “deformation” on NK samples one needs configurations to start from. As in the case of the LJ systems discussed in chapter 3, one would like to start from sets of configurations that differ for some feature (like the average potential energy). In this way one can check how deformation affects the samples, and how it is capable of making them evolve in such a way to forget their initial state. The obvious choice is to choose inherent structures differing for their effective  $T$ , exactly as in the LJ case. Similarly to what has been performed in the case of particle systems above, we obtain several equilibrated NK configurations at different  $T$ . We do this for several realizations of the couplings  $a$ ,  $b$  and  $J$  by means of Monte Carlo sampling and find their

inherent structures of effective temperature  $T$  by means of steepest descent (SD). The average energy of such inherent structures is plotted in Figure 4.5, showing a behavior similar to that observed in Figure 1.8. Even though the energy  $U$  of inherent structures

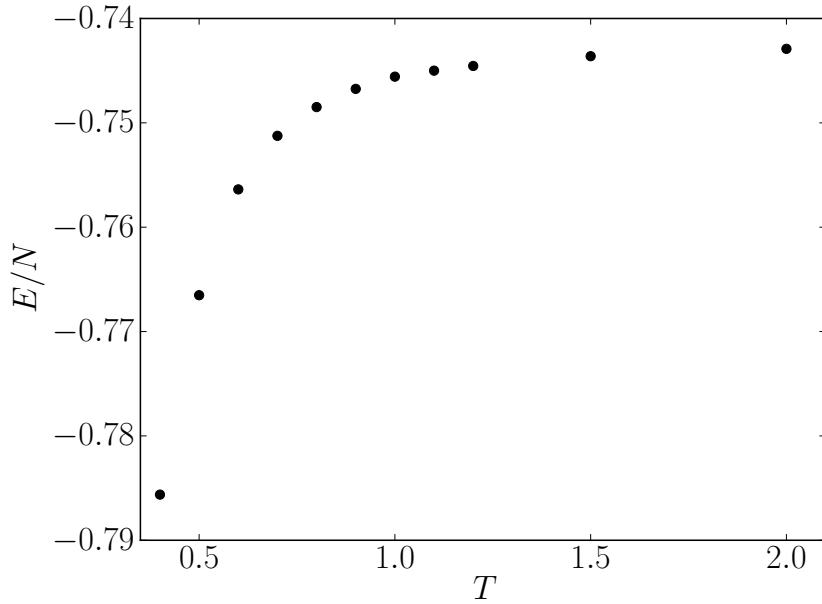


Figure 4.5: Average energy per site of the inherent structures obtained by quenching NK samples ( $N = 20$ ,  $K = 10$ ) equilibrated at different  $T$ . The plot bears a qualitative similarity with what is observed in particle models (see Figure 1.8 for a comparison).

is expected to be a monotonically increasing function of  $T$ , the between Figure 4.5 and Figure 1.8 is not entirely trivial, because it stems from the DOS of the inherent states and from the way in which inherent structures are connected with each other in the landscapes of the NK and KA models. Such analysis allows us to state that inherent structures at the effective temperatures  $T = 0.6$  and  $1.0$  are different enough to be distinguished. These values are thus selected as effective temperatures of choice for the initial inherent structures.

### 4.3.2 Evolution of the energy under deformation

We consider  $N = 20, 40, 80$  and  $K = 10$ , take  $\approx 200$  instances of the couplings and obtain 3-4 equilibrated configurations at  $T = 0.6$  and  $1.0$  for each of such instances. The corresponding inherent structures obtained by SD are deformed by increasing  $\gamma$  in Equation 4.5 in steps of  $d\gamma = 0.005$  (for all  $N$ ) and performing SD at each step. The parameter  $\gamma$  is varied in the interval  $[-\gamma_{max}, \gamma_{max}]$  in a triangle wave fashion, exactly as in the AQS simulations seen in chapter 3. The values of  $E$  and the configuration are recorded whenever  $\gamma = 0$ , i.e. at intervals of  $2\gamma_{max}$ . Plots of  $E$  as a function of  $\gamma_{acc}$

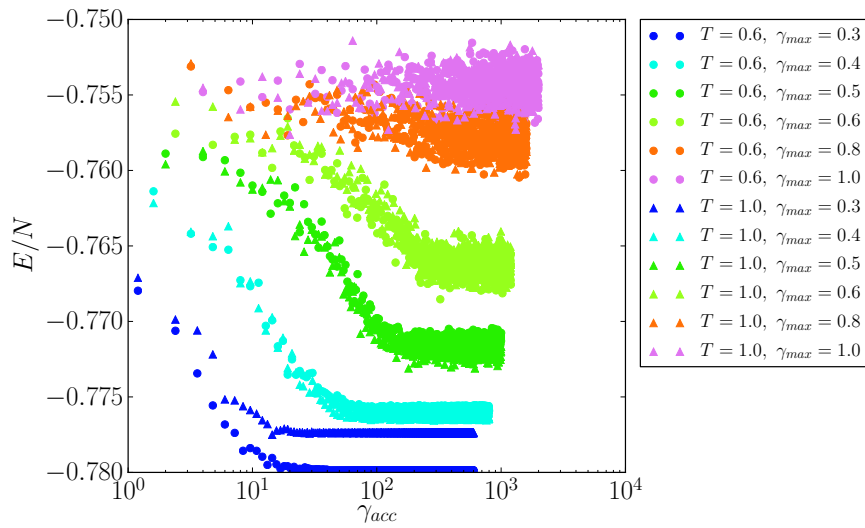


Figure 4.6: Potential energy per site as a function of  $\gamma_{acc}$ , for different initial effective temperatures and different deformation amplitudes  $\gamma_{max}$ , setting  $N = 40$ ,  $K = 10$ . Data refer to configurations with  $\gamma = 0$ . For large values of  $\gamma_{max}$  the energy fluctuates around some value which depends on  $\gamma_{max}$  only. At small  $\gamma_{max}$ , instead, the plateau value of the energy depends on the effective  $T$  of the initial configuration. In this respect what is observed here qualitatively resembles what has been found in particle models in Figure 3.4.

(defined in the same way as in Equation 2.5) are shown in Figure 4.6 for the  $N = 40$  case. Similarly to what is observed in the LJ case, for small values of  $\gamma_{max}$  the energy reaches a plateau which depends on *both*  $\gamma_{max}$  and the initial effective  $T$ . For higher values of  $\gamma_{max}$ , all samples, regardless their initial effective  $T$ , reach plateau depending on  $\gamma_{max}$  only. In this respect, the NK model is able to reproduce qualitatively the same behavior found in Figure 4.6, where samples forget about their initial preparation if the oscillation amplitude exceeds some value  $\gamma_c$ . Unlike the KA systems however, the NK model exhibits a peak in  $E$  before the plateau, and thus can not be fit with a function of the form given in Equation 3.3.

### 4.3.3 Diffusion behavior

Changes in configurations under deformation can be studied for NK configuration as well, by looking at the distance between configurations before and after the application of deformation cycles. Consider two configurations,  $\mathbf{R}(\tilde{\gamma}_{acc})$  and  $\mathbf{R}(\gamma_{acc})$ , obtained for values of the accumulated strain equal to  $\tilde{\gamma}_{acc}$  and  $\gamma_{acc}$  respectively, with  $\tilde{\gamma}_{acc} < \gamma_{acc}$ .

Their distance can be expressed using the Hamming definition<sup>9</sup>  $d$ :

$$d(\gamma_{acc} - \tilde{\gamma}_{acc}) = \frac{c_{01} + c_{10}}{N}, \quad (4.8)$$

where  $c_{01}$  ( $c_{10}$ ) is the number of occurrences such that the  $i$ -th component of  $\mathbf{R}(\tilde{\gamma}_{acc})$  and the  $i$ -th component of  $\mathbf{R}(\gamma_{acc})$  are respectively equal to 0 and 1 (to 1 and 0). We thus pick a configuration  $\mathbf{r}_1$ , choosing a large enough  $\tilde{\gamma}_{acc}$  so that the corresponding  $E$  in Figure 4.6 has relaxed to a steady state. We then compute the Hamming distance from it for configurations reached for increasing values of  $\gamma_{acc}$ , and plot it in Figure 4.7. Differently to what has been observed in Figure 3.8, samples don't show a diffusion behavior. In fact, the average Hamming distance measured starting from a reference configuration in the steady state quickly reaches a constant value for increasing  $\gamma_{acc}$ . This can be explained by the fact that when averaging the Hamming distance over many samples one is averaging over states that are absorbing (so that their Hamming distance is zero for any value of  $\gamma_{acc}$ ) and others that quickly decorrelate from the reference state (so that the Hamming distance is 0.5). The observed value of the Hamming distance thus depends from the fraction of absorbing over non-absorbing states.

By plotting the average of such a value as a function of  $\gamma_{max}$  for different values of  $N$  (see Figure 4.8), one observes that the capability of the system to move away from the reference configuration increases sharply at some value  $\gamma_c$ , which is roughly  $N$  independent. The sharpness of the transition, moreover, is seen to increase with  $N$ . These data thus seem to confirm that a transition at some oscillation amplitude  $\gamma_c$  from a localized regime to a diffusive one exists in the NK model, similarly to what is observed in our KA mixtures in chapter 3 and models of particle suspensions studied in [58] (see subsection 1.3.1).

---

<sup>9</sup>In simpler terms,  $d$  is the fraction of disagreeing components of the two vectors  $\mathbf{r}_1$  and  $\mathbf{r}_2$ .

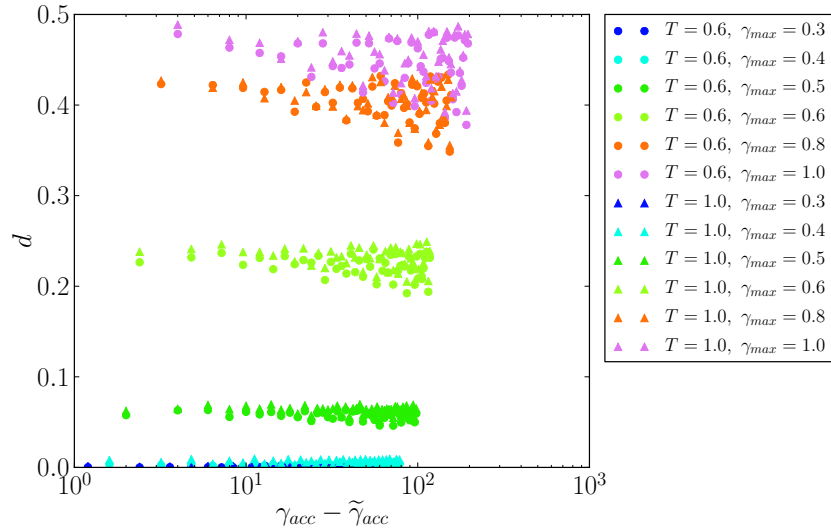


Figure 4.7: Hamming distance as a function of the accumulated strain measured from reference configurations with  $\gamma_{acc} > \tilde{\gamma}_{acc}$ , where  $\tilde{\gamma}_{acc}$  marks the reaching of the plateau of the energy in Figure 4.6.  $N = 40$  and  $K = 10$ . The behavior is not diffusive, but the higher the  $\gamma_{max}$ , the further the systems are able to move away from the reference configuration. The Hamming distance can be modeled with a constant function of  $\gamma_{acc} - \tilde{\gamma}_{acc}$ .

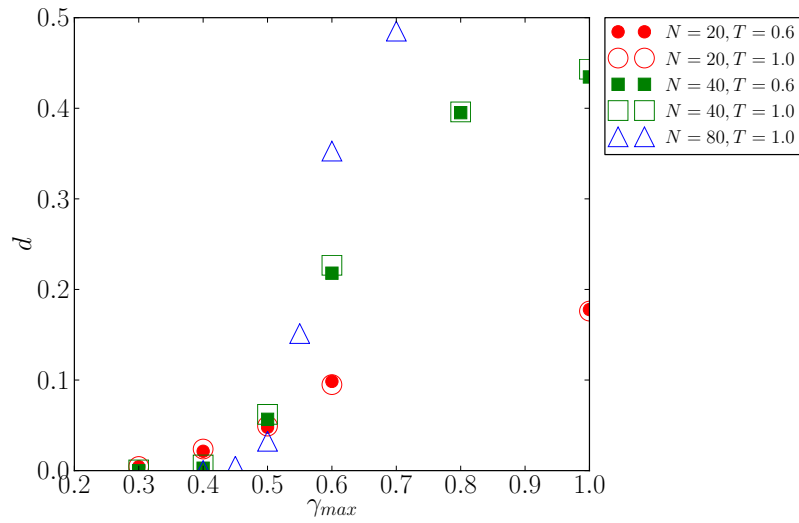


Figure 4.8: Average value of the Hamming distance as determined by averaging data like that in Figure 4.7, for different  $N$  and setting  $K = 10$ . The ability of the system to diffuse away from a reference configuration increases strongly with  $\gamma_{max}$  at  $\gamma_{max} \approx 0.5$ . The transition become sharper as  $N$  is increased.

## 4.4 Results from the TM model

The TM model presented in section 4.2 drops even more features of the LJ system with respect to the NK model: inherent configurations are not anymore associated to an energy, and there is no notion of topology and distance between them. The model consists of a highly stylized representation which mimics the evolution of inherent structures under oscillatory athermal deformation. In a nutshell, the model takes care of labeling all the inherent structures in a fictitious landscape at  $\gamma = 0$  and determines a plausible form of the map  $P$  that associates each inherent configuration with its image through a full deformation cycle (see discussion in section 4.2). Clearly, there is no possibility to straightforwardly<sup>10</sup> extract quantities like  $\tilde{\gamma}_{acc}$  and a diffusion constant within such a model. The information contained in  $P$  can be used to distinguish states that are absorbing or mapping to absorbing states from those that are recurring or mapping to recurring ones (see the definitions given in subsection 4.2.1). This information, in turn, can be used to gather information about the dynamics under AQS deformation: if absorbing states dominate, systems are likely to be trapped into them, similarly to what is observed in the LJ and NK models below  $\gamma_c$ ; if recurring states dominate, systems have the capability of exploring the configuration space before returning to the same state point, analogously to what happens in the other models above  $\gamma_c$ .

### 4.4.1 “Diffusion” behavior: absorbing and recurring states

The naive way to determine which structures behave how under oscillatory deformation is to apply  $P$  repeatedly to each of them. After some applications of  $P$ , the structures will transform into states of the kind  $\mathbf{R}_{abs}$  such that  $P\mathbf{R}_{abs} = \mathbf{R}_{abs}$  (absorbing), or states of the kind  $\mathbf{R}_{rec}$  such that  $P^L\mathbf{R}_{rec} = \mathbf{R}_{rec}$  (recurring). This procedure is however too expensive, because one needs to calculate the trajectory of each and every of the  $M$  structures by means of matrix multiplication. A way to overcome this is treating  $P$  as an adjacency matrix, and constructing the directed graph<sup>11</sup>  $G$  associated to it (see Figure 4.9).  $G$  will be a directed graph whose outdegree is 1, as each structure maps onto one and only one configuration through  $P$ . In general,  $G$  will possess several connected components<sup>12</sup>. Each of these either contains a self-loop or not. Connected components containing a self-loop are those that contain an absorbing state, which is the very node that is connected to itself via the self-loop. All the other nodes are connected to it, and thus represent states mapping to the absorbing state. Connected components not containing self-loops must contain a loop, and their nodes thus represent recurring states or states mapping to recurring states. By examining the graphs one can count

<sup>10</sup>However, the TM model offers the possibility to extract a “relaxation strain” by looking at the average number of cycles  $\tilde{L}$  needed to the system to relax to an absorbing or recurring state (see discussion in subsection 4.2.1). However, this possibility hasn’t been explored in this work.

<sup>11</sup>A useful reference for the terminology of graph theory used in this paragraph is [35].

<sup>12</sup>Using the terminology of graph theory,  $G$  is a *directed 1-forest* or a *functional graph* and its connected components are called 1-trees [35].

the number of  $R$  of recurring (and mapping to recurring) states simply by counting the number of nodes of the connected components of  $G$  which do not possess self-loops. The number of absorbing (and mapping to absorbing) states will be given by  $M - R$ .

We obtain  $P$  with the procedure described in Appendix D, using Python and the support for sparse matrices within the library SciPy [82]. We then extract  $G$  and its connected components using NetworkX [83]. The connected components associated to recurring states can be easily filtered because they don't contain self-loops. We do so for matrices  $P$  with  $M = 10^4$ ,  $10^5$  and  $10^6$ , setting (tentatively) the probability for an inherent structure to be destabilized per unit strain to  $\tau = 0.04$  and plot the average fraction of recurring (or mapping to recurring) states as a function of the  $\gamma_{max}$  averaging on  $\approx 800, 200, 50$  matrices respectively. The result is shown in Figure 4.10.

The curves in Figure 4.10 can be modeled by the fitting function:

$$f(x) = \frac{b}{1 + \left(\frac{\gamma_c}{\gamma_{max}}\right)^a} \quad (4.9)$$

Data in Figure 4.10 and the form of Equation 4.9 show that the TM model shows a sharp increase in the number of states mapping to non-absorbing states as the “oscillation amplitude” is increased beyond some value  $\gamma_c$ , similarly to what has been observed in the case of LJ mixtures and of the NK model above. For this reason, one can reasonably believe that however crude, the TM model encapsulates enough details to describe qualitatively the switch from a “localized” regime (where absorbing states prevail) to a “diffusive” one (where recurring states dominate) observed in particle models. Moreover, the transition is observed to be sharper for higher values of  $M$ , with the parameter  $a$  in Equation 4.9 increasing with increasing  $M$ . Opposite to what is observed in LJ systems, however, the value of  $\gamma_c$  is seen to increase with the system “size”  $M$ .

## 4.5 Summary

In this chapter we have examined the behavior of two kinds of systems.

The first one is the NK model, which was already employed in the past [47] to determine if rejuvenation and overaging are phenomena which take place only in particle systems, or can occur in more general systems when they are cyclically driven in rugged landscapes. The second is a “transition matrix” (TM) model that was specifically designed by us to rationalize the behavior of the dynamics of inherent structures of particle systems under oscillatory athermal deformation.

These systems show a behavior that has interesting similarities and differences with that of particle models studied in chapter 3.

As for the NK model, it exhibits an energy behavior under oscillatory driving that is reminiscent of that observed in the LJ systems of chapter 3. If samples are driven with

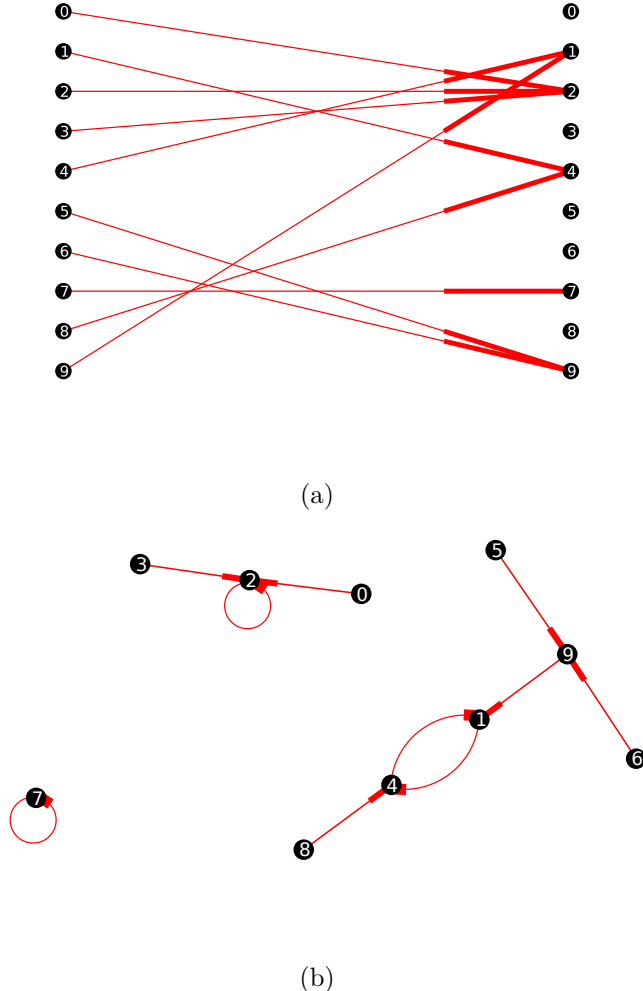


Figure 4.9: (a) The output of the TM model is a map (which depends on  $\gamma_{max}$ ) of the set of inherent structures onto itself. The same map can be interpreted as an adjacency matrix for a directed graph. (b) The resulting graph is a collection of 1-trees [35]. Each of these 1-trees can contain a self-loop or not. If it does, then the vertex with the self-loop represents an absorbing state, and all the vertices in the 1-tree to which it belongs represent states mapping to that absorbing state via AQS dynamics. If the 1-tree does not contain self-loops, then its vertices are associated either to recurring states or states that map onto recurring states in the AQS dynamics. By counting the number of vertices in the two kinds of 1-trees (those with self-loops and those without), one can thus determine the fraction of states that are absorbing (and mapping to absorbing) or recurring (and mapping to recurring).

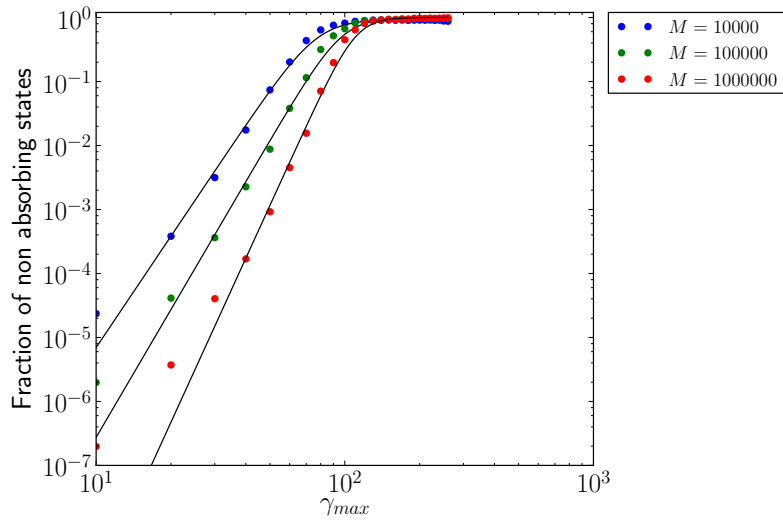


Figure 4.10: Overall fraction of recurring states and mapping to recurring states as a function of  $\gamma_{max}$  for different values of  $M$ , obtained by analysis of the graphs associated to the transition matrices  $P$  generated by the TM model. The number of recurring states increases strongly after some value  $\gamma_c$  which increases as  $M$  increases. The data can be described fairly well with the model in Equation 4.9 (black curves), with a sharpness (dictated by the parameter  $a$ ) which increases for larger  $M$ .

an amplitude  $\gamma_{max}$  above some threshold driving amplitude  $\gamma_c$ , the energy curves as a function of the accumulated “strain”  $\gamma_{acc}$  do converge to a common value, regardless the initial value of the effective temperature (Figure 4.6). This doesn’t happen below  $\gamma_c$ , as systems with different effective  $T$  do reach different plateau values of the energy  $E$  when they are driven at the same  $\gamma_{max}$ . However, we couldn’t devise a way to describe  $E$  as a function of  $\gamma_{acc}$ . In addition, the cumulative  $\gamma_{acc}$  needed to reach the plateau doesn’t seem to increase in correspondence of any value of  $\gamma_{max}$ , as opposed to what is observed in the LJ models.

As for the dynamics in configuration space, the NK model exhibits another important distinctive feature: it shows no hint of diffusion, as configurations seem to reach and maintain a steady average distance from a reference configuration as  $\gamma_{acc}$  is increased (Figure 4.7). However, such distance increases with  $\gamma_{max}$ , and when plotted against  $\gamma_{max}$  it shows a sigmoidal trend which increases at a value  $\gamma_c$ , with a sharpness depending on  $N$  (Figure 4.8). We thus posit that a transition at a value  $\gamma_c$  holds for the NK model, even though our data are too scarce to model it. Our values of  $N$  are quite small with respect to  $K$ , so our samples are possibly affected by important size effects. It would be interesting to study larger samples and do a proper analysis of size effects. Unfortunately, a study of the NK model becomes quickly prohibitive for large  $N$ . A possible solution would be parallelizing the NK code so to allow it to split the minimization procedure onto several processors, but such a scheme has not been implemented in this thesis.

We used the TM model to compute the fraction of states that map (via AQS dynamics)

to recurring states as a function of  $\gamma_{max}$ . Recurring states are expected to represent the diffusive states encountered in the LJ model, at least in the limit in which the number of inherent structures  $M$  is large. Indeed the fraction of recurring states and states mapping to recurring states grows with  $\gamma_{max}$  (see Figure 4.10) and it is well fitted by Equation 4.9. Such fraction of recurring states is related to the observations of diffusion in the LJ model, but can't directly be compared with it, because there is no notion of spatial distance in the TM model. However, such result is in qualitative agreement with what is observed in both the NK and LJ models, showing that the TM model is able to qualitatively capture their behavior.

# 5 Memory effects

Within the LJ, NK and TM models one has the possibility of selecting an initial sample and to apply athermal oscillatory driving of a given amplitude  $\gamma_{max}$  to it. As seen in chapter 3 and chapter 4, if the amplitude is small enough, samples get stuck into absorbing states that are left unchanged by further oscillations. In this chapter we show that information about the oscillation amplitude is encoded in samples that have reached such absorbing states. This information can be *read* from them through a simple procedure, similarly to what can be performed with noncolloidal suspensions. Interestingly, by changing the deformation protocol and alternating oscillations of different amplitudes, we show that samples reach states that encode information about the multiple applied amplitudes. The main findings presented in this chapter have been published in [84].

## 5.1 Memory effects in binary LJ mixtures, NK and TM models

The existence of a transition at  $\gamma_c$  for the LJ, NK and TM models implies the existence of absorbing states, i.e. states that are unperturbed when driven by some amplitude  $\gamma_1 < \gamma_c$ . These states and the associated transition are reminiscent of those observed in the models of noncolloidal suspensions in [55]. These suspensions, in turn, are known to be able to retain memory of their mechanical history [58]. In particular, if samples are deformed with a series of shear oscillations of amplitude  $\gamma_1$ , such amplitude can be read by performing an additional deformation cycle on the samples, and measure if the samples are perturbed by such deformation. The similarity of the behavior under deformation of our LJ and NK models with that of noncolloidal suspensions in [55] suggests that memory effects can be also observed in the former classes of systems, by following the very same protocol above. In what follows we explore this possibility, and verify that it can indeed be realized.

### 5.1.1 Training and reading protocols: single memory

To start with, let's consider a sample of LJ particles like those examined in chapter 2. By applying a sufficiently large number of cycles of oscillatory deformation of amplitude  $\gamma_1 < \gamma_c$  to it, the sample reaches an absorbing state. This means that further oscillations leave it unaffected. Would it be possible for an experimenter to measure (read) the value of  $\gamma_1$  if it is not known beforehand? A possible strategy is to take a copy of the sample and perform a single cycle of amplitude  $\gamma_r$ , and repeat the operation with other copies and different values of  $\gamma_r$ . One can be sure that for  $\gamma_r = \gamma_1$  a cycle won't alter the sample, because it is an absorbing state for that amplitude. Thus one can measure  $\gamma_1$  by finding the value of  $\gamma_{max}$  that does not alter the sample. This can obviously be done if no other value  $\gamma$  has the same property. We show below that this indeed the case for LJ systems, and that this feature holds for the NK model as well.

#### Single memory in the LJ model

In the LJ case, we take inherent structures of KA with  $N = 4000$  and effective  $T = 0.466$  and subject them to a series of  $N_{cyc}$  full oscillations of amplitude  $\gamma_1$ , so that the value of the accumulated strain is  $\gamma_{acc} = 4\gamma_1 N_{cyc}$ . We will refer below to this procedure as the *traning* phase. After the training, identical copies of the samples are subject to a single cycle of a variable amplitude  $\gamma_r$ . During this step, called the *reading* phase, changes of the samples are monitored.

In the LJ case, we set  $\gamma_1 = 0.06$  and look at the MSD between the configurations before and after the read for different durations of the training  $\gamma_{acc}$ . A plot of the MSD measured during reading cycles is shown in Figure 5.1 as a function of the reading amplitude  $\gamma_r$ .

The behavior in Figure 5.1 depends on  $\gamma_{acc}$ :

- For no training at all ( $\gamma_{acc} = 0$ ), the MSD grows smoothly as  $\gamma_r$  is increased. This is because a larger  $\gamma_r$  is related to a larger capability to move away from the initial unstrained configuration (in the language of the mortal random walk in subsection 3.3.3, a larger  $\gamma_r$  corresponds to a larger  $D$  in Equation 3.6).
- For larger values of the training  $\gamma_{acc}$  the MSD is lower, and develops a kink in correspondence to a value of  $\gamma_r = \gamma_1$ .
- For very large values of  $\gamma_{acc}$  the MSD plot becomes independent from  $\gamma_{acc}$ , with a deep dip at  $\gamma_1$ . The independence from  $\gamma_{acc}$  is a consequence of the fact that in this case all the samples reach absorbing states, so that a prolongation of the training has no effect on them. In this case the MSD shown in Equation 3.6 is zero in correspondence of  $\gamma_1$  (as it should, because states are absorbing), but has a non-zero value for all the other values of  $\gamma_r$ . This allows us to conclude that,

### 5.1. Memory effects in binary LJ mixtures, NK and TM models

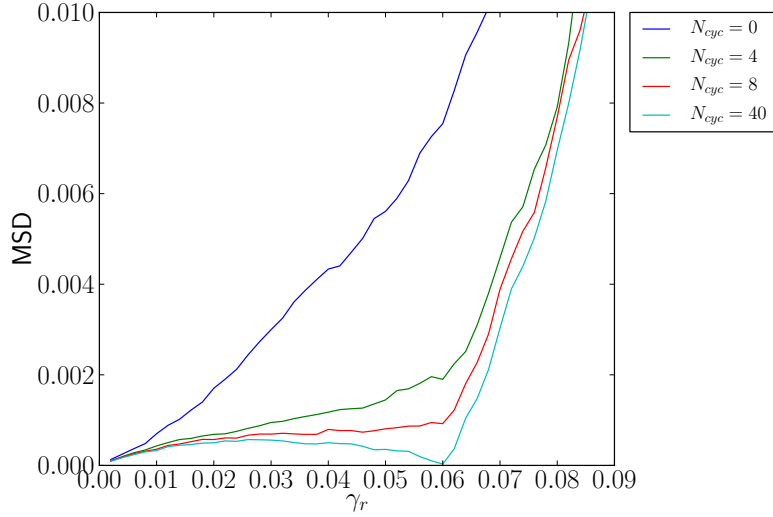


Figure 5.1: Mean squared displacement between configurations before and after a full deformation cycle of amplitude  $\gamma_r$ , for a different number of training cycles of amplitude  $\gamma_1 = 0.06$ , as a function of  $\gamma_r$ . Data are relative to initially undeformed KA samples with  $N = 4000$  and whose effective temperature is  $T = 0.466$ . It's clear how trainings of increasing length produce samples that show a memory of the training amplitude.

in general, *an absorbing state for an oscillation amplitude  $\gamma_1$  is not an absorbing state for a  $\gamma_r \neq \gamma_1$ .*

These facts clearly show that one can recover the value of the training  $\gamma_1$  from trained samples simply by performing reading cycles on them, and looking for kinks in the  $\text{MSD}(\gamma_r)$  plot.

The non-zero MSD for any value of  $\gamma_r$  but  $\gamma_1$  in the reading phase has a more subtle implication: the state reached after the reading cycle of amplitude  $\gamma_r$  does not coincide with the initial one, and this new state doesn't need to be an absorbing state for  $\gamma_1$ . In other words this new state won't necessarily give a zero MSD if re-read at an amplitude  $\gamma_1$ , meaning that memory of the training at  $\gamma_1$  has been erased. Summarizing, *a single cycle of an amplitude which does not coincide with the training amplitude is able to make the system “forget” about the training*. Thus, the reading of memory is an operation that destructs the memory.

How does the mechanism of memory erasure in the LJ model work? The answer to this question is rooted in the nature of the absorbing states, and is related to another question: how does an absorbing state actually manage to retain the same state when read with a cycle whose amplitude is equal to its training amplitude ( $\gamma_r = \gamma_1$ )? By monitoring the behavior of an absorbing configuration during a reading cycle we notice that an absorbing cycle undergoes several transitions (in the sense defined in subsec-

tion 2.3.2). This is evident, for instance, by looking at the evolution of the positions of the particles in the configuration in space or by monitoring the potential energy  $U$  as the strain  $\gamma$  is cycled during the reading phase. An animation of the evolution of the positions of the particles can be found online on [85] (see Appendix F for instructions), whereas plots of  $U$  during the reading cycle are displayed in Figure 5.2. By looking at the evolution of the system in real space and the behavior of  $U$  during a reading cycle, one sees that at some values of the strain the sample undergoes abrupt rearrangements, and that to these correspond discontinuities in the energy. At the end of the full cycle, somewhat surprisingly, the sample returns back to its original state. This is because *the sequence of transitions constitutes a chain of rearrangements that is able to revert the sample to its original state*. It is clear that if such a sequence is altered, for instance by changing the value of the amplitude, the sample is not anymore guaranteed to return to its original state. This is the reason why one gets a non-zero average MSD in Figure 5.1) for  $\gamma_r \neq \gamma_1$ . The consequence of this is that the sample is actually kicked out of the absorbing configuration, and thus loses memory of its training.

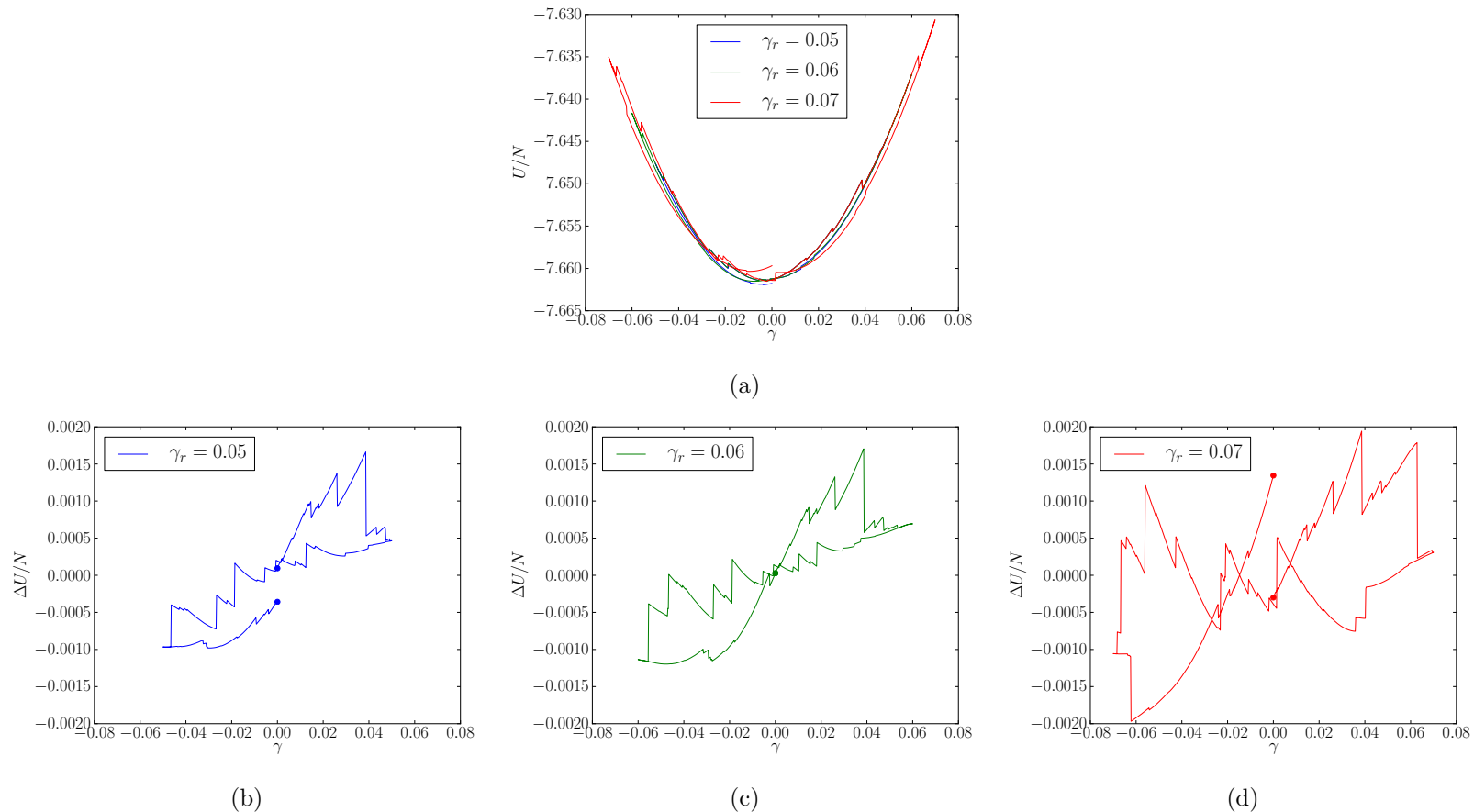


Figure 5.2: Energy per particle as a function of the strain  $\gamma$  for a sample of  $N = 4000$  trained at  $\gamma_1 = 0.06$  and performing a single cycle of amplitude  $\gamma_r = 0.05, 0.06, 0.07$  (in blue, green, red respectively). In (a), all the curves overlap and can be approximated by a quadratic function. In (b), (c), (d), the quadratic background is subtracted. The initial sample is in an absorbing state for amplitudes of  $\gamma_{max} = 0.06$ , so in (c) the endpoints of the curve meet at  $\gamma = 0$ . This is not the case for (b) and (d), where cycles of amplitudes  $\gamma_r = 0.05$  and  $0.07$  respectively are performed.

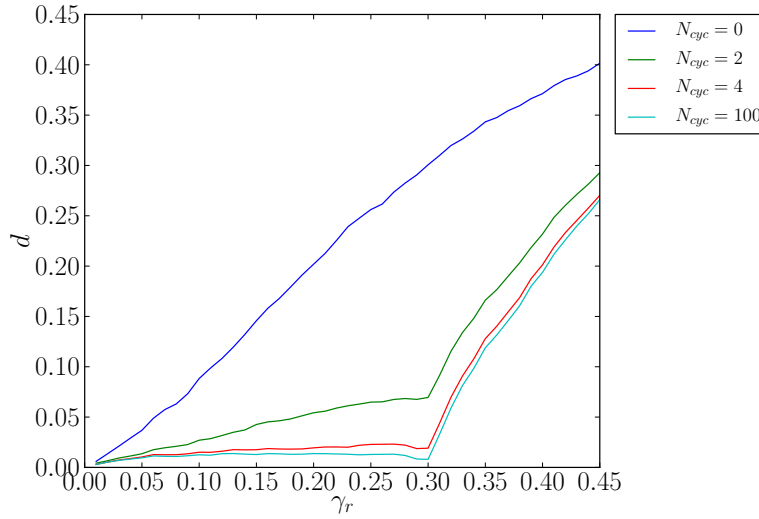


Figure 5.3: Hamming distance between configurations before and after a full deformation cycle of amplitude  $\gamma_r$ , for a different number of training cycles of amplitude  $\gamma_1 = 0.3$ , as a function of  $\gamma_r$ . Data are relative to initially undeformed NK samples with  $N = 20$  and whose effective temperature is  $T = 1.0$ . It's clear how trainings of increasing length yield samples that show a memory of the training amplitude.

### Single memory in the NK model

We perform a training and reading on NK configurations as well, in a way that mirrors that followed in the LJ case. We choose  $N = 20$ ,  $K = 10$ , averaging on  $\approx 8$  inherent configurations for  $\approx 200$  instances of the couplings  $a$ ,  $b$  and  $J$ , setting  $\gamma_1 = 0.3$  and performing trainings of different durations. The measure of the displacement in the reading phase is given by the Hamming distance in Equation 4.8 between the configuration before and after the read. Results are plotted in Figure 5.3, and are in qualitative agreement with what is observed in the LJ case: the possibility to encode, read and erase memory thus exists in the NK model as well.

### Single memory in the TM model

One can probe for memory effects in the TM model, but the procedure is fairly different with respect to that followed in the LJ and NK cases. First of all, to do so we generate  $P$  matrices for different values of  $\gamma_{max}$ , following the procedure described in Appendix D. Once a  $\gamma_1$  is chosen, we consider the configurations trained by  $N_{cyc}$  oscillations (equivalent to  $\gamma_{acc} = 4\gamma_1 N_{cyc}$ ). These are those with the same index of the non-empty rows of the matrix  $P_{\gamma_1}^{N_{cyc}}$ , where  $P_{\gamma_1}$  is the matrix associated to the deformation up to  $\gamma_1$ . This is because  $P_{\gamma_1}^{N_{cyc}}$  is the matrix that maps any of the states of the undeformed landscape into those that are reached by them after  $N_{cyc}$  oscillations. We call to the set of such states  $A_{N_{cyc}}$ . To probe the behavior of such states under a single reading cycle of

### 5.1. Memory effects in binary LJ mixtures, NK and TM models

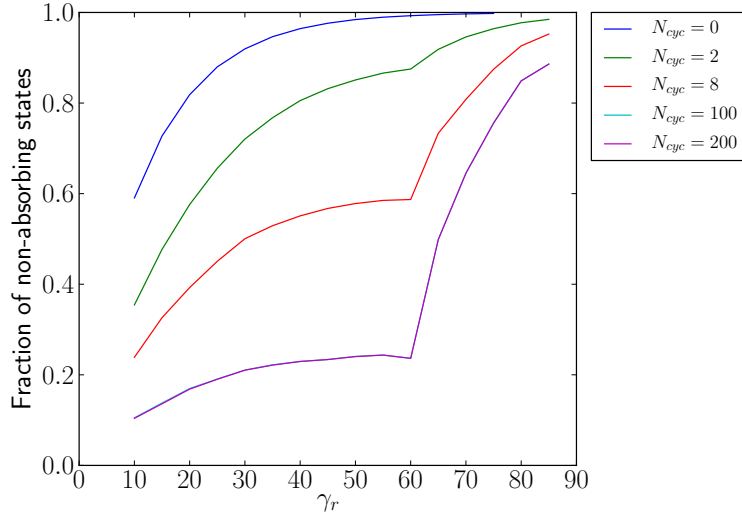


Figure 5.4: Fraction of inherent states that are not invariant under the application of a  $P_{\gamma_r}$ , starting from a pool of states trained by a different number of applications of the matrix  $P_{\gamma_1}$  with  $\gamma_1 = 60$ , as a function of  $\gamma_r$ . Data are obtained within the TM model setting  $M = 10000$ . It's clear how trainings of increasing length yield samples that show a memory of the training amplitude.

amplitude  $\gamma_r$ , we check whether they are absorbing cycles for  $\gamma_r$ , i.e. we verify if the condition  $P_{\gamma_r}\mathbf{R} = \mathbf{R}$  is satisfied, for each  $\mathbf{R}$  state in  $A_{N_{cyc}}$ . The validity of this condition is easy to check, because it holds true if and only if the matrix element on the diagonal of  $P_{\gamma_r}$  corresponding to such states is equal to one. In Figure 5.4 we plot the fraction of non-absorbing states (i.e.  $\mathbf{R}$  states in  $A_{N_{cyc}}$  that don't meet the condition  $P_{\gamma_r}\mathbf{R} = \mathbf{R}$ ) for different values of  $\gamma_r$ , obtained by studying the states belonging to a space with  $M = 10000$  structures with probability  $\tau = 0.04$  to be destabilized and “trained” by a different number of cycles of amplitude  $\gamma_1 = 60$ .

Strictly speaking, the plot in Figure 5.4 is not equivalent to those in Figure 5.1 and Figure 5.3. In the LJ and NK models a notion of distance exists between configurations, so that one is able to quantify the displacement experienced by the samples during the reading phase (using the MSD and the Hamming distance respectively). Such information is not given by the TM model, which however delivers a very similar information: it tells whether states are left unchanged or are modified by a reading cycle of amplitude  $\gamma_r$ <sup>1</sup>.

<sup>1</sup>In this sense, the TM model gives a “yes or no” information about whether a sample is changed by a reading cycle; the LJ and NK models do more: they give a measure of *how much* a sample is affected by a reading cycle.

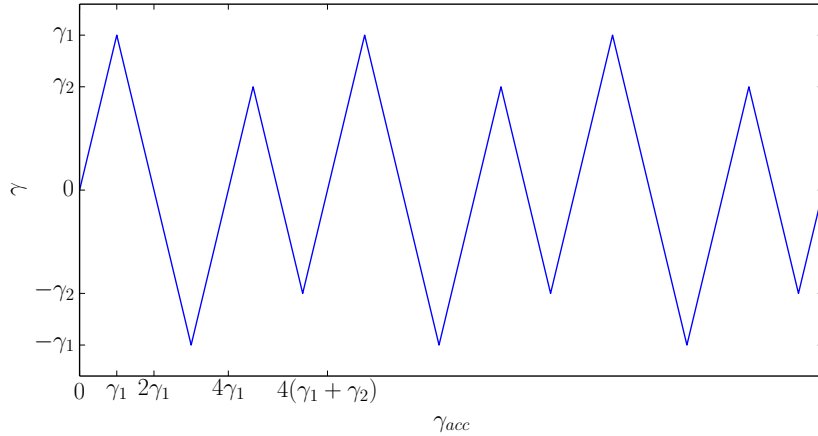


Figure 5.5: Strain profile applied to a sample to encode a double memory.

### 5.1.2 Multiple memories

The training can be modified so that it consists in the alternated repetition of cycles of amplitude  $\gamma_1$  and  $\gamma_2$ , like in Figure 5.5. The rationale behind this protocol is to encode *multiple* memories in our samples, and be able to read the values of the different training amplitudes in the reading phase. The cycles in  $\gamma$  have the form  $0 \rightarrow \gamma_1 \rightarrow 0 \rightarrow -\gamma_1 \rightarrow 0 \rightarrow \gamma_2 \rightarrow 0 \rightarrow -\gamma_2 \rightarrow 0$ . We repeat such cycle  $N_{cyc}$  times, so that after the training the sample has been subjected to an accumulated strain  $\gamma_{acc} = 4(\gamma_1 + \gamma_2)N_{cyc}$ . This can be straightforwardly done in the LJ and NK cases, whereas (as described above in the case of single memory), a different scheme must be adopted with the TM model.

For what concerns the LJ model, we choose  $\gamma_1 = 0.06$  and  $\gamma_2 = 0.04$  and train samples of the same size and initial effective temperature as those trained with a single amplitude by performing  $N_{cyc}$  on them. We then take copies of the trained samples and subject them to a reading cycle of amplitude  $\gamma_r$ . As above we measure the MSD of the configurations as a function of  $\gamma_r$ . As it can be seen from Figure 5.6, the MSD has two kinks in correspondence of  $\gamma_1$  and  $\gamma_2$ , which are both visible for sufficiently high  $N_{cyc}$ . In addition, for a high number of  $N_{cyc}$ , the MSD curve converges to a curve showing clearly the trace of the two training amplitudes. By looking at the data, it's reasonable to assume that this will be true for an arbitrarily large number of  $N_{cyc}$ , so that the two memories will be *persistent* for  $\gamma_{acc} \rightarrow \infty$ .

In the NK case, we choose  $\gamma_1 = 0.06$  and  $\gamma_2 = 0.04$  and train the samples for different  $N_{cyc}$  with the same  $N, K$ , initial effective temperature and values of the couplings of those trained with a single amplitude. Again, we use the Hamming distance  $d$  as a measure of the change in configurations in the reading phase and plot  $d$  for different values of  $\gamma_r$  in Figure 5.7. As in the LJ case, the training amplitudes can be read by looking at kinks (discontinuities in the first derivative) in the plot, and again they appear persistent in the limit  $\gamma_{acc} \rightarrow \infty$ .

### 5.1. Memory effects in binary LJ mixtures, NK and TM models

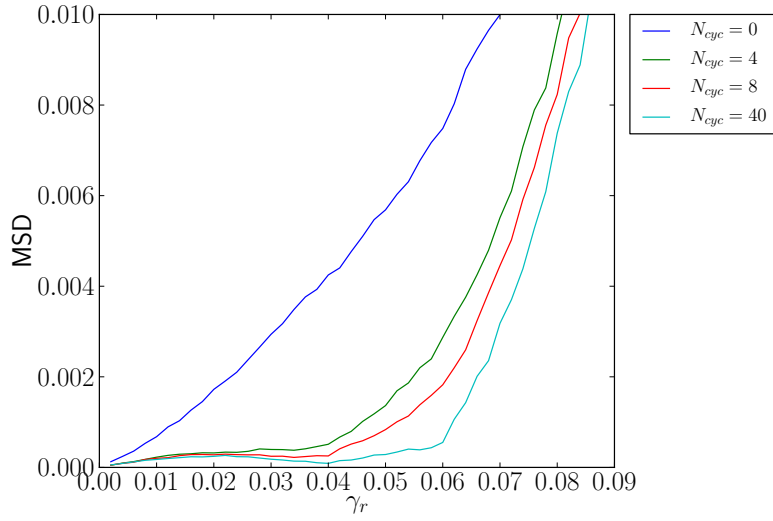


Figure 5.6: Mean squared displacement between configurations before and after a full deformation cycle of amplitude  $\gamma_r$ , for a different number of training cycles alternating training amplitudes  $\gamma_1 = 0.06$  and  $\gamma_1 = 0.04$ , as a function of  $\gamma_r$ . Data are relative to initially undeformed KA samples with  $N = 4000$  and whose effective temperature is  $T = 0.466$ . In the case of the longest trainings samples show a memory of both the training amplitudes.

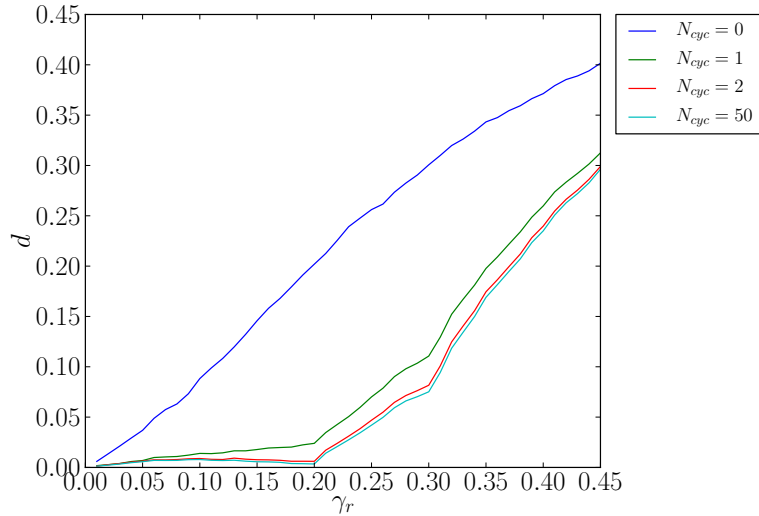


Figure 5.7: Hamming distance between between configurations before and after a full deformation cycle of amplitude  $\gamma_r$ , for a different number of training cycles alternating training amplitudes  $\gamma_1 = 0.3$  and  $\gamma_1 = 0.2$ , as a function of  $\gamma_r$ . Data are relative to initially undeformed NK samples with  $N = 20$  and whose effective temperature is  $T = 1.0$ . In the case of the longest trainings samples show a memory of both the training amplitudes.

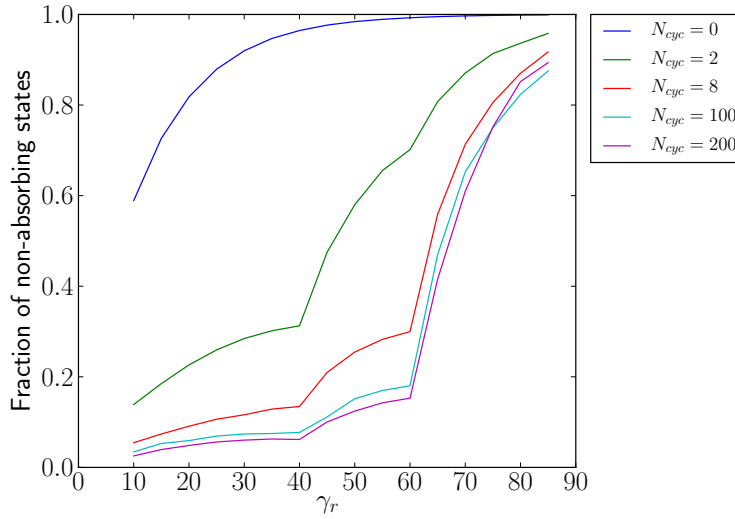


Figure 5.8: Fraction of inherent states that are not invariant under the application of a  $P_{\gamma_r}$ , starting from a pool of states trained by a different number of applications of the matrix  $P_{\gamma_1}$  with  $\gamma_1 = 60$  and of  $P_{\gamma_2}$  with  $\gamma_2 = 40$ , as a function of  $\gamma_r$ . Data are obtained within the TM model setting  $M = 10000$ . It's clear how trainings of increasing  $N_{cyc}$  produce samples that show a memory of the training amplitudes.

In the case of the TM model the “trained” configurations are those with the same index of the non-empty rows of the matrix  $(P_{\gamma_2} P_{\gamma_1})^{N_{cyc}}$ , where  $P_{\gamma_1}$  and  $P_{\gamma_2}$  are the matrices associated to the deformation up to  $\gamma_1$  and  $\gamma_2$ . We refer to the set of such states as  $B_{N_{cyc}}$ . Exactly as in the reading of single memories, we compute the fraction of non-absorbing states (i.e. states in  $B_{N_{cyc}}$  that don't meet the condition  $P_{\gamma_r} \mathbf{R} = \mathbf{R}$ ) for different values of  $\gamma_r$  as a function of  $\gamma_{max}$ . From the analysis of Figure 5.8, it is clear that a double memory can be encoded in an ensemble of structures in the TM model.

### 5.1.3 Summary and comparison with colloidal suspensions

In this chapter we have verified that it is indeed possible to encode in our systems single and double memories using the same protocol adopted in [58] in the case of noncolloidal suspensions. In fact, this can be achieved by training our samples with shear deformation cycles of a given amplitude and by deforming them alternating two different oscillation amplitudes respectively. This is evident, for instance, from the analysis of Figure 5.1 and Figure 5.6.

However, we found that LJ and NK models show an important difference with the memory behavior of noncolloidal suspensions. In these two classes of systems absorbing states for a given amplitude can be destabilized by shear deformation cycles of a lesser amplitude. This fact is related to the nature of absorbing states in the LJ and NK models. An absorbing state is such because during a deformation cycle of amplitude  $\gamma_1$  the system undergoes various rearrangements during a cycle, and the full sequence of

### **5.1. Memory effects in binary LJ mixtures, NK and TM models**

---

them has the effect of bringing the system to the state occupied before the application of the deformation cycle (Figure 5.2). If the deformation amplitude is changed, such sequence of rearrangements is altered, and the system can fail to come back to its initial state. We showed that this fact has the consequence that multiple memories can stay encoded in LJ and NK systems even if these are subjected to indefinitely long series of training cycles. This is because in long trainings different training amplitudes “compete” with the each other. In particular, the action of small amplitudes is that of partially erasing the effect of larger amplitudes, so that samples never get “completely trained” and no amplitude takes over the others. As it can be checked by comparing Figure 5.1 and Figure 5.6 with Figure 1.15, this is different from what happens in noncolloidal suspensions without noise, and mirrors what is observed in models of the same suspensions when noise is added [58]. The effect of memory erasure due to reading at an amplitude other than the training one makes reading a *destructive* operation. However, it is possible to devise a protocol that can overcome the erasure of memory due to the reading operation in our systems: given an ensemble of systems trained in the same way, one can read the information encoded in them by performing on each of the samples a single deformation cycle, with a reading amplitude which is different for each system. Such reading operation is destructive at the level of the memory in a single sample, but allows to retrieve the desired information from the ensemble. Once that the information has been obtained, all the samples of the ensemble can be “retrained” using such information, so to restore in them the original information.

We surmise that the observations in this chapter hold true for LJ and NK systems with much larger  $N$ . We expect this because the transition at  $\gamma_c$  in chapter 3 is likely to exist in the thermodynamic limit, as well as the mechanism of destabilization of absorbing states as the amplitude of deformation is changed.

Furthermore, the observation of single and double memories in the TM model strengthens the idea that memory phenomena are indeed a general feature of the athermal dynamics of oscillatory deformed LJ and NK systems.



## 6 Conclusions and Perspectives

In this chapter we summarize the fundamental results of this thesis. They consist in: 1) a rationalization of the observations of overaging and rejuvenation in the cyclic shear simulations reported in [45]; 2) the analogy drawn between the behavior of our model glass and that of the sheared suspensions in [55], with the existence of a transition in the dynamics of our systems, for some value of the shear amplitude  $\gamma_c$ ; 3) the existence of memory effects in our model glass, comparable to those observed in sheared suspensions in [58]; 4) the observation of a behavior that qualitatively resembles that of our model glass in the NK and TM models.

In what follows, we also draw connections with current research work related to ours, and describe promising future developments.

In the previous chapters we have studied the effect of oscillatory shear deformation on a binary mixture of Lennard-Jones particles, which we have taken as a model for metallic glasses under cyclic load.

By doing so, we have extended the analysis carried out on the very same system by Lacks and Osborne in [45], which reported a variation of the potential energy of their samples as a consequence of a *single shear deformation semicycle*. What was known from [45] was that a single semicycle of deformation is able to overage or rejuvenate the sample depending on its initial effective temperature and on the amplitude of the deformation. Furthermore, they reported that one deformation semicycle changes samples so that they appear as having a lower or higher effective temperature (respectively in the case of overaging and rejuvenation) if one measures their energy after the deformation. However, they noted that if one measures another quantity, e.g. their stress tensor, undeformed and deformed samples are clearly distinguishable, even if they have the same potential energy.

What we have performed here is an analysis similar to that in [45], but applying a large number of full shear deformation cycles. For small deformation amplitudes, samples tend more frequently to lower their energy and overage, coherently with what is re-

## Chapter 6. Conclusions and Perspectives

---

ported in [45]. After a sufficiently large number of cycles, however, samples do assume absorbing states that are unchanged upon further cycles of the same amplitude. Observations of overaging in [45] can thus be considered as the initial steps towards the absorbing states encountered by us. The energy of such absorbing states depends on the initial effective temperature, so that the deformation is not able to make samples lose completely the memory of their original configuration. In addition, these absorbing states have a very low residual stress, comparable to that of undeformed structures. In this case it's thus hard to distinguish deformed absorbing states and undeformed states with the same potential energy. For larger amplitudes, systems are brought by deformation to states characterized by a potential energy and residual stress that depend on the amplitude  $\gamma_{max}$  but not on the original state of the system. This is a feature that is observed only in the case of several oscillations, and was thus outside of the reach of the simulations in [45]. A large number of shear strain cycles of sufficiently large amplitude is thus able to make systems forget about their original configuration. These states have a large residual stress, and thus can be easily distinguished from undeformed ones with the same potential energy.

From these observations, we conclude that there must be a threshold value of the strain amplitude  $\gamma_{max}$  that determines whether a sample will lose memory of its initial configuration or not. Incidentally, the accumulated strain  $\tilde{\gamma}_{acc}$  needed to the energy to assume a fixed value for low oscillation amplitudes and that needed to reach a steady value of the energy for large amplitudes become very large at the separation between the two regimes. This is the hint of the existence of a transition, which could not be observed in [45] and is qualitatively similar to what has been observed by members of the Pine group [55] in models of suspensions.

Our results confirm that there is indeed an analogy between the behavior of the dilute suspensions in [55] and the one we observe in our model glass. In fact, by studying the diffusion of the particles in our system, we have identified two regimes, that are associated to the energy behavior and the memory of the initial conditions discussed above. For deformation amplitudes below some value  $\gamma_c$ , the systems rearrange until particles stop diffusing. This happens because diffusion makes systems explore the space of configurations until they find absorbing states which are stable under the application of a deformation cycle. Typically, the systems fall into absorbing states before having moved far away from their initial configurations, and so their initial states and the final absorbing ones are correlated. In this low-amplitude regime one can approximate the motion of the system in configuration space as a continuous time<sup>1</sup> random walk with a finite probability of being interrupted (which we named “mortal” in agreement with the language used in [80]). This behavior is similar to what is observed in the suspensions in [55]. We emphasize, however, that absorbing states in our LJ systems and particle suspensions have a different nature. In [55] absorbing states are configurations where no interactions between the particles happen in the course of the deformation. In our particle model, instead, an absorbing state undergoes several rearrangements during the

---

<sup>1</sup>In our case, however, it is the accumulated strain  $\gamma_{acc}$  that plays the role of time.

---

deformation cycle. Such rearrangements “conspire” to bring the system back to the initial configuration after a full cycle has been performed, so that exactly the same sequence of transitions takes place over and over again if the sample is subjected to further cycles of the same amplitude. Incidentally, an analysis of the stress-strain curves in this regime reveals that the hysteresis curves are very narrow. The energy dissipation due to the rearrangements mentioned above is thus very small.

For amplitudes larger than some value  $\gamma_c$ , the systems don’t seem able to find absorbing states in the course of their exploration of the space of configurations, so that particle motion doesn’t come to a halt. For the largest system size that we dealt with ( $N = 32000$ ) the motion of the particles is heterogeneous, with particles that move the most organizing in bands within the simulation box. To our knowledge, this is the first observation of the formation of such shear bands in simulations of oscillatory shear in Lennard-Jones systems employing Lees-Edwards boundary conditions. In addition, the motion of the system in this regime is dissipative and characterized by large hysteresis curves in the stress-strain plot. The value of  $\gamma_c$  doesn’t seem to be closely related to value of yield strain of our samples. Even without looking at the results in detail, this is easy to rationalize. The value of  $\gamma_c$  is related the properties of deformed samples, and can be inferred from the behavior of oscillatory deformed samples that (above  $\gamma_c$ ) have lost memory of their initial condition. There is thus no reason to believe that  $\gamma_c$  should bear any close relation at all with the value of the yield strain, which is a property of *undeformed* samples.

From all of the above it is clear that the system shows a transition from a low-amplitude regime characterized by low dissipation and the reaching of absorbing states which bear memory of the initial conditions, to a high-amplitude regime characterized by dissipation and particle diffusion and loss of memory of the initial configuration (at least for the smallest systems). This is one of the main findings of this thesis.

During the completion of this work, two papers studying systems of particles under oscillatory shear were published by other authors.

In [86], the transition at  $\gamma_c$  from the regime where absorbing states dominate to the one where diffusion dominates is interpreted as a transition to chaos, with systems revisiting states not after just one cycle (as in our absorbing states), but after a small integer number of deformation cycles as the amplitude of the deformation exceeds  $\gamma_c$ . This observation is coherent with our findings and complements them.

In [87], KA mixtures like ours are simulated at *finite temperature*, and the outcome qualitatively agrees with our results: a subdiffusive plateau in the MSD of the particles is in fact observed for small deformation amplitudes, and diffusive behavior is observed for large amplitudes, thus confirming that our athermal protocol is capable of revealing features that are retained at non-zero temperatures.

The fact that both our system and the suspensions in [55] both undergo a dynamic transition at some value  $\gamma_c$  of the oscillation amplitude suggests that the two systems can show other similarities. We indeed verify that our Lennard-Jones system can retain

## Chapter 6. Conclusions and Perspectives

---

a memory of its mechanical history like suspensions studied in [58] do. In particular, if a set of LJ systems is trained with cyclic oscillations of a given amplitude, such an amplitude can be read by performing a single “reading” cycle of various amplitudes. The memory manifests itself as a kink in the MSD of the samples at the end of each reading cycle. Differently from what is observed in the case of suspensions, samples trained with a given amplitude reach states that are absorbing only for cycles whose amplitude coincides exactly with the training amplitude, but are destabilized by cycles of lower or higher amplitude. An indirect consequence of this fact is that it is possible to encode multiple memories in our samples by applying on the sample an arbitrarily long series of training oscillations alternating different amplitudes. This is not possible in the noise-free version of the system in [58], because in that case a long training has the consequence of erasing all but one memory of the training amplitudes. Our system, which is able to exhibit multiple *persistent* memories, is instead equivalent to the system in [58] with added noise.

We expect the results above to extend to more complex systems (for instance constituted by a larger number of components) endowed with more realistic interaction potentials. In addition, our work can be considered as a benchmark for mesoscopic theories of deformation (e.g. the STZ theory). Faithful mesoscopic descriptions should thus aim at reproducing, for instance, the transition behavior described above.

In the previous chapter we have also shown that the behavior observed in oscillatory deformation of our LJ system can be observed in the NK model, a model which has been used in the past [47] to show that rejuvenation and overaging don’t occur only in particle models of glasses. Our results extend the observations on the NK model in [47] in a similar way as we have extended the work on the LJ system in [45]. Our analysis of the NK model demonstrates that a transition and memory phenomena can be observed in presence of a generic deformable landscape. This fact suggests, for instance, that memory effects can be observed in driven systems where the dynamics of the system can be considered athermal and occurring in a deformed landscape. This could be realized, for instance, in the case of frustrated magnets at low temperature in oscillating magnetic fields. Incidentally, the NK model appears to as an ideal playground to test the existence of a mechanism of “period-doubling” for the transition to chaos explored in [86] in athermally deformed energy landscapes.

We have also developed and described in detail the TM model, which is a toy model that aims at modeling in a very simple way the athermal dynamics of the systems above, based on some fairly stringent assumptions on the behavior of the energy landscape under deformation. In spite of its simplicity (and in particular the absence of a notion of distance between the inherent structures) it has proven able to reproduce the existence of some kind of transition at a value  $\gamma_c$  and to show memory effects. The very limited number of ingredients in this model leads us to believe that the phenomenology observed for the LJ and NK systems can be observed in a wide class of systems showing some

---

kind of “symmetry” in their dynamics, which is embodied in the construction on  $P_{\pm}$  matrices in the TM model.



# A Glossary of mechanical terms

Here we list some definitions and concepts related to the terminology used in materials science and employed in chapter 1. A more comprehensive introduction to these terms can be found in [1].

## List of definitions

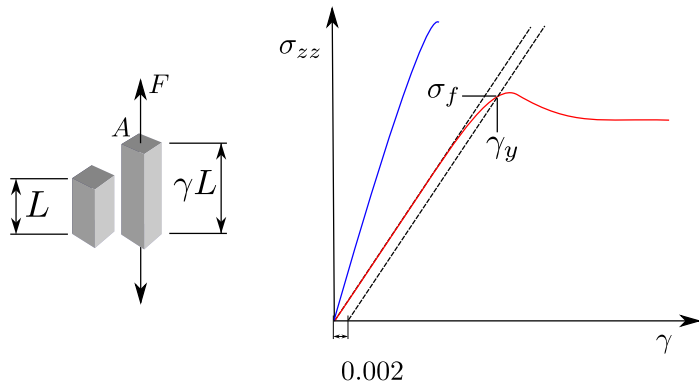


Figure A.1: Schematic of a tensile deformation experiment (left) and two possible forms of stress-strain curves.  $\sigma_{zz}$  is equal to  $F/A$ . The blue curve represents the behavior of a *brittle* sample, i.e. a sample that ruptures soon after that the stress-strain curve has deviated from linearity. The red curve represents the stress-strain curve of a *ductile* sample, i.e. of a sample that can sustain tensile stress for large values of the deformation  $\gamma$ . In particular, the red curve shows *work-softening*, with the sample sustaining less force as it is deformed at large strains. The slope of the dashed lines is the Young modulus  $E$  of the sample associated to the red curve, and can be used to determine the 0.002 yield strain  $\gamma_y$  and the yield stress  $\sigma_f$  via the construction shown in the figure. The yield strain and stress ( $\gamma_y, \sigma_f$ ) are the coordinates of the point where the line of slope  $E$  passing through the point  $(0.002, 0)$  intercepts the stress-strain curve.

## Appendix A. Glossary of mechanical terms

---

For small deformation of a material in a tensile experiment (see Figure A.1) the material behaves *elastically*, i.e.  $\sigma_{xx}$  shows a linear dependence from  $\gamma$ . We define the *Young modulus*  $E$  as

$$E = \frac{\sigma_{zz}}{\gamma} \quad (\text{A.1})$$

where  $\sigma_{zz}$  is the value of stress in the direction of the loading corresponding to a deformation  $\gamma$  measured in the linear part of the stress-strain curve (see Figure A.1).  $E$  is thus the slope of the stress-strain curve in an interval close to the origin.

The *strength*  $\sigma_f$  is defined for metals as the value of the stress at which the stress-strain curve for axial loading (see Figure A.1) deviates by a strain of 0.002 from the linear elastic line.

The *yield strain*  $\gamma_y$  is the value of strain at which the stress-strain curve assumes the value  $\sigma_f$  (see Figure A.1). It is thus the value of the strain at which the sample ceases to be linearly elastic upon axial loading, where the exact definition of “ceasing to be elastic” depends on the definition of  $\sigma_f$ .

The *hardness*  $H$  is the quantity measured by pressing a pyramid-shaped indenter onto the surface of a material and is expressed by the formula

$$H = \frac{P}{A} \quad (\text{A.2})$$

where  $P$  is the load (force) applied on the indenter and  $A$  is the area of the base of the pyramid-shaped indent caused on the surface (see Figure A.2). Hardness is related to strength  $\sigma_f$  by the approximate relationship  $H = 3\sigma_f$ .

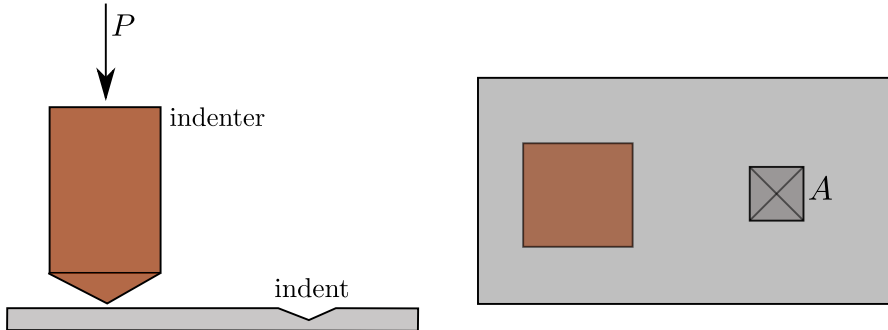


Figure A.2: Schematic side (left) and top (right) view of an indentation experiment to obtain the hardness of a material.

The *resilience* is the area under the stress-strain curve up to  $\gamma = \gamma_y$  (see Figure A.3):

$$\text{resilience} = \int_0^{\gamma_y} \sigma_{zz} d\gamma \quad (\text{A.3})$$

---

Materials with a high resilience are able to store elastically large quantities of energy.

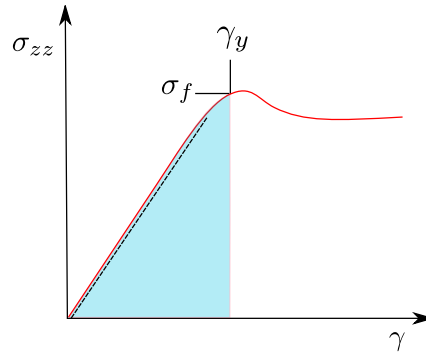


Figure A.3: Stress-strain curve in an experiment where the sample is subjected to tensile loading. The shaded area represents the resilience in Equation A.3.

The *loss coefficient* is defined as the ratio

$$\eta = \frac{\oint \sigma_{zz} d\gamma}{\int_0^{\gamma_{max}} \sigma_{zz} d\gamma} \quad (\text{A.4})$$

which is the ratio of the area of the hysteresis loop when a material is deformed cyclically up to some value  $\gamma_{max}$  and the amount of energy stored in the system when it is deformed up to  $\gamma_{max}$  (Figure A.4). The loss coefficient is also the inverse of the  $Q$  factor for a mechanical oscillator [1].

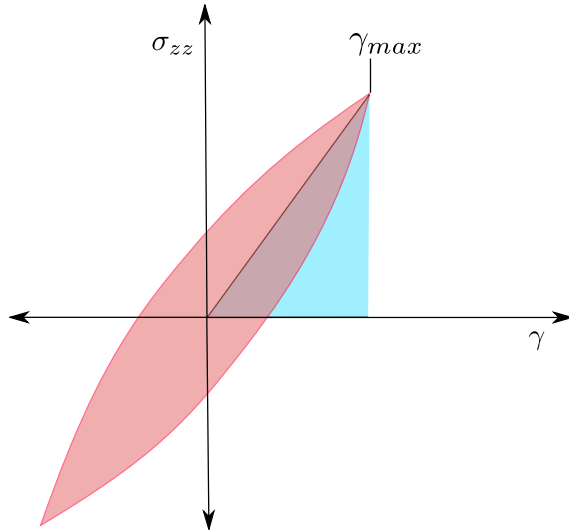


Figure A.4: Hysteresis stress-strain curve in an experiment where the sample is loaded cyclically. The loss coefficient in Equation A.4 is the ratio between the value of the red area and the light blue one.



## B The mortal random walk

### Derivation of the expression of the MSD

A particle system formed by  $N$  particles undergoing deformation can be represented as a state point in the  $3N$ -dimensional coordinate space. Here we focus on the configurations visited by a system subjected to oscillatory deformation at  $\gamma = 0$ , and assume that systems during such an experiment can be in two states:

- they're diffusing ("alive"), with a certain diffusion constant  $D$  (they thus perform a random walk in configuration space). On average, they move farther and farther from the configuration assumed for  $\gamma_{acc} = 0$  as  $\gamma_{acc}$  increases;
- they're absorbing ("dead"), and retain their coordinates for arbitrarily large values of  $\gamma_{acc}$ .

Furthermore, we assume that systems diffusing under deformation have some finite probability  $\lambda$  per unit  $\gamma_{acc}$  to stop their diffusive motion, thus becoming absorbing. Such "mortal" dynamics clearly violates the principle of detailed balance<sup>1</sup>.

The probability  $P(r, \gamma_{acc})$  to find a configuration at a distance  $r = \sqrt{N \cdot \text{MSD}}$  away from the starting point where the system is at  $\gamma_{acc} = 0$  after an oscillatory deformation

---

<sup>1</sup>Detailed balance is violated because a "living" state can "die", whereas resurrections are not possible!

## Appendix B. The mortal random walk

---

of  $\gamma_{acc}$  is given by:

$$P(r, \gamma_{acc}) = P_{alive}(r, \gamma_{acc}) + P_{dead}(r, \gamma_{acc}) \quad (\text{B.1})$$

$$= P_{alive}(\gamma_{acc}) P_{RW}(r, \gamma_{acc}) + \sum_{\gamma'_{acc}} P_{dying}(\gamma'_{acc}) P_{RW}(r, \gamma'_{acc}) \quad (\text{B.2})$$

$$= P_{alive}(\gamma_{acc}) P_{RW}(r, \gamma_{acc}) + \sum_{\gamma'_{acc}} P_{alive}(\gamma'_{acc}) \lambda P_{RW}(r, \gamma'_{acc}) \quad (\text{B.3})$$

$$\approx e^{-\lambda \gamma_{acc}} P_{RW}(r, \gamma_{acc}) + \int_0^{\gamma_{acc}} d\gamma'_{acc} e^{-\lambda \gamma'_{acc}} \lambda P_{RW}(r, \gamma'_{acc}) \quad (\text{B.4})$$

where  $P_{RW}(r, \gamma_{acc})$  is the probability for a random walker to be at a distance  $r$  away from the starting point after a deformation on  $\gamma_{acc}$ . As the mean squared displacement is defined as the second moment of  $P(r, \gamma_{acc})$ , we have

$$\text{MSD}(\gamma_{acc}) = \frac{1}{N} \int dr r^2 P(r, \gamma_{acc}) = \langle r^2(\gamma_{acc}) \rangle \quad (\text{B.5})$$

$$= \frac{1}{N} e^{-\lambda \gamma_{acc}} D\gamma_{acc} + \frac{1}{N} \int_0^{\gamma_{acc}} d\gamma'_{acc} e^{-\lambda \gamma'_{acc}} \lambda D\gamma'_{acc} \quad (\text{B.6})$$

$$= \frac{D}{\lambda N} (1 - e^{-\lambda \gamma_{acc}}) \quad (\text{B.7})$$

where the solution is obtained by integrating by parts and imposing  $\text{MSD}(0) = 0$  as a boundary condition. This expression of the mean squared displacement is used to fit the diffusion behavior in subsection 3.3.3.

# C Details of the NK model

## Reduction of the allowed configuration space

In section 4.1 the set of the configurations accessible to the NK models is restricted to the subset of  $N$ -tuples formed by ones and zeros that have the following property:

$$\sum_i m_i = \frac{N}{2} \quad (\text{C.1})$$

The reason to use this configuration space rather than the set of the  $2^N$   $N$ -tuples formed by ones and zeros is a bit subtle, and can be understood by looking at the following example. If the  $a$  function in Equation 4.4 is such that

$$\{0, \dots, 0\} \xrightarrow{a} \frac{1}{4} \quad (\text{C.2})$$

(so that the  $(K + 1)$ -tuple formed by zeros only maps through  $a$  onto  $\frac{1}{4}$ ) the value of the energy as measured from Equation 4.5 yields, for the configuration where all the  $N$  spins are identically zero, when  $\gamma = 0$ :

$$\begin{aligned} E &= -\frac{1}{2} \sum_{i=1}^N (1 + \sin(2\pi a_i + \gamma b_i)) \\ &= -\frac{1}{2} \sum_{i=1}^N (1 + 1) = -N \end{aligned} \quad (\text{C.3})$$

so that the energy assumes the lowest possible value ( $-N$ ) in correspondence of the configuration where all spins are 0. The sum in Equation C.3 gets simplified because all spins are equal to zero, all their neighbors are zero too, and thus each term  $a_i = \frac{1}{4}$  for all  $i$ . The value that the map  $a$  assumes in correspondence with the null  $(K + 1)$ -

## Appendix C. Details of the NK model

---

tuple gives rise to a very deep energy ground state (which is the null  $N$ -tuple), and neighboring configurations will (in general) have an energy strictly higher, analogously to what happens in the case of ferromagnetic states in the Ising model. The presence of a such a deep inherent structure in the NK landscape poses a problem because its basin is a potentially vast “funnel” that easily attracts the system during AQS dynamics<sup>1</sup>. Furthermore, by changing  $\gamma$  such a deep minimum is possibly not destabilized, especially if  $b$  in Equation 4.4 maps the null  $(K + 1)$ -tuple to a value close to 0.

The same problem of course exists if  $a$  maps the  $K$ -tuple formed by all ones onto a value close to 1/4. Two strategies can be envisaged in order to cure this problem:

1. restricting the possible values of the couplings  $a$  and  $b$ : the “pathologic” values of the couplings  $a$  and  $b$  can be forced not to assume problematic values in correspondence to the  $(K + 1)$ -tuples with all equal values. This can be achieved in practice by choosing a non-uniform probability distribution in the choice of the values of the couplings Equation 4.4. This presumably rules out energy landscapes presenting “trivial” deep ground states and undesired topologies. It’s not clear, however, what kind of probability distribution one should use;
2. restricting the number of states: the problematic states of the energy landscape can simply be removed from the accessible landscape. This is the choice made in section 4.1 and summarized by Equation C.1, where just the subset of all the  $N$ -tuples of constant “magnetization” equal to  $N/2$  is taken as the set of allowed configurations. Such method is arguably more elegant than the previous one, but comes at a high price: whereas in the entire space of the  $N$ -tuples configurations lie on a simple (hyper-)cubic lattice where all configurations have  $N$  nearest neighbors at a distance  $d = 1$ , in the subset nearest neighbors are separated by  $\sqrt{2}$  and are many more ( $N^2/4$ ). This increases the complexity of the steepest descent algorithm used to perform AQS on the NK model, making the study of the model computationally expensive if  $N$  is large.

## Example of the NK model, ground state degeneracy

A simple example can help to understand how the NK model works, and some of the features that it can have (in this case, ground state degeneracy). We set  $\gamma = 0$  for simplicity and take  $N = 4, K = 1$ : Consider the map  $a$ :

$$\{0, 0\} \xrightarrow{a} 0 \quad \{0, 1\} \xrightarrow{a} \frac{1}{4} \quad \{1, 0\} \xrightarrow{a} 0 \quad \{1, 1\} \xrightarrow{a} 0 \tag{C.4}$$

---

<sup>1</sup>Loosely speaking, the “ferromagnetic” configuration acts as a crystalline configuration which can be easily reached starting from any point of the energy landscape.

---

and the neighbor lists for each spin:

$$\{1, 2\}, \{2, 1\}, \{3, 4\}, \{4, 3\} \quad (\text{C.5})$$

Let's enumerate all the energies of the allowed 4-tuples, calculated from the expression in Equation 4.5 using the information in Equation C.4 and Equation C.5:

$$\begin{aligned} E(0, 0, 1, 1) &= -2 \\ E(0, 1, 0, 1) &= -3 \\ E(0, 1, 1, 0) &= -3 \\ E(1, 0, 0, 1) &= -3 \\ E(1, 0, 1, 0) &= -3 \\ E(1, 1, 0, 0) &= -2 \end{aligned} \quad (\text{C.6})$$

In this simple example one sees that the minimum possible value of energy  $-N = -4$  is not attained and that the ground state is four-fold degenerate.

## Density of states and of inherent structures in the NK model

A distinctive and nice feature of the NK model is that it has a discrete set of states: for a given value of  $N$  there are  $\binom{N}{N/2}$  allowed configurations. If this number is not too large one can enumerate each of them and calculate their energy by means of Equation 4.5. In this way one can calculate the density of states (DOS). This is done in Figure C.1, where the density of states is shown to be gaussian.

Furthermore, by applying a steepest descent (SD) procedure using Kawasaki moves [88], one can even *minimize all the allowed states one by one* (at least if  $N$  is small enough), and thus find *all* the inherent structures of the NK landscape and their energies. This brute force approach is clearly not feasible with particle systems, where the set of allowed states is not countable. Doing so, one can extract the density of inherent states, which is also plotted in Figure C.1. Clearly, the features of the DOS mentioned above will depend on the choice of  $N$ ,  $K$ , and the value of the parameters needed to compute  $E$  in Equation 4.5. Whenever brute force computation of the states is feasible, the system can be studied at some given  $T$  by calculating the partition function via the sum of the Boltzmann factors  $e^{-\beta U}$ , and ensemble averages can be performed in a straightforward way. If  $N$  is large, however, the number of states becomes huge, and the system needs to be studied by means of sampling methods, like the Monte Carlo method [61]. To do this one starts from some given configuration and attempts Kawasaki moves to neighboring ones, accepting or rejecting the moves according to the Metropolis rule for the given  $T$ . After a transient, the system equilibrates on a trajectory that samples states with

## Appendix C. Details of the NK model

---

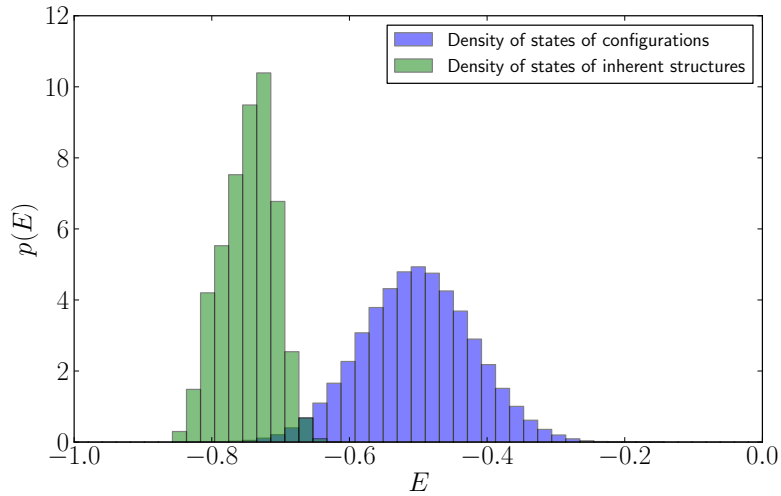


Figure C.1: Density of states and of inherent states of an NK model with  $N = 20$  and  $K = 10$ . The form of the DOS is gaussian.

a probability proportional to their Boltzmann factor. Such states can be minimized in energy via SD so to obtain the associated inherent structures, which in turn can be used as starting configurations for athermal “deformation” simulations.

## D Details of the TM model

### Details of the construction of $P$

Here we describe how the assumptions listed in subsection 4.2.2 can be used to construct  $P$ . First of all, one can see that

$$P = P_- P_+ \quad (\text{D.1})$$

so that the construction of  $P$  is reduced to that  $P_+$  and  $P_-$ . Each of these (say  $P_+$ ), can in turn be viewed as the composition of matrices

$$P_+ = P_{\leftarrow}^0 \dots P_{\leftarrow}^{\gamma_{max}-d\gamma} P_{\rightarrow}^{\gamma_{max}} P_{\rightarrow}^{\gamma_{max}-d\gamma} \dots P_{\rightarrow}^{2d\gamma} P_{\rightarrow}^{d\gamma} \quad (\text{D.2})$$

where  $P_{\rightarrow}^{\gamma^*}$  is the matrix describing how AQS dynamics maps the inherent structures of the landscape relative to  $\gamma = \gamma^* - d\gamma$  into the set of the structures of the landscape associated to  $\gamma = \gamma^*$ . The arrows in the subscript indicate whether  $P^{\gamma^*}$  is associated to an increase of  $\gamma$  ( $\rightarrow$ ) or a decrease ( $\leftarrow$ ) in strain. For instance,  $P_{\leftarrow}^{\gamma^*}$  describes how AQS maps the structures of the  $\gamma = \gamma^* + d\gamma$  landscape onto those associated to  $\gamma = \gamma^*$ . As the landscape is assumed to have  $M$  inherent structures no matter the value of  $\gamma$ , each of these  $P_{\rightarrow}^{\gamma^*}$ ,  $P_{\leftarrow}^{\gamma^*}$  is a square matrix. To construct each of the  $P_{\rightarrow}^{\gamma^*}$  one uses the assumption that the probability per unit strain to destabilize a given inherent structure is equal to  $\tau$ . So, when the strain is incremented by  $d\gamma$ , a system in a given inherent structure has probability  $1 - \tau d\gamma$  to be in a structure  $i$  that is not destabilized, and thus it maps to the same structure  $\mathbf{R}_i$  in the deformed landscape through  $P_{\rightarrow}^{\gamma^*}$ . In that case the matrix element  $P_{\rightarrow,ii}^{\gamma^*} = 1$ . The system has also a probability  $\tau d\gamma$  to be in a structure  $\mathbf{R}_j$  that is destabilized by the strain increment, so that it falls onto some randomly chosen inherent structure  $\mathbf{R}_k$  of the deformed landscape. in that case the matrix element  $P_{\rightarrow,kj}^{\gamma^*} = 1$ . Incidentally, for each configuration  $\mathbf{R}_l$  that is destabilized at  $\gamma^*$  as strain is increased, another configuration  $\mathbf{R}_m$  is correspondingly created at that strain value. This means that  $\mathbf{R}_m$  will be destroyed at  $\gamma^*$  when the strain will be decreased (due to the symmetry

## Appendix D. Details of the TM model

---

of the landscapes). This is a constraint on the form of the matrix  $P_{\leftarrow}^{\gamma^*}$ :  $P_{\leftarrow}^{\gamma^*}$  must be constructed by taking into account that the structures that are destroyed at  $\gamma^*$  when incrementing  $\gamma$  are exactly those created at  $\gamma^*$  when decrementing  $\gamma$ .

The procedure outlined above is used to create a matrix  $P_+$  associated to some  $\gamma_{max}$ . The  $P'_+$  corresponding to another  $\gamma'_{max}$  is simply given by

$$P'_+ = P_{\leftarrow}^0 \dots P_{\leftarrow}^{\gamma'_{max}-d\gamma} P_{\rightarrow}^{\gamma'_{max}} P_{\rightarrow}^{\gamma'_{max}-d\gamma} \dots P_{\rightarrow}^{2d\gamma} P_{\rightarrow}^{d\gamma} \quad \text{if } \gamma'_{max} < \gamma_{max} \quad (\text{D.3})$$

$$\begin{aligned} P'_+ = P_{\leftarrow}^0 \dots P_{\leftarrow}^{\gamma_{max}-d\gamma} P_{\leftarrow}^{\gamma_{max}} P_{\leftarrow}^{\gamma_{max}+d\gamma} \dots P_{\leftarrow}^{\gamma'_{max}-d\gamma} P_{\rightarrow}^{\gamma'_{max}} P_{\rightarrow}^{\gamma'_{max}-d\gamma} \\ \dots P_{\rightarrow}^{\gamma_{max}+d\gamma} P_{\rightarrow}^{\gamma_{max}} P_{\rightarrow}^{\gamma_{max}-d\gamma} \dots P_{\rightarrow}^{2d\gamma} P_{\rightarrow}^{d\gamma} \quad \text{if } \gamma'_{max} > \gamma_{max} \end{aligned} \quad (\text{D.4})$$

Using this procedure its thus possible to create a sequence of matrices relative to multiple values of  $\gamma_{max}$ .

A Python code capable of generating  $P_+$  (or  $P_-$ ) for a given value of  $\gamma_{max}$  is proposed below.

## Python implementation

Here we quote some Python code capable of generating one of the  $P_+$  and  $P_-$  matrices using the assumptions of the TM model. We warn the reader that this is a short and readable implementation that is not efficient as the size of the matrices  $M$  gets large. For large  $M$ , sparse matrices need to be employed (these can be easily handled by the SciPy library [82]).

```

1 import sys
2 import numpy as np
3 import pylab as plt
4
5 M = int(sys.argv[1])
6 p = float(sys.argv[2])
7 gamma_max = int(sys.argv[3])
8 np.random.seed(123456)
9
10 allPplus = np.eye(M)
11 allPminus = np.eye(M)
12
13 for gammastar in range(1, gamma_max):
14
15     Pplus = np.zeros((M, M))
16     Pminus = np.zeros((M, M))
17     unstable = np.random.rand(M) < p
18     for i in xrange(M):
19         if unstable[i]:
```

---

```
20         dest = np.random.randint(M)
21         Pplus[dest,i] = 1
22     else:
23         Pplus[i,i] = 1
24     for i in xrange(M):
25         if unstable[i]:
26             dest = np.random.randint(M)
27             Pminus[dest,i] = 1
28         else:
29             Pminus[i,i] = 1
30
31     allPplus = np.dot(Pplus, allPplus)
32     allPminus = np.dot(allPminus, Pminus)
33
34 Pplus = np.dot(allPminus, allPplus)
35 plt.spy(Pplus)
36 plt.show()
```



# E Athermal deformation of gels and bigels

In this appendix, after a brief description of their properties, we discuss how *particle gels* and *bigels* (a new kind of system recently found in computer simulations and realized experimentally using DNA-coated colloids [89]) behave under athermal quasi static deformation. Even though these systems are physically different from metallic glasses, a qualitative treatment of their properties can be performed using the same methods that have been described in chapter 2 and employed in chapter 3, with minor modifications to the model. The main findings presented in this chapter have been published in [90].

## Gels and bigels

If a fluid above its critical temperature is cooled down and crosses its gas-liquid transition line, it separates in two distinct phases in equilibrium. Such phases coexist at the same pressure, and have different densities. A particular example is constituted by *colloids*. In a colloid, solid particles (named *colloidal particles*) whose size ranges from 1 nm to 1  $\mu\text{m}$  are dispersed in a liquid solvent<sup>1</sup>. Above some critical temperature the colloidal particles form a single homogeneous phase. If the system is cooled down (or, conversely, the interactions between the particles are strengthened) the system can separate in a “colloid-rich” phase (which is characterized by a high density of colloidal particles) and a “colloid-poor” one, separated by an interface. The dynamics of such phase separation depends on the nature of the system and on the rate at which the system is cooled down. One of the ways in which the system can separate in two phases goes under the name of *spinodal decomposition*. In a spinodal decomposition phase separation takes place everywhere in a given sample, with the two phases organizing in an intertwined structure whose characteristic lengthscale grows with time. For some kinds of interparticle interactions, if the quench is sufficiently fast so that low temperatures are reached before such lengthscale has grown, the spinodal decomposition can be *ar-*

---

<sup>1</sup>In an experimental setup the density of the colloidal particles is often made equal to that of the solvent, so that the effect of gravity is compensated by buoyancy.

## Appendix E. Athermal deformation of gels and bigels

---

rested [91–93]. This arrest is similar to the one observed in glasses, with the system maintaining for long times configurations out of equilibrium, rather than separating into two bulk phases separated by an interface. The arrested configuration observed in some colloidal systems is an inhomogeneous, ramified, tenuous and system spanning structure composed of colloidal particles, which goes under the name of *particle gel*. Particle gels have been observed for instance in [93], using colloids formed by PMMA beads suspended in a solvent with the same density and refractive index of the beads. In that case the “quench” is obtained by adding linear polystyrene chains to the solution, so to induce an effective isotropic depletion attraction [94] between the particles. Qualitatively, similar results have been obtained in MD simulations modeling colloids as point particles interacting via the Asakura-Oosawa potential (which is the analytical description of depletion interaction [94]) or a modified Lennard-Jones potential characterized by a very short interaction range [93], as well as in event-driven MD of point particles interacting via a short-ranged square-well potential.

Recently, a more complex class of systems was discovered [89], by using mixtures of particles as those described above, characterized by an attractive interaction between particles of the same species and a repulsive interaction between particles of different species. Systems of this kind could be realized experimentally by grafting polystyrene beads with functionalized DNA, which is able to induce attraction on complementary strands. As these systems are quenched by lowering the temperature, the mixture undergoes *demixing* [95] and finally colloidal particles form interpenetrating structures. Each of these structures is composed by particles of a single species only, and is very close to that of a gel. In the case of binary mixtures, these structures were named *bigels* [89]. Similar structures have been first obtained by means of event driven MD simulations [89], quenching particles interacting with an intraspecies square-well potential and a hard-sphere interspecies potential.

## Computer simulation of gels

The mechanical properties of *particle gels* are a subject of ongoing investigations (see [96, 97] for examples of recent experimental work), and those of bigels have (to our knowledge) never been probed before, neither in experiments nor simulations. In what follows we present computer simulations of AQS deformation of gel-like and bigel-like structures obtained by using a short-ranged Lennard-Jones potential.

---

## Modified Lennard-Jones binary mixture

In what follows we consider a modified cut and shifted Lennard-Jones potential of the form

$$U_{\alpha\beta}(r) = \begin{cases} 4\epsilon \left( \left(\frac{\sigma}{r}\right)^m - \left(\frac{\sigma}{r}\right)^n \right) + U_{\alpha\beta}^{shift}, & \text{if } r \leq \lambda_{\alpha\beta}\sigma \\ 0, & \text{if } r > \lambda_{\alpha\beta}\sigma \end{cases}, \quad (\text{E.1})$$

where  $m = 64$ ,  $n = 32$ , in order to get a short ranged potential. We use this potential both to describe interaction within a pure fluid of a single species (so that its concentration is  $c = N_A/N = 1$ ) and a symmetric two-component mixture ( $c = 0.5$ ). The choice of parameters here is  $\epsilon = 1$  and  $\sigma = 1$ , and the attraction and repulsion is determined by the value of the cut-off  $\lambda_{\alpha\beta}$ . By setting  $\lambda_{AB} = 1$  and  $\lambda_{AA} = \lambda_{BB} = 1.4$  the inter-species interaction is made purely repulsive, whereas attraction exists at intermediate range for particles of the same species. The choice of the exponents is such to make the potential  $U_{AB}$  sufficiently short-ranged, and  $U_{shift}$  is chosen to make  $U_{\alpha\beta}$  continuous at the cut-off.

## Preparation of the samples

We take a system composed by  $N = 50000$  particles of species  $A$  at packing fraction<sup>2</sup>  $\phi = 0.1$ , and another one of the same dimensions composed by  $N_A = 25000$  of species 1 and  $N_B = 25000$  of species 2 and simulate it using LAMMPS<sup>3</sup>. Such particles are initially placed at random in a simulation box with periodic boundary conditions. Then, an energy minimization is applied in order to remove overlaps between the particles. The two systems are initially thermostated at  $T = 100$ , and subsequently quenched from  $T = 100$  to  $T = 0.01$  by connecting them to a Berendsen [62] thermostat at  $T = 0.01$ . The initial temperature is chosen to have such a high value so to follow a procedure which is as close to that followed in [89] as possible. In order to ensure numerical stability at high temperatures, when particles have a high kinetic energy and thus undergo large displacements per unit time, a very small time step  $dt = 10^{-5}$  (in reduced units) is employed. As the temperature is decreased,  $dt$  is increased to 0.001 to reduce computational overhead and follow the system for longer times.

The result of this preparation are respectively gel-like and bigel-like structures, whose visual inspection (see snapshots on the top Figure E.3) reveals a strong resemblance with what is observed in simulations using square well interaction potentials in [89]. In addition, after having waited enough time after the beginning of the quench, both the

---

<sup>2</sup>If one assumes that the volume occupied by a single particle is equal to  $\frac{4}{3}\pi \left(\frac{\sigma}{2}\right)^3$ , the packing fraction  $\phi$  is defined to be fraction of the overall volume occupied by the particles. The packing fraction is related to the number density  $\rho$  through the formula  $\phi = \frac{\pi}{6}\rho$  if  $\sigma = 1$ .

<sup>3</sup>The potential in Equation E.1 is not implemented in LAMMPS for general values of  $m$  and  $n$ , and was coded by the author following the templates available within the source code of LAMMPS (see [85]).

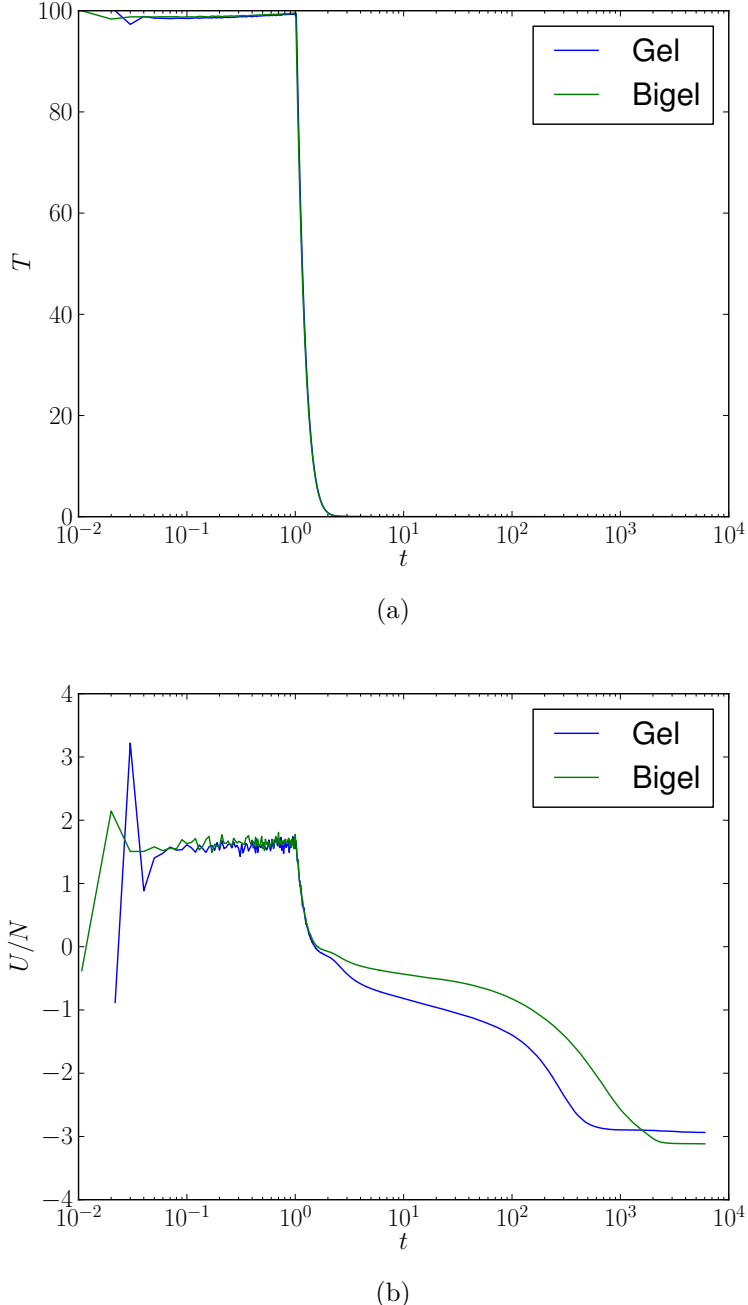


Figure E.1: (a) Temperature profile applied over time during the quench of the single component and the two component mixture. (b) Potential energy profile during the quench for the two cases. During the quench the energy progressively lowers, and finally reaches a regime where it drifts extremely slowly downward. At this stage ( $t \approx 10^3$ ) the gel and bigel structures can be considered to be arrested.

---

MSD of the particles and the potential energy  $U$  (Figure E.1) saturate to nearly-constant values. At that stage, one can consider the phase separation to be arrested.

## Appendix E. Athermal deformation of gels and bigels

---

### Athermal deformation behavior of gels and bigels

Quenched configurations that have reached a plateau in the potential energy and MSD are subjected to a potential energy minimization using the conjugate-gradient algorithm. This allows them to reach mechanically stable minima. Such configurations of minimum energy are shear-strained up to a large values of the strain ( $\gamma = 10$ ) by varying the boundary conditions using the AQS procedure described in chapter 2 and employing a  $d\gamma = 10^{-5}$ . Imposing energy minimization at each AQS step corresponds to considering the system as composed of “sticky” particles, able to form and destroy bonds only as a consequence of a change in strain. Values of the shear stress in the plane of the applied strain and configurations are computed with Equation 3.4 and dumped at regular intervals as the strain is increased, so that the evolution of the sample under deformation can be monitored.

The mechanical behavior of gels and bigels is very different, at least for the set of parameters chosen here. For low values of the strain, the two systems both show an elastic behavior with a linear dependence of the shear stress from the shear strain Figure E.2. The bigel, however, appears to be much stiffer than the gel. This is possibly due to the fact that deformation brings different branches of the intertwined structure in contact, and that the two systems behave in a different way as a consequence of this. In the gel, branches brought in contact are formed by particles of the same species, and thus when in contact stick together because of the attractive intraspecies interaction. In a bigel, instead, branches in contact can be formed by particles belonging to different species. In this latter case, branches do repel each other, and thus impede the system to comply to the deformation. At a larger value of the strain, which is approximately equal for the two kinds of systems, the stress deviates from linearity and both the gel and the bigel yield. As a consequence of the larger stiffness of the bigel, its yield stress is much larger than that of the gel. For strains larger still, the two systems undergo large modifications, but in qualitatively distinct ways (see Figure E.3). The ramified structure of the gel is gradually destroyed, with dangling branches lumping together so to form a less porous structure which is clearly not percolating in the simulation box, and a stress correspondingly falling to low values for large strains. Such compaction is not observed in the case of bigels. In fact, as strain is increased, the ramified structure of bigels breaks up into a “gas” of disconnected clusters of particles of the two species. Is this difference in behavior related to the fact that the two component of a bigel form structures that more tenuous than those of a gel with the same packing fraction? In principle this could be true, because the gel is a single structure made out of  $N$  particles, whereas the bigel is made out of two intertwining networks each containing  $N_A = N_B = N/2$  particles. We have verified that this is not the case by studying the deformation behavior of a single component gel formed by  $N/2$  particles in a box with the same dimensions as that used with the gels with  $N$  particles. This system is approximately equivalent to the structure formed by a single component in a bigel, if the one formed by the other component is disregarded. We checked that the large deformation behavior of such a gel

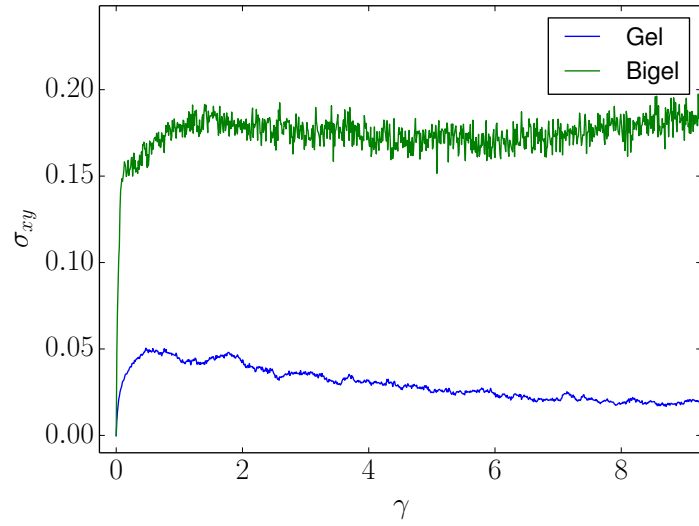


Figure E.2: Shear stress as a function of shear strain averaged over  $\approx 8$  gel and bigel samples of  $\phi = 0.1$ . The bigel is stiffer, and is able to sustain a larger stress for large values of the strain.

(with  $\phi = 0.05$ ) is qualitatively equivalent to that of the  $\phi = 0.1$  gel. This suggests that the difference in the large strain behavior observed in bigels is likely to be due to the presence of particles of the other species, which behaves like an obstacle that impedes to particles of a given species to bond together and form a large compact cluster.

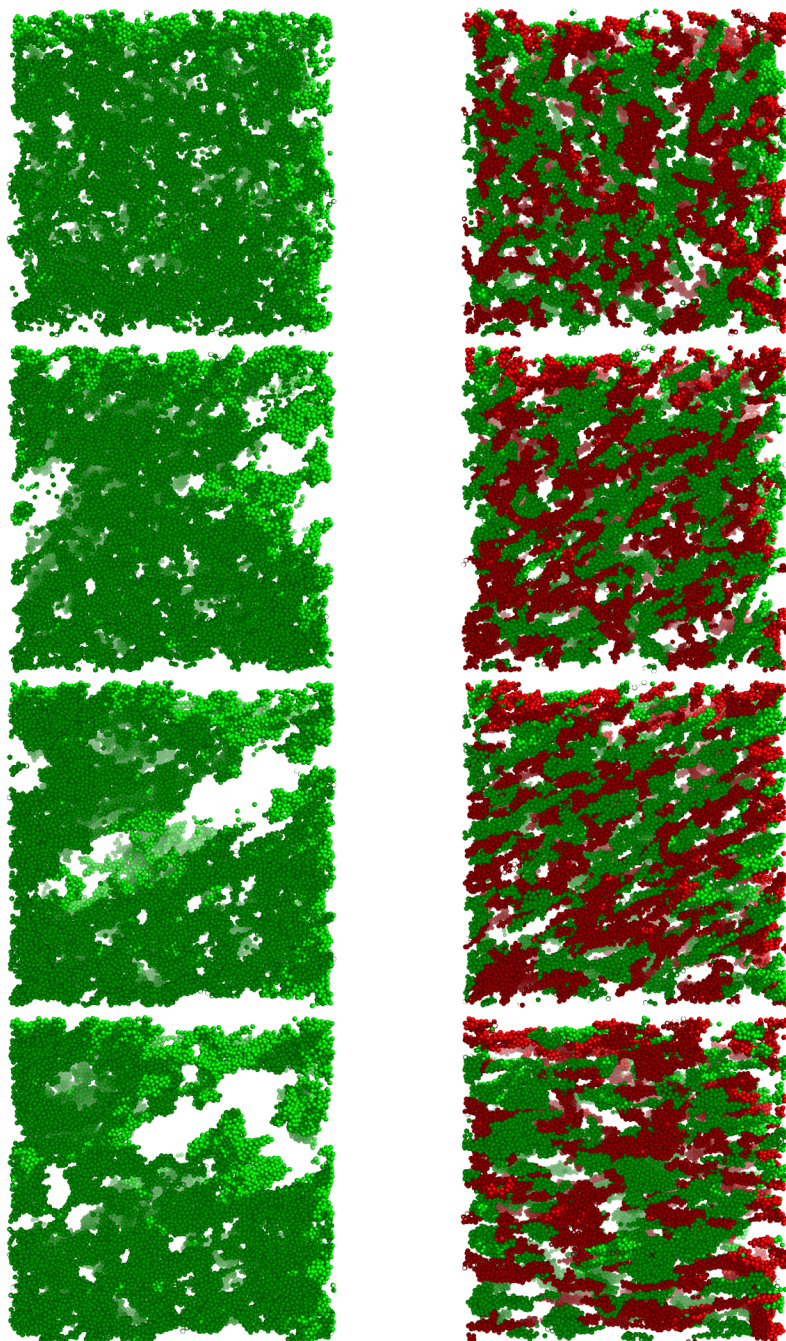


Figure E.3: Configuration of a gel (left) and a bigel (right) of  $\phi = 0.1$  at  $\gamma = 0, 1, 2, 8$ . With an increase in shear strain, the gel ruptures and compacts. The bigel does form a gas of disconnected clusters instead.

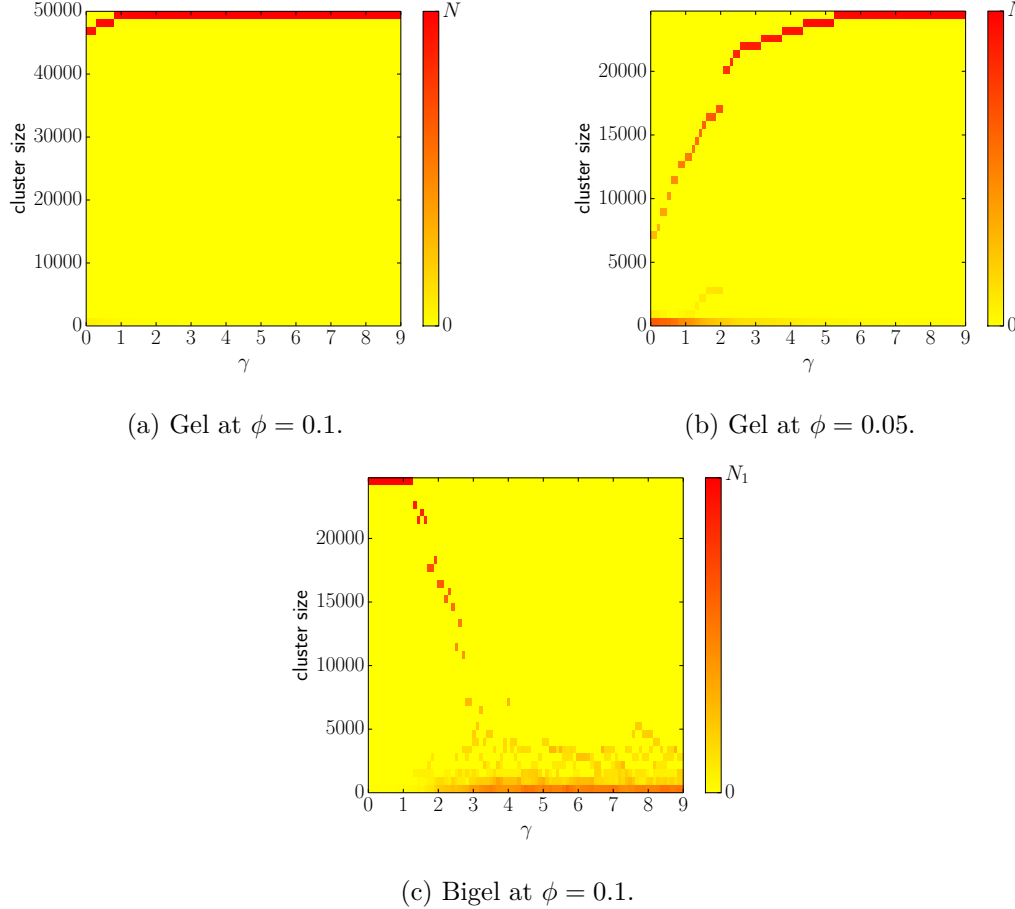


Figure E.4: In these heatmaps, we represent the total number of particles of species  $A$  that belong to a cluster whose size is indicated on the  $y$ -axis, as a function of the strain  $\gamma$ , for gels and bigels systems. Particles are considered to belong to the same cluster if they belong to the same species and their centers are separated by a distance lower than 1.4. Under deformation the particles of the gels form a single cluster containing almost all the particles (in the case of the gel at  $\phi = 0.05$ , the largest cluster actually *grows*). In the case of the bigel, the structure breaks into smaller clusters as strain is increased.

### **Summary and outlook**

Our data show that bigels have interesting mechanical properties that differentiate them from gel structures formed by particles of a given kind only. Gels and bigels are both elastic at small strains, but bigels appear stiffer. Large strains are able to destroy the percolating structures in both the cases of gels and bigels. However, gels and bigels do rupture in quite different ways, with gels aggregating in a single, dense cluster and bigels breaking up in multiple smaller clusters (at least in the range of strains examined here). One can speculate, on the basis of our data, that a reversal of the strain will not make any of the two kinds of systems recover the ramified and percolating configurations that they had before the deformation. We posit that the result of strain reversal of deformed gels will be a compact cluster, and a gas of clusters in the case of bigels, with none of the two systems showing the capability to spontaneously heal as strain is reversed.

Our results could be confirmed by carrying out rheological experiments on bigels, with particle positions being able to be measured by means of confocal microscopy as in [89].

## F Data preservation

Part of the data presented in the plots and the scripts needed to generate them are available together with code related to the LJ, NK, and TM models and the input parameters used in the simulations on

<https://github.com/davidefiocco/phd-thesis>

On this repository (referred to in the text as “[85]”) the interested reader can find the additional material mentioned in the thesis and a list of corrections to typos.



# Bibliography

- [1] M. F. Ashby, “Materials selection in mechanical design,” *MRS BULLETIN*, vol. 30, p. 995, 2005.
- [2] L. Hamill, S. Roberts, M. Davidson, W. L. Johnson, S. Nutt, and D. C. Hofmann, “Hypervelocity impact phenomenon in bulk metallic glasses and composites,” *Advanced Engineering Materials*, 2013.
- [3] J. Schroers, T. Nguyen, S. O’Keeffe, and A. Desai, “Thermoplastic forming of bulk metallic glass – applications for MEMS and microstructure fabrication,” *Materials Science and Engineering: A*, vol. 449, pp. 898–902, 2007.
- [4] J. Horton and D. Parsell, “Biomedical potential of a zirconium-based bulk metallic glass,” *Elastic*, vol. 130, no. 150, p. 547, 2003.
- [5] W. Klement, R. Willens, and P. Duwez, “Non-crystalline structure in solidified gold–silicon alloys,” *Nature*, 1960.
- [6] R. Vaidyanathan, M. Dao, G. Ravichandran, and S. Suresh, “Study of mechanical deformation in bulk metallic glass through instrumented indentation,” *Acta Materialia*, vol. 49, no. 18, pp. 3781–3789, 2001.
- [7] M. P. Allen and D. J. Tildesley, *Computer simulation of liquids*. Oxford university press, 1989.
- [8] P. Schall, D. A. Weitz, and F. Spaepen, “Structural rearrangements that govern flow in colloidal glasses,” *Science*, vol. 318, no. 5858, pp. 1895–1899, 2007.
- [9] M. Chen, “A brief overview of bulk metallic glasses,” *NPG Asia Materials*, vol. 3, no. 9, pp. 82–90, 2011.
- [10] A. Inoue, “Stabilization of metallic supercooled liquid and bulk amorphous alloys,” *Acta materialia*, vol. 48, no. 1, pp. 279–306, 2000.
- [11] E. Bakke, R. Busch, and W. Johnson, “The viscosity of the ZrTiCuNiBe bulk metallic glass forming alloy in the supercooled liquid,” *Applied Physics Letters*, vol. 67, p. 3260, 1995.

## Bibliography

---

- [12] M. Ediger, C. Angell, and S. R. Nagel, “Supercooled liquids and glasses,” *The Journal of Physical Chemistry*, vol. 100, no. 31, pp. 13200–13212, 1996.
- [13] P. G. Debenedetti and F. H. Stillinger, “Supercooled liquids and the glass transition,” *Nature*, vol. 410, no. 6825, pp. 259–267, 2001.
- [14] R. Busch, J. Schroers, and W. Wang, “Thermodynamics and kinetics of bulk metallic glass,” *Mrs Bulletin*, vol. 32, 2007.
- [15] Q. Luo, B. Zhang, D. Zhao, R. Wang, M. Pan, and W. Wang, “Aging and stability of cerium-based bulk metallic glass,” *Applied physics letters*, vol. 88, no. 15, pp. 151915–151915, 2006.
- [16] S. Khonik, A. Makarov, K. Podurets, A. Lysenko, and V. Khonik, “Comparative study of relaxation behavior of glassy “usual”  $Pd_{40}Cu_{30}Ni_{10}P_{20}$  and “unusual”  $Pd_{40}Cu_{40}P_{20}$  by measurements of the electrical resistance,” *Intermetallics*, vol. 20, no. 1, pp. 170–172, 2012.
- [17] B. Ruta, Y. Chushkin, G. Monaco, L. Cipelletti, E. Pineda, P. Bruna, V. Giordano, and M. Gonzalez-Silveira, “Atomic-scale relaxation dynamics and aging in a metallic glass probed by X-ray photon correlation spectroscopy,” *Physical Review Letters*, vol. 109, no. 16, p. 165701, 2012.
- [18] J. Wang, L. Liu, J. Xiao, T. Zhang, B. Wang, C. Zhou, and W. Long, “Ageing behaviour of  $Pd_{40}Cu_{30}Ni_{10}P_{20}$  bulk metallic glass during long-time isothermal annealing,” *Journal of Physics D: Applied Physics*, vol. 38, no. 6, p. 946, 2005.
- [19] S. Chathoth and K. Samwer, “Stokes-Einstein relation in dense metallic glass-forming melts,” *Applied Physics Letters*, vol. 97, no. 22, pp. 221910–221910, 2010.
- [20] M. Ashby and A. Greer, “Metallic glasses as structural materials,” *Scripta Materialia*, vol. 54, no. 3, pp. 321–326, 2006.
- [21] C. A. Schuh, T. C. Hufnagel, and U. Ramamurty, “Mechanical behavior of amorphous alloys,” *Acta Materialia*, vol. 55, no. 12, pp. 4067–4109, 2007.
- [22] W. Peter, P. Liaw, R. Buchanan, C. Liu, C. Brooks, J. Horton Jr, C. Carmichael Jr, and J. Wright, “Fatigue behavior of  $Zr_{52.5}Al_{10}Ti_5Cu_{17.9}Ni_{14.6}$  bulk metallic glass,” *Intermetallics*, vol. 10, no. 11, pp. 1125–1129, 2002.
- [23] D. C. Hofmann, J.-Y. Suh, A. Wiest, G. Duan, M.-L. Lind, M. D. Demetriou, and W. L. Johnson, “Designing metallic glass matrix composites with high toughness and tensile ductility,” *Nature*, vol. 451, no. 7182, pp. 1085–1089, 2008.
- [24] A. Concustell, F. Méar, S. Surinach, M. Baró, and A. Greer, “Structural relaxation and rejuvenation in a metallic glass induced by shot-peening,” *Philosophical Magazine Letters*, vol. 89, no. 12, pp. 831–840, 2009.

- [25] C. Packard, L. Witmer, and C. Schuh, “Hardening of a metallic glass during cyclic loading in the elastic range,” *Applied Physics Letters*, vol. 92, no. 17, pp. 171911–171911, 2008.
- [26] A. Cavagna, “Supercooled liquids for pedestrians,” *Physics Reports*, vol. 476, no. 4, pp. 51–124, 2009.
- [27] K. Binder and W. Kob, *Glassy Materials and Disordered Solids: An Introduction to Their Statistical Mechanics (Revised Edition)*. World Scientific, 2011.
- [28] L. Berthier and G. Biroli, “Theoretical perspective on the glass transition and amorphous materials,” *Reviews of Modern Physics*, vol. 83, no. 2, p. 587, 2011.
- [29] M. Ediger and P. Harrowell, “Perspective: Supercooled liquids and glasses,” *The Journal of Chemical Physics*, vol. 137, p. 080901, 2012.
- [30] F. Sciortino, “Potential energy landscape description of supercooled liquids and glasses,” *Journal of Statistical Mechanics: Theory and Experiment*, vol. 2005, no. 05, p. P05015, 2005.
- [31] A. Heuer, “Exploring the potential energy landscape of glass-forming systems: from inherent structures via metabasins to macroscopic transport,” *Journal of Physics: Condensed Matter*, vol. 20, no. 37, p. 373101, 2008.
- [32] F. H. Stillinger, “A topographic view of supercooled liquids and glass formation,” *Science*, vol. 267, no. 5206, pp. 1935–1939, 1995.
- [33] J. P. Doye, M. A. Miller, and D. J. Wales, “Evolution of the potential energy surface with size for Lennard-Jones clusters,” *The Journal of Chemical Physics*, vol. 111, p. 8417, 1999.
- [34] O. M. Becker and M. Karplus, “The topology of multidimensional potential energy surfaces: Theory and application to peptide structure and kinetics,” *Journal of Chemical Physics*, vol. 106, no. 4, pp. 1495–1517, 1997.
- [35] B. Bollobás, *Modern graph theory*, vol. 184. Springer, 1998.
- [36] V. K. de Souza and D. J. Wales, “Connectivity in the potential energy landscape for binary Lennard-Jones systems,” *The Journal of Chemical Physics*, vol. 130, p. 194508, 2009.
- [37] B. Doliwa and A. Heuer, “Hopping in a supercooled Lennard-Jones liquid: Metabasins, waiting time distribution, and diffusion,” *Physical Review E*, vol. 67, no. 3, p. 030501, 2003.
- [38] S. Sastry, “The relationship between fragility, configurational entropy and the potential energy landscape of glass-forming liquids,” *Nature*, vol. 409, no. 6817, pp. 164–167, 2001.

## Bibliography

---

- [39] S. Mossa and F. Sciortino, “Crossover (or Kovacs) effect in an aging molecular liquid,” *Physical Review Letters*, vol. 92, no. 4, p. 045504, 2004.
- [40] M. S. Daw, S. M. Foiles, and M. I. Baskes, “The embedded-atom method: a review of theory and applications,” *Materials Science Reports*, vol. 9, no. 7, pp. 251–310, 1993.
- [41] W. Kob and H. C. Andersen, “Testing mode-coupling theory for a supercooled binary Lennard-Jones mixture i: The van Hove correlation function,” *Physical Review E*, vol. 51, no. 5, p. 4626, 1995.
- [42] L. Berthier, G. Biroli, J.-P. Bouchaud, L. Cipelletti, D. El Masri, D. L’Hôte, F. Ladieu, and M. Pierno, “Direct experimental evidence of a growing length scale accompanying the glass transition,” *Science*, vol. 310, no. 5755, pp. 1797–1800, 2005.
- [43] D. Rodney, A. Tanguy, and D. Vandembroucq, “Modeling the mechanics of amorphous solids at different length scale and time scale,” *Modelling and Simulation in Materials Science and Engineering*, vol. 19, no. 8, p. 083001, 2011. **This review paper is a nice introduction to the problem of mechanical deformation of amorphous solids and the models that try to attack it at different levels of granularity.**
- [44] M. Falk and C. Maloney, “Simulating the mechanical response of amorphous solids using atomistic methods,” *The European Physical Journal B*, vol. 75, no. 4, pp. 405–413, 2010.
- [45] D. J. Lacks and M. J. Osborne, “Energy landscape picture of overaging and rejuvenation in a sheared glass,” *Physical Review Letters*, vol. 93, no. 25, p. 255501, 2004. **This is a key paper of this thesis. It contains the results of simulations of oscillatory deformation of a model glass, observing overaging and rejuvenation. In this thesis we aimed at extending the observations contained here to a oscillatory shear simulations consisting in a large number of cycles.**
- [46] M. Utz, P. G. Debenedetti, and F. H. Stillinger, “Atomistic simulation of aging and rejuvenation in glasses,” *Physical Review Letters*, vol. 84, no. 7, p. 1471, 2000. **This is a key paper of this thesis. It is the first observation of rejuvenation in a computer simulation of a model glass.**
- [47] B. A. Isner and D. J. Lacks, “Generic rugged landscapes under strain and the possibility of rejuvenation in glasses,” *Physical Review Letters*, vol. 96, no. 2, p. 025506, 2006. **This is a key paper of this thesis. It contains the description of the NK model, used here to prove that rejuvenation and overaging are a general phenomenon.**

- [48] R. Phillips, D. Rodney, V. Shenoy, E. Tadmor, and M. Ortiz, “Hierarchical models of plasticity: dislocation nucleation and interaction,” *Modelling and Simulation in Materials Science and Engineering*, vol. 7, no. 5, p. 769, 1999.
- [49] L. Shilkrot, R. Miller, and W. Curtin, “Coupled atomistic and discrete dislocation plasticity,” *Physical Review Letters*, vol. 89, no. 2, p. 025501, 2002.
- [50] V. Bulatov, F. F. Abraham, L. Kubin, B. Devincre, and S. Yip, “Connecting atomistic and mesoscale simulations of crystal plasticity,” *Nature*, vol. 391, no. 6668, pp. 669–672, 1998.
- [51] J. Langer, “Shear-transformation-zone theory of deformation in metallic glasses,” *Scripta materialia*, vol. 54, no. 3, pp. 375–379, 2006.
- [52] A. Argon, “Plastic deformation in metallic glasses,” *Acta Metallurgica*, vol. 27, no. 1, pp. 47–58, 1979.
- [53] F. Spaepen, “A microscopic mechanism for steady state inhomogeneous flow in metallic glasses,” *Acta Metallurgica*, vol. 25, no. 4, pp. 407–415, 1977.
- [54] E. Bouchbinder. Private Communication.
- [55] L. Corte, P. Chaikin, J. Gollub, and D. Pine, “Random organization in periodically driven systems,” *Nature Physics*, vol. 4, no. 5, pp. 420–424, 2008. **This is a key paper of this thesis. In this paper the behavior of a non-colloidal suspension under oscillatory deformation is described and modeled. In this thesis we aimed at understanding whether some of the behavior seen in such suspensions is found in the case of glassy systems.**
- [56] G. I. Menon and S. Ramaswamy, “Universality class of the reversible-irreversible transition in sheared suspensions,” *Physical Review E*, vol. 79, no. 6, pp. 061108\_1–061108\_4, 2009.
- [57] H. Hinrichsen, “Non-equilibrium critical phenomena and phase transitions into absorbing states,” *Advances in physics*, vol. 49, no. 7, pp. 815–958, 2000.
- [58] N. C. Keim and S. R. Nagel, “Generic transient memory formation in disordered systems with noise,” *Physical Review Letters*, vol. 107, no. 1, p. 010603, 2011. **This is a key paper of this thesis. It contains the observation of memory effects in sheared non-colloidal suspensions. In this thesis we aimed at understanding whether a similar kind of memory can be encoded in glassy systems.**
- [59] S. Toxvaerd, U. R. Pedersen, T. B. Schröder, and J. C. Dyre, “Stability of supercooled binary liquid mixtures,” *The Journal of Chemical Physics*, vol. 130, p. 224501, 2009.

## Bibliography

---

- [60] P. Bordat, F. Affouard, M. Descamps, and F. Müller-Plathe, “The breakdown of the Stokes–Einstein relation in supercooled binary liquids,” *Journal of Physics: Condensed Matter*, vol. 15, no. 32, p. 5397, 2003.
- [61] D. Frenkel and B. Smit, *Understanding molecular simulation: from algorithms to applications*. Access Online via Elsevier, 2001.
- [62] P. H. Hünenberger, “Thermostat algorithms for molecular dynamics simulations,” in *Advanced Computer Simulation*, pp. 105–149, Springer, 2005.
- [63] D. J. Evans and G. Morriss, *Statistical mechanics of nonequilibrium liquids*. Cambridge University Press, 2008.
- [64] A. F. Voter, F. Montalenti, and T. C. Germann, “Extending the time scale in atomistic simulation of materials,” *Annual Review of Materials Research*, vol. 32, no. 1, pp. 321–346, 2002.
- [65] A. Tangy, J. Wittmer, F. Leonforte, and J.-L. Barrat, “Continuum limit of amorphous elastic bodies: A finite-size study of low-frequency harmonic vibrations,” *Physical Review B*, vol. 66, no. 17, p. 174205, 2002.
- [66] C. E. Maloney and A. Lemaître, “Amorphous systems in athermal, quasistatic shear,” *Physical Review E*, vol. 74, no. 1, p. 016118, 2006.
- [67] S. Kobayashi, K. Maeda, and S. Takeuchi, “Computer simulation of deformation of amorphous Cu<sub>57</sub>Zr<sub>43</sub>,” *Acta Metallurgica*, vol. 28, no. 12, pp. 1641–1652, 1980.
- [68] D. L. Malandro and D. J. Lacks, “Relationships of shear-induced changes in the potential energy landscape to the mechanical properties of ductile glasses,” *The Journal of Chemical Physics*, vol. 110, p. 4593, 1999.
- [69] N. P. Bailey, J. Schiøtz, A. Lemaître, and K. W. Jacobsen, “Avalanche size scaling in sheared three-dimensional amorphous solid,” *Physical Review Letters*, vol. 98, no. 9, p. 095501, 2007.
- [70] D. Fiocco, G. Foffi, and S. Sastry, “Oscillatory athermal quasistatic deformation of a model glass,” *Phys. Rev. E*, vol. 88, p. 020301, 2013. **In this paper we describe the key results that we obtained in our simulations of oscillatory shear deformation of an LJ mixture.**
- [71] W. Kob and H. C. Andersen, “Scaling behavior in the  $\beta$ -relaxation regime of a supercooled Lennard-Jones mixture,” *Physical Review Letters*, vol. 73, no. 10, p. 1376, 1994.
- [72] S. Plimpton, “Fast parallel algorithms for short-range molecular dynamics,” *Journal of Computational Physics*, vol. 117, no. 1, pp. 1–19, 1995.

---

## Bibliography

- [73] S. Nosé, “An improved symplectic integrator for Nosé-Poincaré thermostat,” *Journal of the Physical Society of Japan*, vol. 70, p. 75, 2001.
- [74] J. R. Shewchuk, “An introduction to the conjugate gradient method without the agonizing pain,” 1994.
- [75] C. Chakravarty, P. G. Debenedetti, and F. H. Stillinger, “Generating inherent structures of liquids: Comparison of local minimization algorithms,” *The Journal of Chemical Physics*, vol. 123, p. 206101, 2005.
- [76] D. Ceperley and D. D. Johnson, “Statistical errors,” on <http://courses.physics.illinois.edu/phys466/lnotes/errors.html>, 2001.
- [77] J.-P. Hansen and I. R. McDonald, *Theory of simple liquids*. Access Online via Elsevier, 1990.
- [78] T. B. Schröder, S. Sastry, J. C. Dyre, and S. C. Glotzer, “Crossover to potential energy landscape dominated dynamics in a model glass-forming liquid,” *The Journal of Chemical Physics*, vol. 112, p. 9834, 2000.
- [79] N. Duff and D. J. Lacks, “Shear-induced crystallization in jammed systems,” *Physical Review E*, vol. 75, no. 3, p. 031501, 2007.
- [80] S. Yuste, E. Abad, and K. Lindenberg, “Exploration and trapping of mortal random walkers,” *Physical Review Letters*, vol. 110, no. 22, p. 220603, 2013.
- [81] S. Ramaswamy. Private Communication.
- [82] E. Jones, T. Oliphant, P. Peterson, *et al.*, “SciPy: Open source scientific tools for Python,” 2001–.
- [83] A. A. Hagberg, D. A. Schult, and P. J. Swart, “Exploring network structure, dynamics, and function using NetworkX,” in *Proceedings of the 7th Python in Science Conference (SciPy2008)*, (Pasadena, CA USA), pp. 11–15, 2008.
- [84] D. Fiocco, G. Foffi, and S. Sastry, “Encoding of memory in sheared amorphous solids,” *Physical Review Letters*, vol. 112, no. 2, p. 025702, 2014. **In this paper we describe our key results about memory phenomena in the LJ and NK models.**
- [85] D. Fiocco, “on <https://github.com/davidefiocco/phd-thesis>,” 2013.
- [86] I. Regev, T. Lookman, and C. Reichhardt, “Onset of irreversibility and chaos in amorphous solids under periodic shear,” *Physical Review E*, vol. 88, no. 6, p. 062401, 2013.
- [87] N. V. Priezjev, “Heterogeneous relaxation dynamics in amorphous materials under cyclic loading,” *Physical Review E*, vol. 87, no. 5, p. 052302, 2013.

## Bibliography

---

- [88] C. Domb, *Phase transitions and critical phenomena*, vol. 19. Access Online via Elsevier, 2000.
- [89] F. Varrato, L. Di Michele, M. Belushkin, N. Dorsaz, S. H. Nathan, E. Eiser, and G. Foffi, “Arrested demixing opens route to bigels,” *Proceedings of the National Academy of Sciences*, vol. 109, no. 47, pp. 19155–19160, 2012. **This is a key paper of this thesis. In it bigels, intertwining ramified colloidal structures obtained from binary mixtures, are introduced. In an appendix of this thesis we perform simulations of the behavior of such systems under shear deformation.**
- [90] L. Di Michele, F. Varrato, D. Fiocco, S. Sastry, E. Eiser, and G. Foffi, “Aggregation dynamics, structure, and mechanical properties of bigels,” *Soft Matter*, 2014. **In this paper we describe the key results of our simulations of the deformation behavior of gels and bigels.**
- [91] G. Foffi, C. De Michele, F. Sciortino, and P. Tartaglia, “Scaling of dynamics with the range of interaction in short-range attractive colloids,” *Physical Review Letters*, vol. 94, no. 7, p. 078301, 2005.
- [92] G. Foffi, C. De Michele, F. Sciortino, and P. Tartaglia, “Arrested phase separation in a short-ranged attractive colloidal system: A numerical study,” *The Journal of Chemical Physics*, vol. 122, p. 224903, 2005.
- [93] P. J. Lu, E. Zaccarelli, F. Ciulla, A. B. Schofield, F. Sciortino, and D. A. Weitz, “Gelation of particles with short-range attraction,” *Nature*, vol. 453, no. 7194, pp. 499–503, 2008.
- [94] C. N. Likos, “Effective interactions in soft condensed matter physics,” *Physics Reports*, vol. 348, no. 4, pp. 267–439, 2001.
- [95] N. Dorsaz and G. Foffi, “Phase behaviour of the symmetric binary mixture from thermodynamic perturbation theory,” *Journal of Physics: Condensed Matter*, vol. 22, no. 10, p. 104113, 2010.
- [96] B. Rajaram and A. Mohraz, “Microstructural response of dilute colloidal gels to nonlinear shear deformation,” *Soft Matter*, vol. 6, no. 10, pp. 2246–2259, 2010.
- [97] J. Sprakel, S. B. Lindström, T. E. Kodger, and D. A. Weitz, “Stress enhancement in the delayed yielding of colloidal gels,” *Physical Review Letters*, vol. 106, no. 24, p. 248303, 2011.

# Davide Fiocco

## Doctoral Assistant EPFL

Chemin des Bégonias 1  
CH-1018 Lausanne  
+41 (0) 76 308 83 98  
[davide.fiocco@gmail.com](mailto:davide.fiocco@gmail.com)  
Born in Verona, Italy, age 29



## Experience

2009--present **Research assistant**, EPFL, Lausanne.

- Research:
  - Investigation of mechanical properties of dense amorphous materials in the frame of the Indo-Swiss joint research program between the EPFL, Switzerland and JNCASR Bangalore and TIFR Hyderabad, India;
  - Investigation of mechanical properties of gels and bigels within a collaboration between the EPFL and the University of Cambridge, United Kingdom;
  - Studies of diffusion of water in sugar matrices, via coarse-grained models, in order to achieve a long-lasting foam on beverages (cappuccino), in a collaboration between the EPFL and the Nestlé Research Center, Lausanne, Switzerland;
  - Investigation on effective forces in asymmetric binary mixtures of square-well fluids, in collaboration with the University of Trieste, Italy.
- Talks:
  - "Oscillatory deformation of a model glass"  
From cooperativity in supercooled liquids to plasticity of amorphous solids,  
CECAM workshop, ETH, Zurich, Switzerland, June 2013
- Publications:
  - Effective forces in square well and square shoulder fluids, *J. Phys. Chem. B*, 2010
  - Oscillatory athermal quasi-static deformation of a model glass, *Physical Review E*, 2013
  - Encoding of memory in sheared amorphous solids, *PRL*, 2014
  - Aggregation dynamics, structure, and mechanical properties of bigels, *Soft Matter*, 2014
- Teaching:
  - General Physics, assisting Prof. C. Hébert
  - Biothermodynamics, assisting Prof. P. De Los Rios and Prof. M. Dal Peraro
  - I mentored Master's students in Physics during their theses/projects.

## Education

2009--present **Ph.D. Candidate**, Theoretical Physics Institute, EPFL, Lausanne.

Courses:

- School and Conference on Multiscale Modeling and Simulations of Hard and Soft Materials, Bangalore, India, December 2009
- Multiscale simulation methods for complex flows, Lausanne, Switzerland, June 2010
- Complex materials in Physics and Biology, Varenna, Italy, July 2010
- First school on Computational Physics: Soft Matter, Les Houches, France, June 2011
- Modern Computational Science: Optimization: Oldenburg, Germany, August 2012
- Modern Photovoltaic Technologies, Lausanne, June 2013

2007--2009 **M.Sc. Condensed Matter Physics**, Università degli Studi di Trieste, Trieste, Italy, 110/110 and honors.

Theoretical and experimental methods of solid state physics: electronic properties in materials, physics of surfaces, fundamentals of semiconductor fabrication, numerical simulation via Monte Carlo and Molecular Dynamics.

2003--2007 **B.Sc. Physics**, Università degli Studi di Trieste, Trieste, Italy, 109/110.

Inelastic X-ray and UV scattering at the synchrotron radiation facilities ESRF, Grenoble, France and Elettra, Trieste, Italy

2003 **Scientific high school degree**, Liceo Scientifico G. Galilei, Verona, Italy, 99/100.